Photoelectrochemical Behavior of WO_3 Electrodeposited on Stainless Steel Microfiber for Flexible, Wire-Shaped Photovoltaic Cells

by

Taehwan Kim

Submitted in Partial Fulfillment of the Requirements

for the Degree of

Doctor of Philosophy

in the

Materials Science and Engineering

Program

YOUNGSTOWN STATE UNIVERSITY

August 2022

Photoelectrochemical Behavior of WO_3 Electrodeposited on Stainless Steel Microfiber for Flexible, Wire-shaped Photovoltaic Cells

Taehwan Kim

I hereby release this to the public. I understand that this crystal structure, morphology, and photoelectrochemical behavior of WO_3 electrodeposited on stainless steel microfiber will be made available from the OhioLINK ETD Center and the Maag Library Circulation Desk for public access. I also authorize the University or other individuals to make copies of this thesis as needed for scholarly research.

Signature:

Taehwan Kim, Student	Date

Approvals:

Dr. *Clovis A. Linkous*, Thesis Advisor	Date
Dr. *Tom N. Oder*, Committee Member	Date
Dr. *Donald J. Priour*, Committee Member	Date
Dr. *Farzad Ahmadi*, Committee Member	Date
Dr. *Taci Turel*, Committee Member	Date
Dr. *Salvatore A. Sanders*, Dean of Graduate Studies	Date

ABSTRACT

Photovoltaic cells have become ideal alternatives to conventional energy technologies due to their ability to convert clean, unlimited, and sustainable solar energy into electricity. However, the conventional rigid, planar structure of photovoltaic cells has limitations in modern electronic applications. Therefore, there is increasing interest in developing next-generation PV devices with more sophisticated design. One simple and effective method is to fabricate the cell into a wire-shaped format, where the thread itself is capable of a PV effect combined with the advantage of being weavable into a textile. In this research, electrodeposited, micron-sized islands of n-WO_3 on stainless steel thread, serving as a semiconductor photoanode, was paired with a platinum-modified, polymer latex-coated stainless steel wire as a counter electrode in iodide/triiodide electrolyte to prepare a wire-shaped liquid junction solar cell. In contrast to previous studies, the active layer of WO_3-deposited thread was twisted around the counter electrode to achieve more uniform light absorption along the length of the PV wire cell. The WO_3/steel wire-shaped PV cell gave a photoconversion efficiency of 0.36% under illumination of 71 mW/cm^2, which was further improved to 1.86% by loading a natural anthocyanin dye sensitizer onto the surface of the active layer and using acetonitrile instead of water as the solvent. Additionally, to improve the performance of the cells, redox catalyst triethylamine was added to the iodide/acetonitrile electrolyte. Adding the amine under the same illumination conditions improved efficiency to 0.53% for the WO_3/steel wire-shaped PV cell and 2.44% for the anthocyanin dye-sensitized cell. This value is comparable to what others have achieved in wire-shaped PV cell performance.

Table of Contents

List of Figures

Lists of Tables

Chapter 1. Introduction

1-1. Photovoltaic wearable electronics

Wearable electronics fabricated on lightweight and flexible substrates have great potential for portable devices. Lightweight and wearable power supply modules with high energy storage performance are desirable for wearable technologies.[1] Recently, there is growing interest in making wire/fiber-shaped PV cells for flexible and woven (or textile) power supply electronics, of which the wire/thread comprising the textile itself is capable of a PV effect. The advantages of being lightweight, flexible and integrable into textiles in various forms make it a more practical approach for wearable electronics.

1-2. Photovoltaic cells

Renewable energy technologies have gained much attention due to their significant advantages compared to those based on conventional energy sources such as fossil fuels. Solar energy is the predominant renewable energy source; it can be directly transduced into electrical energy with photovoltaic cells. A photovoltaic cell is an electrical device that converts the light energy directly into electricity by the photovoltaic effect.[2] Photovoltaic cells are composed of layers of semiconducting materials forming p-n junctions which can convert light energy into electric current and voltage.[3] The structure of a PV cell is shown in Fig.1. The p-n junction occurs at the interface between a p-type semiconductor and an n-type semiconductor. Near the interface is a depletion region

where the carrier density is low due to charge transfer across the interface. This also results in a net charge building up on either side of the interface. The n-type side possesses a net positive charge, and the p-type side possesses a net negative charge. This charge distributions generates an internal electric field across the interface. When a photon is absorbed within the space charge layer, it results in the formation of an electron-hole pair. The effect of the electric field is to force the electrons to toward the n-type region and holes to the p-type region. This redistribution of charge results in photovoltage. If the back contacts of the p-n junction are connected through an external circuit, the photogenerated charge carriers will travel through the circuit, measured as photocurrent and photovoltage.[4]

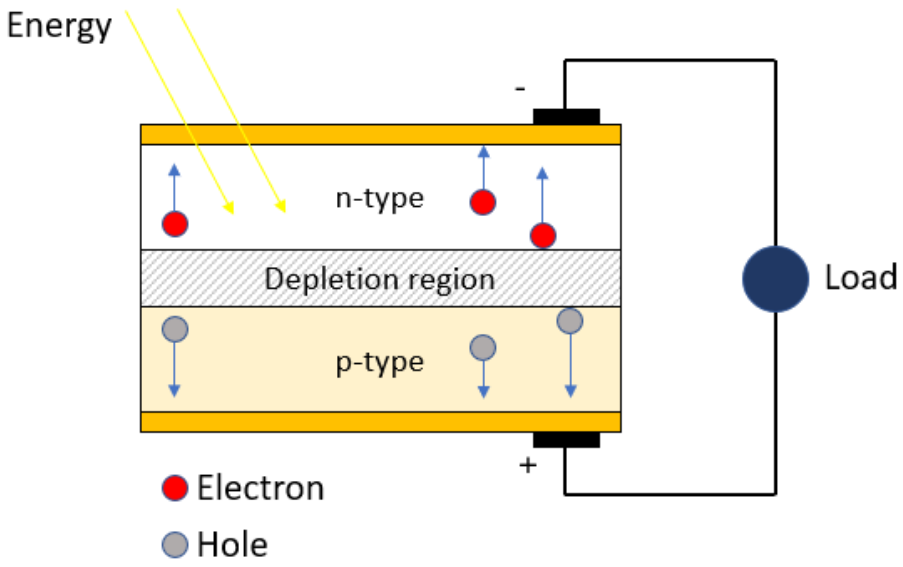

Figure 1. Schematic diagram of p-n junction photovoltaic cell.

1-3. The p-n junction

The p-n junction is the boundary that is formed between two semiconductor phases, one p-type, one n-type, when they are brought into contact with each other. Their electronic structure was altered by doping or growth of a layer of crystal with dopant. A dopant is an impurity that is intentionally introduced into a semiconductor for optimizing its electrical properties. N-type doping is the introduction of impurity atoms (dopants) which possess a filled electronic energy level near the conduction band edge. Phosphorus is a good n-type dopant for silicon, since the host semiconductor has four valence electrons while P has five electrons. If a small amount of P is added to a pure silicon crystal, one of its valence electrons can be thermally promoted into the conduction band, where it becomes a free electron. A p-type dopant introduces empty energy levels near the valence band of the semiconductor. For example, Si is doped with boron. The three valence electrons of B will be insufficient to bond to all of its Si neighbors. Filling the empty orbital with an electron produces a hole.[5] A schematic diagram of the energy band diagram of a p-n junction is shown in Fig. 2. Under illumination, absorption of photons in the semiconductor generates electron-hole pairs, resulting in excess mobile charge carriers. These charge carriers are then transported in the direction of electric field across the p-n junction. While the minority charge carriers of the n-type region (holes) are transported in the direction of the electric field, the electrons in the p-type region are transported in the opposite direction of the electric field.[6]

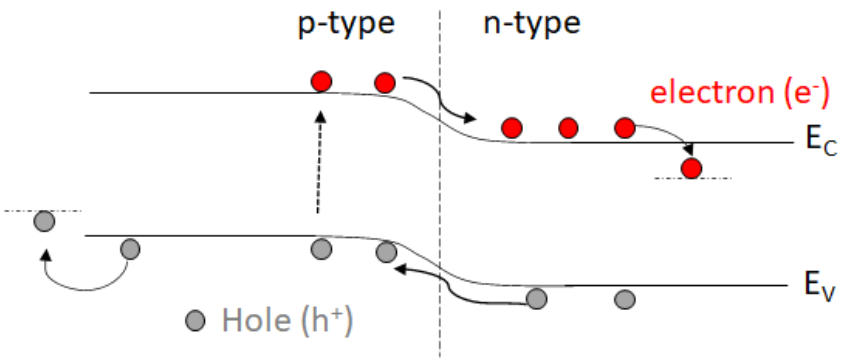

Figure 2. Energy band diagram of p-n junction.

1-4. Photovoltaic characterization

The performance of the photovoltaic device can be evaluated by using open circuit voltage (V_{OC}), short circuit current (J_{SC}), fill factor (FF) and overall efficiency (η) as shown in Fig. 3. V_{OC} is the voltage across negative and positive electrodes under open circuit condition at zero current, or the potential difference between the conduction band energy of the semiconducting material and the redox potential of the electrolyte.[7] In contrast, J_{SC} is the short circuit current at zero potential. P_{max} is the maximum efficiency of the cell to convert sunlight into electricity and FF is the ratio of current times voltage at power maximum divided by the product of V_{OC} and J_{SC}.[8] Finally, the overall efficiency is the percentage of solar energy converted to electrical energy, where η increases with FF, V_{OC}, and J_{SC} over the incident light intensity.

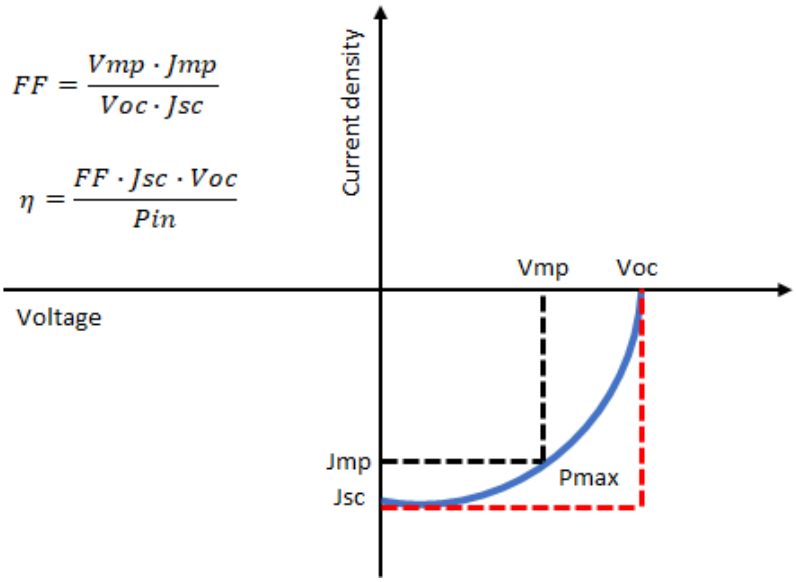

Figure 3. I-V curve to evaluate PV cell performance.

1-5. Liquid junction solar cell

Liquid junction photoelectrochemical cells (PEC) were first studied in the 1950s in the dark and under illumination. Semiconductor electrodes can act either as donors or acceptors for electron exchange with excited molecules in the electrolyte. Semiconductor has a sufficiently large band gap which the reaction with both ground and excited state will not occur simultaneously unlike metal. Therefore, it is possible to observe the injection of electrons or holes into the semiconductor by photocurrents produced.[9] The use of PECs in a solar energy conversion and storage scheme was first suggested by Fujishima and Honda in 1972, where titanium dioxide (TiO_2) in the rutile phase was used to split water under solar illumination.[10] The dye-sensitized solar cell (DSSC) is a photoelectrochemical cell where a wide band gap semiconductor such as TiO_2 is made responsive to visible wavelength radiation via contact with a with a dye or

photosensitizer, platinum-deposited counter electrode, and a redox liquid electrolyte invented by O'Regan and Grätzel in 1991.[11] The main feature of the DSSC is that light absorption takes place in a layer of adsorbed sensitizer rather than the semiconductor layer. The PEC consists of several components, namely, a transparent conducting oxide glass (TCO), thin layer of semiconductor film, electrolyte containing redox mediator, and usually platinum deposited counter electrode. The role of TCO is to allow the light passing through the PEC and DSSC with support of semiconductor. The layer of the semiconductor film serves as a photovoltaic effect, which electron-hole pairs are generated in this layer. The electrolyte containing redox-oxidation mediator serves as a medium of collecting electrons that flow through the semiconductor.

1-5-1. Working principle of PEC

The critical component of the PEC is the semiconductor, which has been configured as an electrode, Electron-hole pairs are generated in the semiconductor by the irradiation of the electrode with photons whose energy is equal or greater than the band gap energy of the semiconductor. When light illuminates a photoanode, electrons in the valence band are excited to the conduction band of the semiconductor, leaving a hole behind. The photogenerated electrons are swept out toward the electrical circuit and are transported to a counter electrode. Fig. 4 shows the general working principal of a PEC. As the PEC cell illustrated in Fig. 4(a)goes under illumination, the PEC undergoes six processes: (1) absorption of light by the semiconductor film; (2) generation of electron-hole pairs according to the photon energy; (3) generated electron flow from the n-type photoelectrode to produce electric current; (4) reduction at the interface of the counter

electrode and electrolyte; (5) oxidation at the surface of the semiconductor and electrolyte; and (6) recombination between electrons and holes in the semiconductor. From Fig. 4(b) upon light illumination, electrons from the valence band excite across the bandgap to the conduction band of the semiconductor, leaving holes in the valence band.[12] The conduction band and valence band are bent and produce a potential barrier. The potential barrier prevents the flow of excited electrons from the semiconductor to the electrolyte and hinders the recombination of the electrons and holes. In an n-type semiconductor, the Fermi energy is higher than the redox potential of the electrolyte.[13] The excited electrons are collected by the photoelectrode and driven to the counter electrode through an external circuit. Holes are driven to the interface between the semiconductor and the electrolyte to perform oxidation.

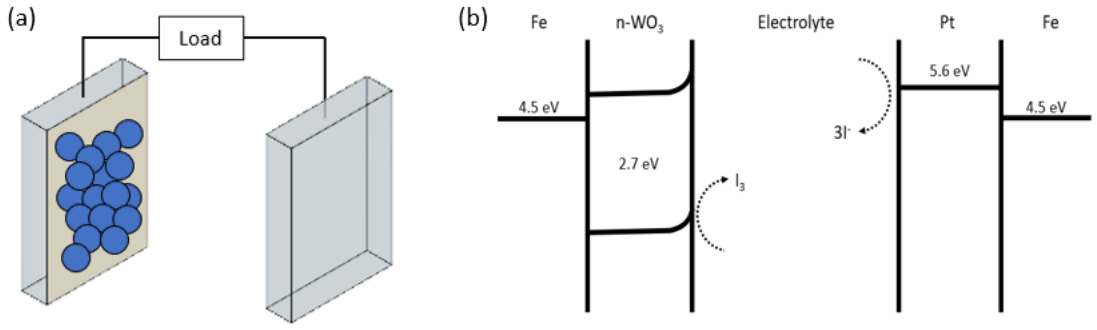

Figure 4. Schematic diagram of (a) photoelectrochemical cell, and (b) band gap comparison of each working and counter electrode.

1-5-2. Working principle of DSSC

The electrical energy produced and stored in a DSSC is similar to the PEC where a highly adsorptive layer of organic or organometallic dye covers the semiconductor and "sensitizes" it to visible wavelength light. A schematic diagram of DSSC operation is displayed in Fig. 5(a). A DSSC is composed of a redox couple electrolyte system, typically iodide and triiodide complex. A photoanode covered with photosensitize dye molecules and a counter electrode are sandwiched between two pieces of TCO glass, and the redox couple in the electrolyte is used to regenerate the oxidized dye. The total efficiency of the DSSC is dependent on the optimization and compatibility of each one of the components and more particularly the photoanode, which plays a vital role in the charge generation and transfer processes. From Fig. 5(b) the working principle of the DSSC follows the sequence: (1) the cell is illuminated onto and a photon is absorbed by a dye molecule, (2) the dye is energetically promoted to its excited state, (3) the excitation results in an injection of an electron into the semiconductor, which is then transported through the network of deposited semiconductor anode to the back contact, where it flows into the external circuit. (4) concurrently, the oxidized dye is reduced to its ground state by the redox species present in the electrolyte, which iodide reduces the oxidized dye to form an intermediate ionic species, (5) then to form triiodide, diffuses to the counter electrode where the regeneration cycle of triiodide reduction back to iodide takes place at the platinum-coated cathode.[14] To increase the power conversion efficiency of a DSSC, a nanostructured porous titanium dioxide (TiO_2) with a wide bandgap and large excitation binding energy is typically used in constructing the photoanode.[15] The

large surface area of nanostructured TiO_2 ensures substantial adsorption of dye molecules with efficient electron injection into the conduction band .

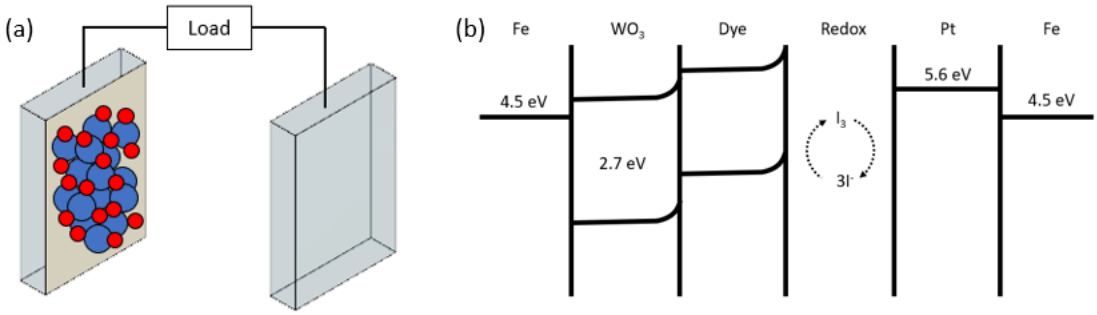

Figure 5. Schematic diagram of (a) dye-sensitized solar cell, and (b) energy level comparison of each component: working electrode, dye, and counter electrode.

1-6. Tungsten oxide (WO_3)

To date the most efficient and well-studied liquid junction solar cells are based on TiO_2, with efficiencies approaching 12%.[16] While most of the research is focused on TiO_2, other metal oxides such as WO_3 are possible alternatives with promising photoconductive behavior for solar energy devices. WO_3 is an n-type semiconductor with energy band gap commonly observed in a range from 2.6 to 3.1 eV, which corresponds to the blue near UV region of the solar spectrum.[17] For TiO_2, the absorption edge commonly appears at 380 nm (purple region), while the WO_3 absorption edge appears at 420 nm.[18] The function of the semiconducting material is to absorb sunlight, resulting in the creation of an electron in the conduction band. TiO_2 has a band gap of 3.2 eV and only absorbs the UV portion of the solar spectrum, accounting for only 4% of the total irradiance.[19] For visible light harvesting, as shown in Fig. 6, the position of the WO_3 conduction band is

lower in energy than that of TiO_2 and thus WO_3 can act as an electron scavenger, without the risk of H_2 evolution. Also, WO_3 typically has a higher carrier mobility than TiO_2.[20]

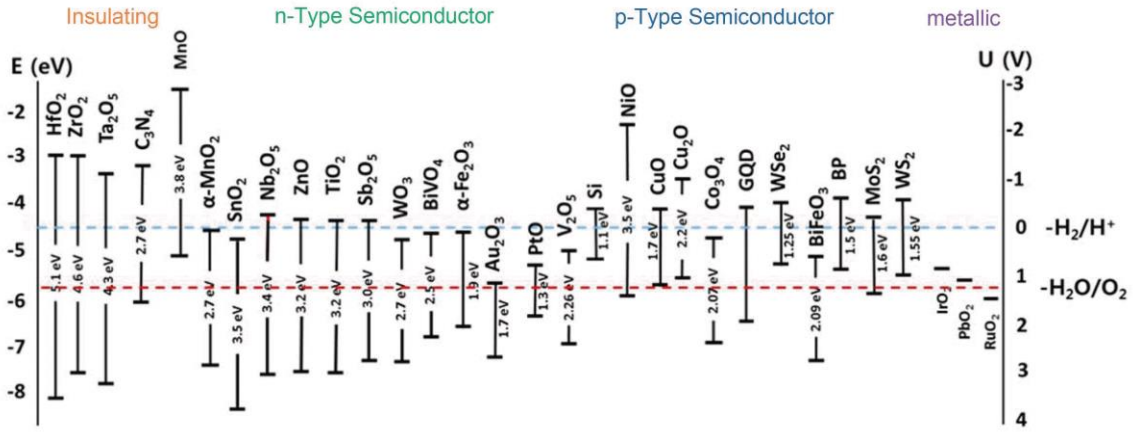

Figure 6. Bandgap energy and bandgap alignment comparison of various metal oxides.[16]

1-6-1. Crystal structure of WO_3

WO_3 is reported to have different crystal structures as a function of temperature. Its various crystal phases consist of WO_6 octahedra arranged in various corner sharing configurations. The phases obtained by corner sharing are monoclinic II, triclinic, monoclinic I, orthorhombic, tetragonal, and cubic. The room temperature monoclinic I structure, which is shown in Fig. 7, is the most stable form of WO_3, favorable for PEC applications.[21] There is also a hexagonal phase of WO_3, which can be obtained by heating the hydrated oxide.[22] As shown in Fig. 8, there are trigonal cavities and hexagonal windows. After stacking of WO_6 octahedra, trigonal and hexagonal tunnels along the c axis, which enable rapid conduction of ions and electrons.[23] The phase

transition behavior of nanostructured WO_3 mainly depends on the morphology, which is greatly affected by the synthetic process used on the initial precursors.

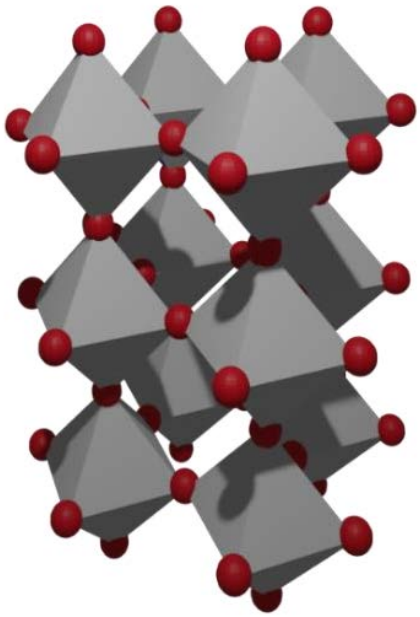

Figure 7. Crystal structure of monoclinic WO_3.

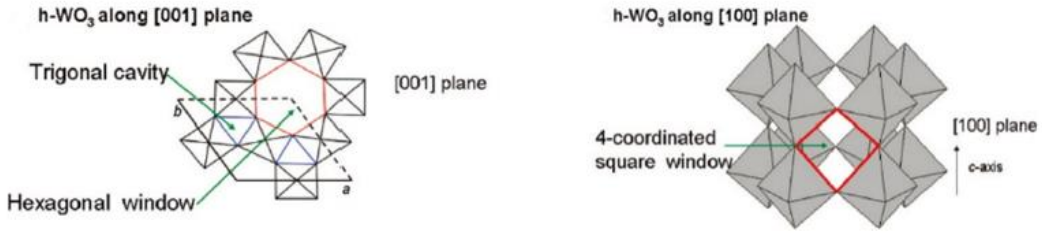

Figure 8. Crystal structure of hexagonal phase of WO_3.[23]

1-6-2. Nanostructured WO_3

The synthesis and analysis of WO_3 nanostructures has become increasingly prominent with the advent of nanotechnologies. Enhancing the performance of functional materials, nano-structured WO_3 features an increased surface to volume ratio, which can provide more surface area for both chemical and physical interaction.[24] Also, due to their inherently small size, quantum confinement effects influence the charge transport, electronic band structure and optical properties.[25] In addition to light absorption in the visible region, the morphology of WO_3 is another key factor in the efficiency of a photoelectric cell. Various types of nanostructured WO_3 thin films are shown in Fig. 9, including nanoflakes[26], nanoplates[27], nanorods[28], nanowires[29], nanotubes[30], and nanoflowers[31], which can be fabricated by various film deposition techniques.

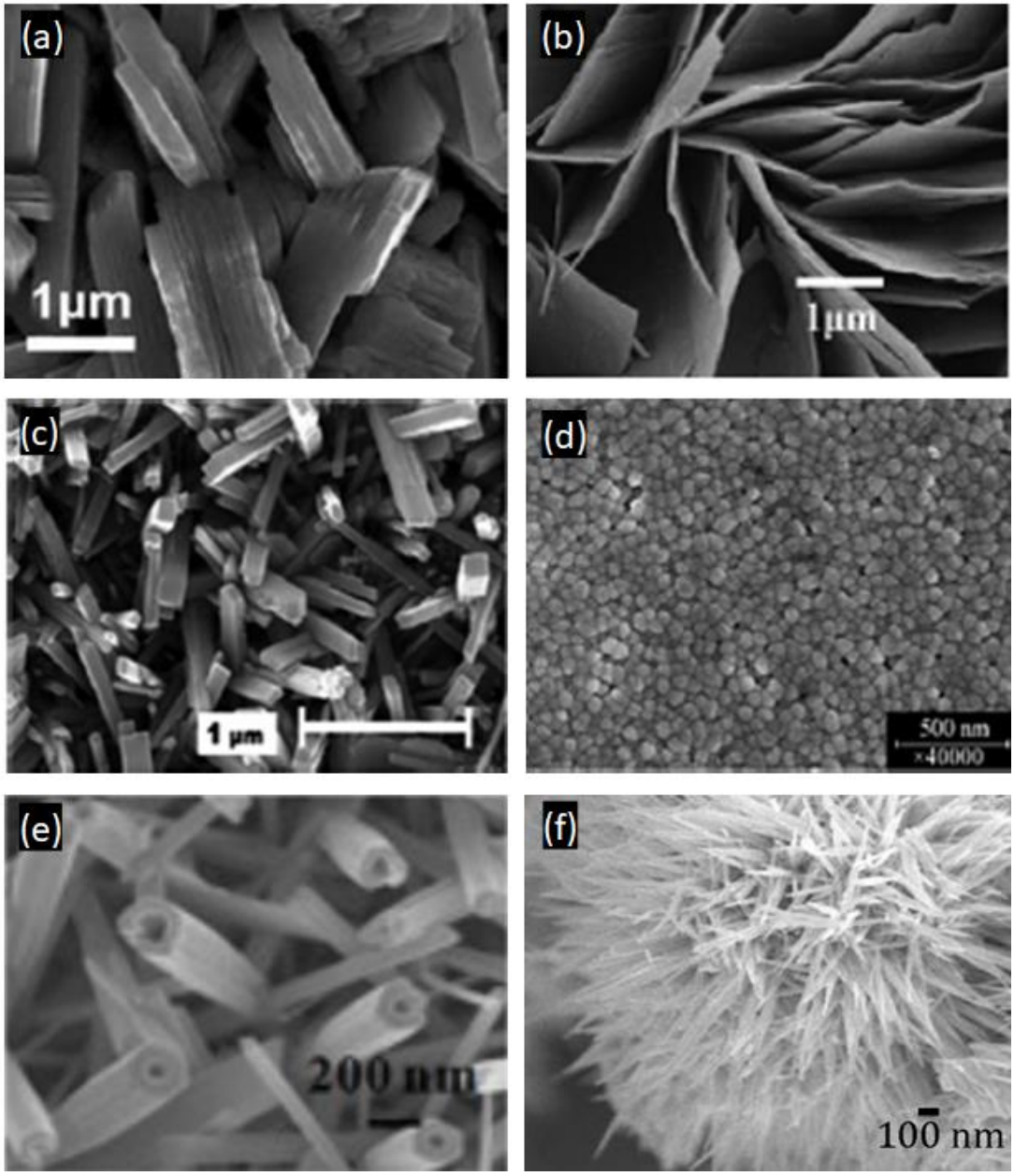

Figure 9. Various nanostructured WO_3 nanoarrays of (a) nanoplates[26], (b) nanoflakes[27], (c) nanowires[28], (d) nanoparticles[29], (e) nanotubes[30], and (f) nanoflowers[31].

1-6-3. Electrodeposited WO_3 film

The photoelectrochemical behavior of WO_3 can be greatly influenced by the synthesis method. Electrodeposition is one of the methods that can deposit films onto a complex structure (substrate). In a potentiostat (three-electrode) system, an electrolyte containing a WO_3 precursor species is subjected to a DC electrical current from an electrode or conducting substrate immersed in the electrolyte , whereupon the precursor species is reduced to the oxide and deposited on the substrate to form the film.[32] Kwong et al.[33] has reported electrodeposited thin films of WO_3 on FTO glass by using an aqueous solution of peroxotungstic acid. The electrodeposition was performed with a three-electrode system consisting of FTO glass as working electrode, Pt foil as counter electrode, and Ag/AgCl as a reference electrode. An applied potential of 0.4 V was used. Photocurrent density of 0.06 mA/cm^2 at 0.7 V was achieved. There are few photoelectrochemical examples where WO_3 was electrodeposited onto stainless steel substrate. Georgieva et al.[34] electrodeposited WO_3 and bi-layer of WO_3/TiO_2 onto stainless steel 304 plate. Peroxytungstate and titanium oxosulfate acids solution were used for the deposition. The deposition was conducted for 30 min at -1.0 V vs mercury-mercurous sulfate (MSE) reference electrode. The electronic structure of the WO_3 layer relative to TiO_2 promotes better separation of electron-hole pairs and reduces recombination rates while enhancing visible wavelength absorption.

1-7. Liquid junction solar cells in wire format

Wire-shaped liquid junction solar cells have been mostly fabricated by twisting two conductive fibers together as electrodes and inserting into narrow bore, flexible tubing, and back-filling with electrolyte, with one as fiber as the working electrode coated with photoactive semiconductors or semiconductors coated with photosensitive dyes. A platinum wire is generally used as a counter electrode due to its high electrocatalytic activity for the electrolyte. The advantage of the wire-shaped liquid junction solar cells is that it can be easily connected to an external circuit with while maintaining flexibility of the cells.

1-7-1. Twisted metal wires as electrode substrates

Compared with the conventional planar structure, photovoltaic devices in wire format have attracted increasing attention as a light-weight configuration and can be easily woven into clothes or integrated into other structures, which enable applications in wearable electronics and various complex devices.[35] As shown in Fig. 10, Zou and co-workers[36] pioneered this cell by twisting two steel wires coated with porous titania and platinum respectively, to serve as working and counter electrodes. They achieved 0.61 V open circuit voltage (V_{OC}), 1.2 mA/cm^2 short circuit current (J_{SC}), 0.38 fill factor (FF), and energy conversion efficiency (η) of 0.27%. To improve the photovoltaic performance, they further used a titanium wire coated with a layer of titania nanoparticles to replace the porous titania-modified steel wire. A higher efficiency of 5.4% was achieved. Choudhury et al.[37] prepared photoactive TiO_2 hierarchical microstructures

using a simple and facile hydrothermal growth process onto Ti wire. To enhance the photon conversion efficiency, plasmonic nanoparticles of Ag were also deposited using a photoreduction method. The branched structure of the photoanode increased the dye loading by filling the space between the nanowires, while the Ag nanoparticles played the multiple roles of dye adsorption and light scattering to increase the efficiency of the cell. From Fig. 11 is a schematic depicting the procedure for constructing the hierarchical TiO_2 nanoforest structure decorated with Ag nanoparticles for a flexible wire-shaped DSSC. They achieved 0.882 V open circuit voltage (V_{OC}), 6.41 mA/cm^2 short circuit current (J_{SC}), 0.71 fill factor (FF), and maximum energy conversion efficiency (η) of 4.0%. They improved the charge collection efficiency by providing a preferential electron pathway with the photoactive morphology and the high-density of Ag nanoparticles on the forest-like structure, which serves to decrease charge recombination .

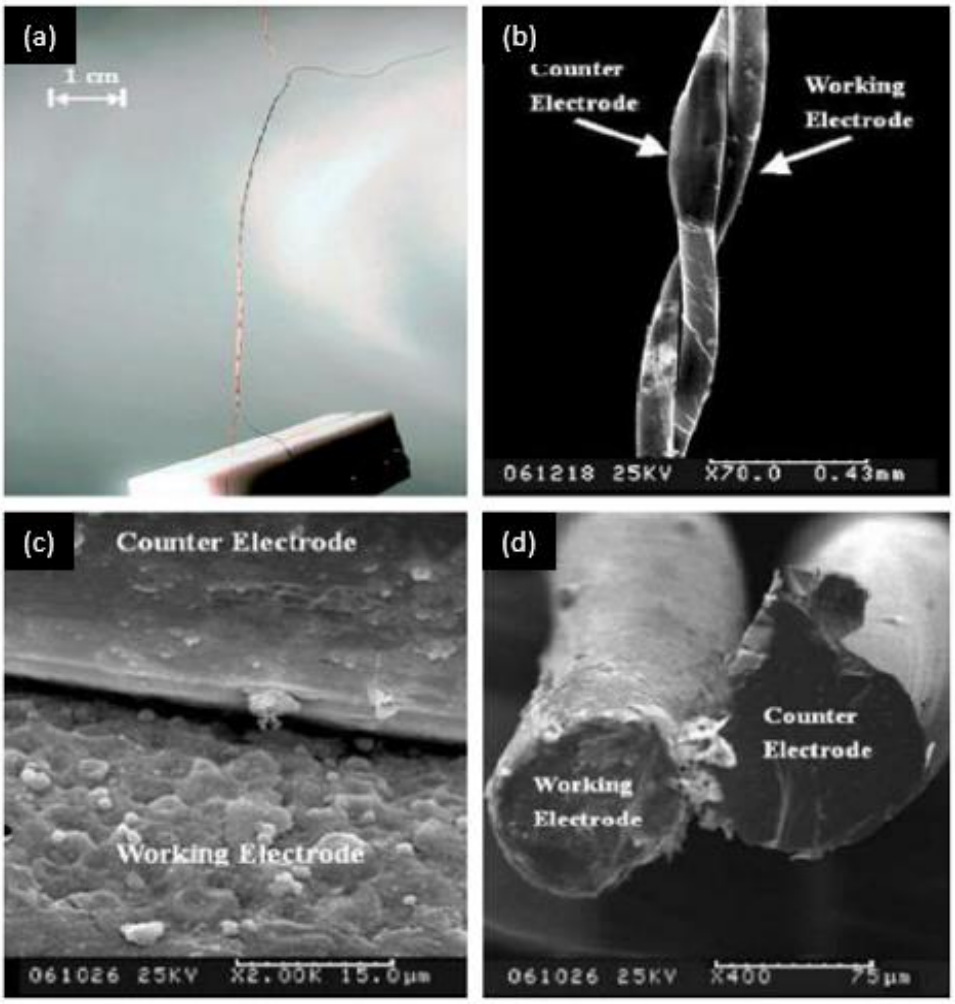

Figure 10. Wire shaped dye-sensitized solar cells (DSSCs) with (a) photograph and (b), (c) and (d) SEM images of a twisted wire-shaped DSSC.[36]

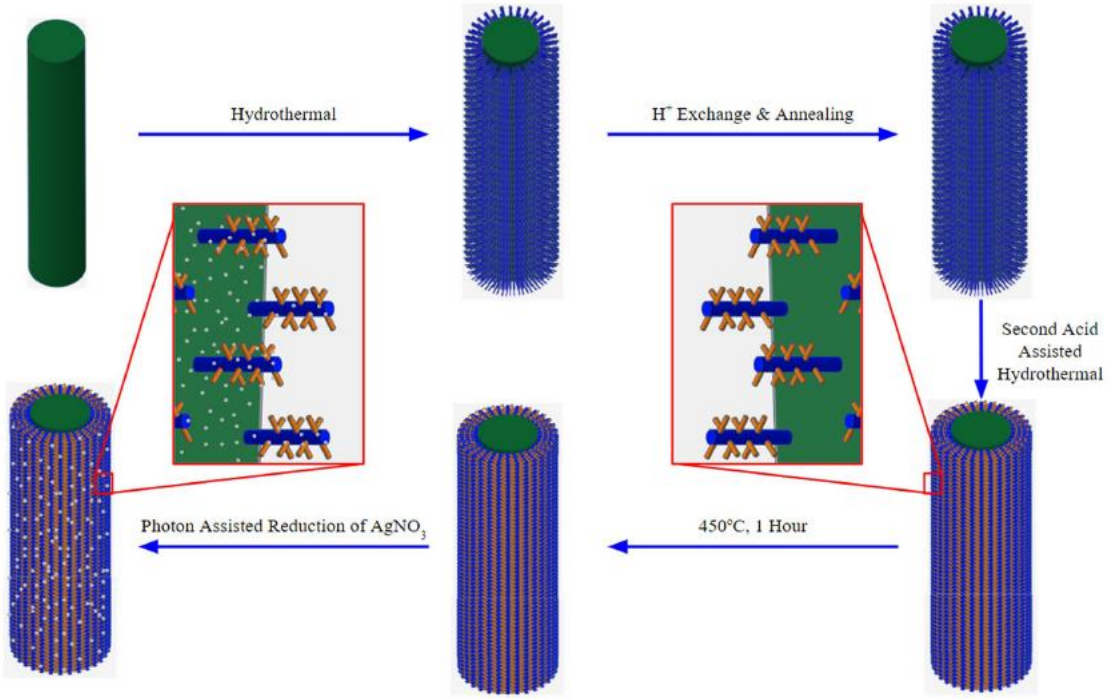

Figure 11. Schematic diagram of mechanism of the hierarchical growth of TiO_2 photoanode.[37]

1-7-2. Carbon fiber based DSSCs

Carbon fibers are flexible, low density, moderate conductivity, and high strength materials, and so are attractive candidates as electrodes for energy devices. As shown in Fig. 12, Cai et al.[38] developed an all carbon fiber-based DSSC in which a sensitized TiO_2 layer deposited onto carbon fiber working electrode with another carbon fiber coated with carbon ink to serve as a counter electrode. They achieved 0.329 V open circuit voltage (V_{OC}), 12.19 mA/cm^2 short circuit current (J_{SC}), 0.41 fill factor (FF), and maximum energy conversion efficiency (η) of 1.65%.

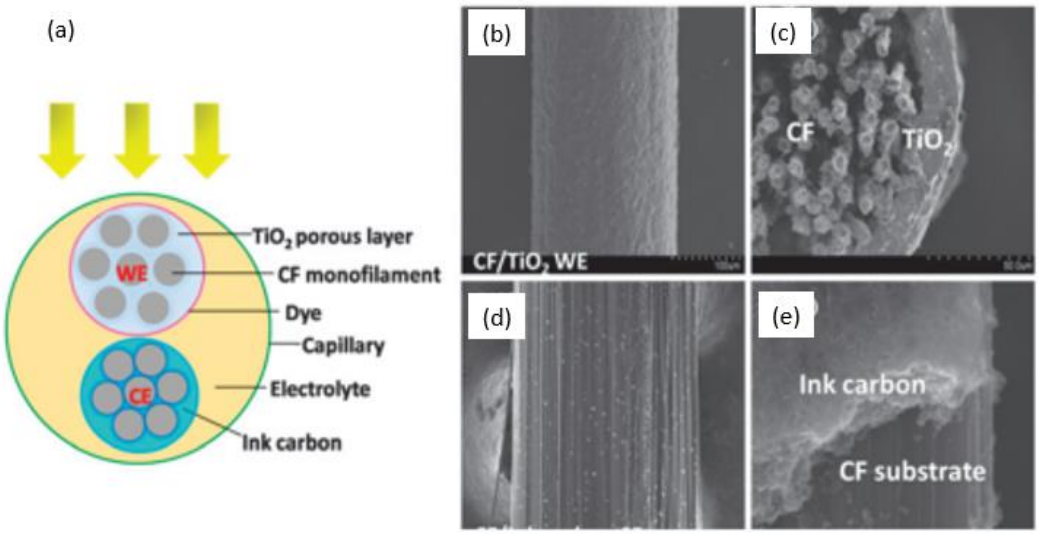

Figure 12. (a) Schematic diagram of the constructed carbon fiber based DSSC and SEM images of (b) cross-section, (c) carbon fiber/TiO_2, (d) carbon ink, and (e) boundary between the carbon ink and the carbon fiber substrate.[38]

Similarly, as shown in Fig. 13, aligned CNT fibers coated with TiO_2 photoactive layers were used as the working electrode and bare CNT fiber as the counter electrode in a wire-shaped DSSC prepared by Cai et al.[39] The two CNT fiber electrodes can be tightly twisted with close contact between them (Polyvinylidene fluoride (PVDF) non-electrically conductive polymer barrier coated onto CNT fiber counter electrode). The performance of the DSSC showed 0.64 V open circuit voltage (V_{OC}), 9.03 mA/cm^2 short circuit current (J_{SC}), 0.45 fill factor (FF), and maximum energy conversion efficiency (η) of 2.60%.

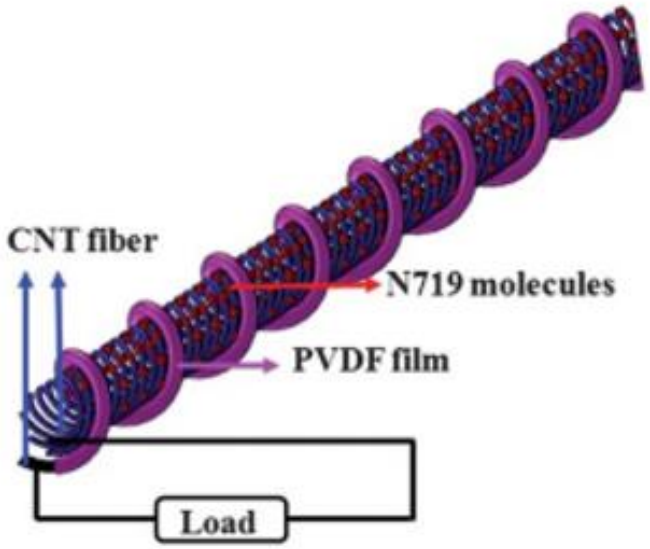

Figure 13. Schematic diagram of a CNT fiber based wire-shaped DSSC.[39]

1-7-3. Wire-shaped polymer solar cells

Compared with the metal wire-shaped solar cells, polymer solar cells (PSCs) can be made into solid state devices without use of liquid electrolytes. Twisted wire-shaped PSCs have been prepared by using modified Ti wire that was coated with a photoactive layer of poly(3-hexyl-2,5-thiophene) (P3HT) and (6,6)-phenyl1-C_{71} butyric acid methyl ester ($PC_{70}BM$) and twisted around an aligned CNT fiber. Fig. 14 shows the schematic diagram of the wire-shaped polymer cells by Chen et al.[40] The prepared cells showed 0.42 V open circuit voltage (V_{OC}), 0.98 mA/cm^2 short circuit current (J_{SC}), 0.36 fill factor (FF), and maximum energy conversion efficiency (η) of 0.15%. Although the cell efficiency is relatively low compared to the metal-based wire-shaped DSSCs, this work has provided an effective route to develop of wire-shaped polymer solar cells.

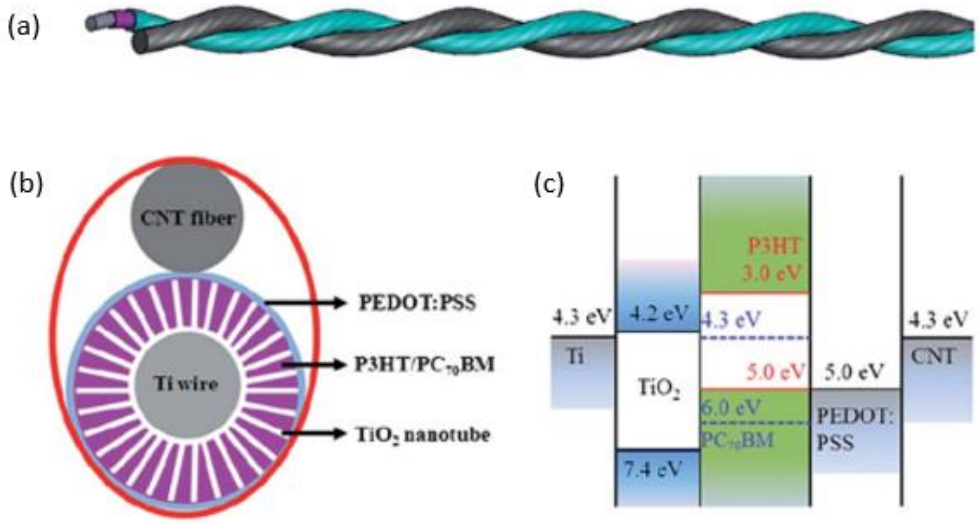

Figure 14. Schematic diagram of (a) wire-shaped polymer solar cell, (b) cross-sectional view, and (c) comparison of energy diagram.[40]

From Fig. 15 the wire-shaped PSC was fabricated by multilayer on the surface of steel wires for photoanode.[41] A zinc oxide (ZnO) layer was first deposited as a hole blocking layer and following with photoactive P3HT and PCBM layer were deposited onto the ZnO layer. A poly(3,4-ethylene-dioxythiophene):poly(styrene sulfonate) (PEDOT:PSS) layer coated to improve hole transport and electrical contact to the single-walled CNT counter electrode. By comparison to the planar, coated counter electrode, the photovoltaic wire showed higher efficiencies of 2.3%, which was close to 2.48% for their planar counter electrode parts under the same conditions.

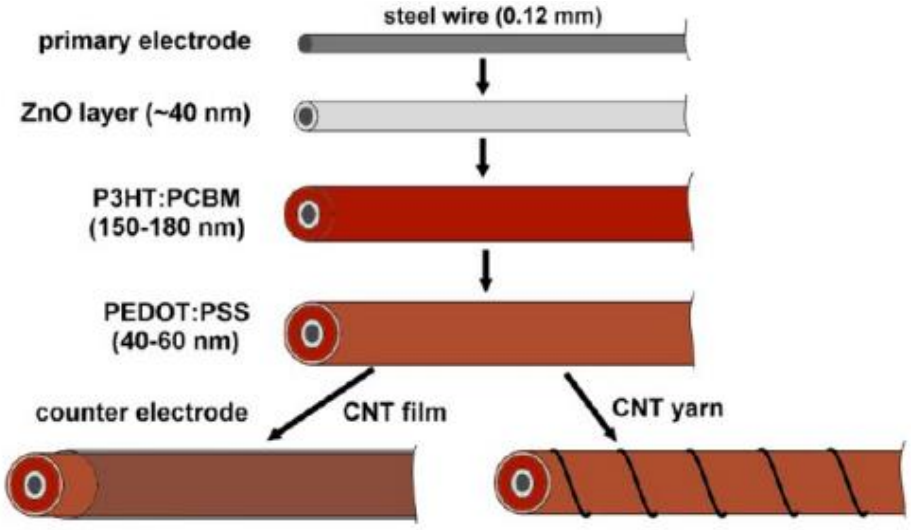

Figure 15. Schematic diagram of fabrication of wire-shaped polymer solar cells with two different architectures.[41]

1-8. Main challenges of wire-shaped solar cells

The high flexibility of the wire-shaped solar cells is a unique advantage that makes it quite capable for applications in wearable technologies. Flexibility of the substrate is directly related to their power conversion efficiency and stability. The greatest attraction to wire-shaped devices is its freedom from transparent conductive oxide (TCO) glass photovoltaic parts. Due to the unique shape (light weight, wearability, and ease of integration) compared to planar solar cells, wire-shaped solar cells have attracted considerable attention. However, the efficiencies of the cells are still much lower compared to the planar format. The power conversion efficiency will be largely decreased as the cell length is increased, since the electrical resistance of the fiber electrodes are linearly increased with the length of the fiber.[42] The challenge is to reach a balance between high efficiency and acceptable length. With the exception of PSCs, no reports of solid state electrolyte wire-shaped DSSCs are available; liquid electrolytes are mainly used for the wire-shaped DSSCs. Leakage of the electrolyte will be a challenge when sealing the wire cell at large scale. More efforts should be paid to solid-state electrolytes, which are particularly important for wire cells. Despite the described challenges, wire-shaped solar cells can be easily integrated into multifunctional devices. To this aim, more efforts should be focused on optimizing the structure and enhancing the performance of the solar cells.

1-9. Statement of problem

Most PV cells are large, planar, inflexible and brittle. Many more applications would arise if the PV cell could be integrated or even woven into a smooth, supple surface. In recent years, liquid junction solar cells (PECs or DSSCs) have received more and more attention from both academia and industry due to low cost, simple preparation methodology, low toxicity, and ease of production. Through continuous development, it was reported that most of the liquid junction solar cells were prepared by using TCO glass as a substrate for the working electrode. However, rigid TCO glass has restricted the adaptability during installation and application. To improve the adaptability, fabricating flexible cells has become a challenge.

1-10. Outcome from the thesis

Based on the preceding literature survey, it is recognized that there are only few publications related to electrodeposition of WO_3 on stainless steel flat substrates. These articles solely focused on changing the parameters of deposition voltage and time. In this research we have prepared electrodeposited WO_3/stainless steel thread as photoanode and platinum-coated stainless steel wire as counter electrode to prepare a wire format liquid junction solar cell. It is critically important to develop miniature energy harvesting and storage devices that are small, lightweight, and flexible in modern electronics. Conventional silicon wafer-based photovoltaic technologies cannot fully satisfy these requirements. Therefore, there is increasing interest in developing next-generation photovoltaic devices. One general and effective method to overcome the above

difficulties is to fabricate the cell into a new wire-shaped that can simultaneously enable them to be small, lightweight, flexible, and foldable. In addition, they could be easily scaled up for industrial production by textile technology. We have proceeded in three main aspects of liquid junction solar cells: 1) geometric comparison prepared with two different configurations: i) twisting the photoanode around a Pt-coated counter electrode and ii) replacing the stainless steel thread with tungsten wire and orienting the wires in a parallel manner. 2) to enhance the light absorption, we have isolated natural dyes and loaded them onto the electrodeposited WO_3/stainless steel thread in a dye sensitization scheme. For comparison, synthetic organic dyes that are suitable for the photovoltaic effect will be tested such as diketopyrrolopyrolles (DPP) and bis-(anthroquinones) (Red 177). 3) several alternative redox couples will be tested.

The electrochemical reaction rate of the redox couple I^-/I_3^- is of central importance for the functioning of liquid junction cells. Both electrodes are exposed to the electrolyte, and the efficiency of the cell is based on the reaction with the redox couple. 0.1 M KI and 0.01 M I_2 in DI water were prepared and tested. Alternatives to the I^-/I_3^- redox couple will be investigated by replacing the KI with tetraethylammonium iodide, tetrapropylammonium iodide, and tetrabutylammonium iodide with higher concentrations in organic solvent based electrolyte. We have used a UV-vis spectrophotometer to analyze the light absorption characteristics and XRD to determine the crystal change after annealing WO_3 at 350 ℃ for 1 hr. Results from electroanalytical methods such as cyclic voltammetry and linear sweep voltammetry will be discussed. Finally, the performance of the constructed DSSC will be tested to plot a current vs voltage curve and V_{OC}, J_{SC}, FF and η will be calculated.

Chapter 2. Experimental & Characterization

2-1. Preparation of peroxotungstic acid solution

WO_3 thin films were prepared by electrodeposition from a peroxotungstic acid ($H_2W_2O_{11}$) solution.[43] The precursor solution was prepared by dissolving enough sodium tungstate dihydrate ($Na_2WO_4 \cdot 2H_2O$, ACROS Organics) in 100 ml DI water to make a 30 mM solution, followed by adding 0.2 mL of 30% hydrogen peroxide (H_2O_2, Fisher chemical). A pale-yellow solution was initially formed, which faded after an hour. The initial pH of the $Na_2W_2O_{11}$ solution would rise to about pH 10. Concentrated nitric acid (HNO_3, Fisher Scientific) was added dropwise until a pH 2 was reached.

2-2. Electrodeposition of WO_3 film

The electrodeposition was performed with a potentiostat (Princeton Applied Research, Potentiostat/ Galvanostat Model 273 A), using Ag/AgCl as the reference electrode, and platinum wire as counter electrode as shown in Fig. 16. The electrodeposition was performed at a potential of – 0.45 V for 60 min. The conductive stainless steel thread (Adafruit Industry) was used as a working electrode for the deposition and annealed at 350 ℃ in air for 1 hr. The technique is based on the chemical reduction of peroxotungstic acid and the precipitation of a solid thin film onto the stainless steel thread substrate. For comparison to stainless 316L thread, indium doped tin oxide (ITO, Sigma Aldrich) glass

and tungsten wire (0.2 mm diameter, Alfa Aesar), were used as conductive substrates, and annealed at 350 ℃ in air for 1 h after deposition.

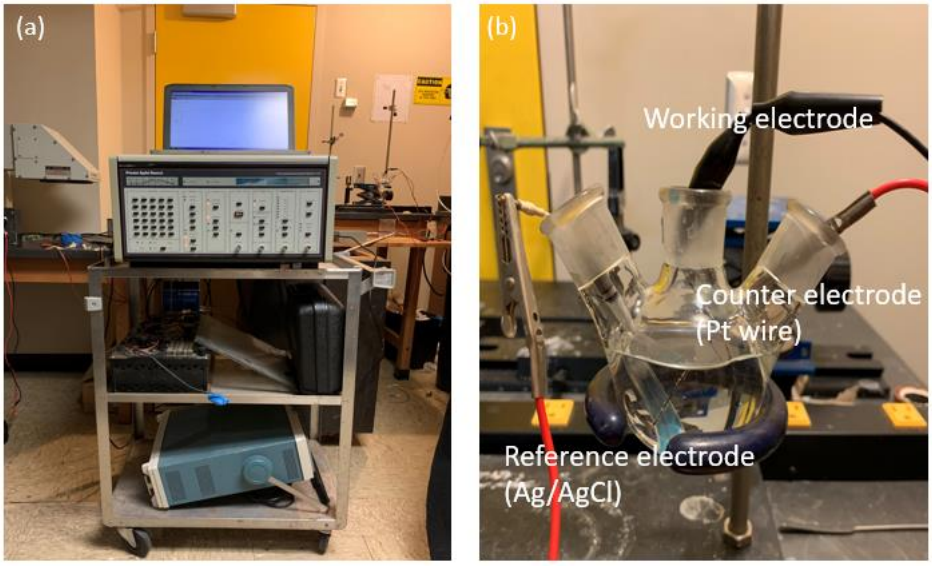

Figure 16. Picture of (a) potentiostat (Princeton Applied Research, Potentiostat/ Galvanostat Model 273 A) and (b) conventional three-electrode system.

2-3. Preparation of Pt-deposited counter electrode

Electrochemical preparation of the Pt deposition was conducted in a standard three electrode cell with Ag/AgCl reference electrode and Pt wire as counter electrode. The working electrode upon which the Pt particles was deposited onto stainless steel 302 wire (diameter: 0.25mm). Cyclic voltammetry with potential range of - 0.35 to + 0.35 V and scan rate of 50 mV/s for 30 cycles was conducted. Pt^{4+} ions in the aqueous electrolyte consisting of 2.0 mM chloroplatinic acid (H_2PtCl_6, Sigma Aldrich) in 1 M H_2SO_4 were reduced to deposit the Pt particles.[44]

2-4. PMMA latex coating onto counter electrode

To avoid contact between the working electrode and counter electrode, polymethylmethacrylate (PMMA) latex was synthesized by emulsion polymerization.[45] The monomer methyl methacrylate (MMA, Alfa Aesar) 3 mL was added to 25 mL distilled water under nitrogen in a three-necked round bottom flask equipped with thermometer and N_2 inlet. The polymerization was carried out at 70 ℃ where the initiator 2,2'-Azobis(2-methylpropionamidine) dihydrochloride (AIBN, Acros organics) was added to polymerize the MMA monomer for 2 h. The procedure involved for coating the Pt particles electrodeposited counter electrode, a dip coating method was employed. Adding 0.1 ml of prepared latex to DI water, into which the Pt-deposited counter electrode was immersed and dried in air at 80 ℃ for 12 h while the solution evaporated.

2-5. Preparation of electrolyte solution

Iodide (I^-)/triiodide (I_3^-) electrolyte solution was prepared by adding 0.415 g of potassium iodide (KI, Fisher Scientific) to 25 mL of DI water to make a 0.1 M solution. That was followed by adding 0.064 g of solid iodine (I_2, Fisher Scientific) crystals and stirring to make the solution nominally 0.01 M in triiodide. The pH 8 of the prepared solution was adjusted by adding 10% H_2SO_4 dropwise to pH 2. The solution was stirred 12 h in a dark container before use. Instead of H_2O as a solvent, acetonitrile was sometimes used as an organic solvent. For comparison, three different organic salts for the liquid electrolyte were studied. Table 1 summarizes the chemical structures of the organic salts studied. Electrolytes were prepared by combining 0.1 M solutions of

tetraethylammonium iodide (TEAI), tetrapropylammonium iodide (TPAI) or tetrabutylammonium iodide (TBAI) in acetonitrile with enough I_2 to make the solution 0.01 M in triiodide. Without pH adjustment the solution was stirred 3 h in a dark container before use.

Table 1. Chemical structure of TEAI, TPAI, and TBAI

Chemical	Chemical structure	MW (g/mol)
Tetraethylammonium Iodide (TEAI)	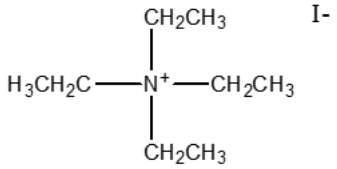	257.16
Tetrapropylammonium Iodide (TPAI)	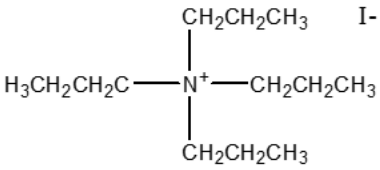	313.26
Tetrabutylammonium Iodide (TBAI)	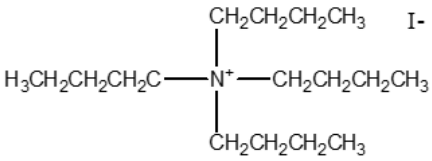	369.17

2-6. Dye-sensitized electrode fabrication

To fabricate the natural dye-sensitized electrodes, the electrodeposited WO_3/stainless steel thread was immersed in an extract from blackberries and raspberries for 24 hr. The extraction was performed by crushing 100 g of natural fruits in a 50 mL solution of

methanol/acetic acid/water (25:4:21) and filtered with Whatman 541 – 110 mm diameter filter paper.[46] After dye transfer, the electrode was dried at 60 ℃ in air for 1 h. Fig. 17 shows a schematic of the stages involved in the fabrication of the natural dye-sensitized solar cell (NDSSC). Fig. 18 shows a schematic diagram of the completed NDSSC. The natural dye-sensitized and the Pt-coated wire electrodes were assembled to form a solar cell by twisting around each other and inserting into a transparent heat shrink tube (1/8 inch diameter). The tube was employed to hold the iodide/triiodide electrolyte necessary to form a liquid junction with the semiconductor electrode and was sealed with epoxy cement to avoid any leakage.

For comparison, non-natural organic dyes suitable for the photovoltaic effect, such as diketopyrrolopyrolles (DPP) and bis-(anthroquinones) (Red 177), were also tested. These organic dye solutions were prepared by adding sufficient material to make a 0.3 mM dye solution in dichloromethane (CH_2Cl_2) and stirred for 12 h at room temperature. The electrodeposited WO_3/stainless steel thread was then immersed in the prepared organic dye solutions for 24 h. After dye transfer, the electrode was dried and the cell was assembled in the same manner as the NDSSC.

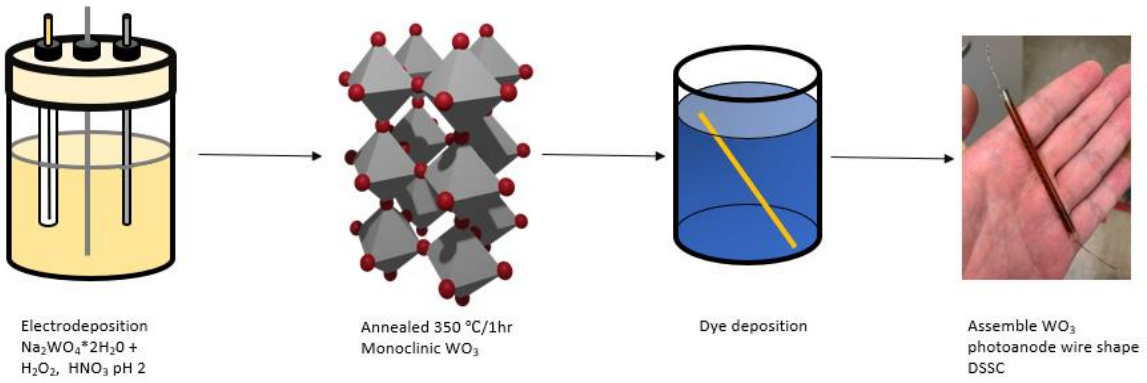

Figure 17. Schematic of sequence for assembling natural dye sensitized solar cell.

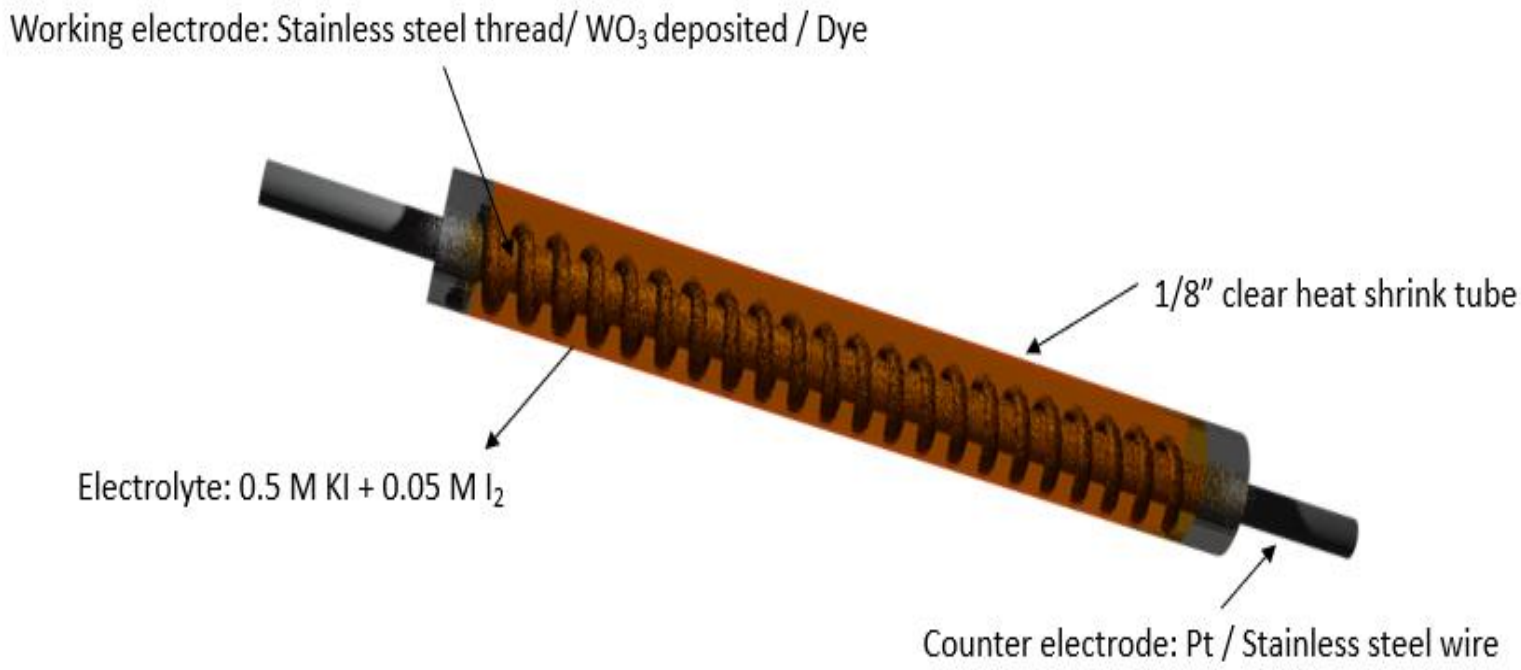

Figure 18. Schematic diagram of assembled DSSC in twisted orientation wire shaped liquid junction solar cell.

2-7. Characterization techniques

The surface morphology of the synthesized PV thread was investigated using a scanning electron microscope (JEOL JIB-4500 multi beam system). The crystalline phase and average crystal size were determined by an X-ray diffractometer (Bruker, X8 PROSPECTOR).

2-8. Optical properties

The absorbance of the electrodeposited WO_3 onto ITO coated glass was analyzed by UV-vis spectroscopy (Agilent 8453, UV-vis spectrophotometer system). The UV-vis absorption spectra of the WO_3 films were recorded in the wavelength range from 190 to 1000 nm. All solution samples were tested with 25 μL of solution diluted into a 3 mL cuvette filled with DI water.

2-9. Electrochemical characterization

Electrochemical measurements on WO_3 thin films on stainless steel thread were carried out by cyclic voltammetry (CV) using a PAR potentiostat in a three-electrode cell configuration with 1.0 M H_2SO_4 as the electrolyte. A platinum wire was the counter electrode, Ag/AgCl was the reference electrode, and WO_3 electrodeposited on steel thread was the working electrode. The potential ranged from -1 to 1 V with 50 to 100 mV/s scan rate.

2-10. Photo-oxidation (Photocurrent) activity measurement

The photo-oxidation activities of the WO_3 electrodeposited onto stainless steel thread was compared with WO_3 electrodeposited onto ITO glass substrates. The measurement of the films was determined by the linear sweep voltammetry upon light irradiation using the 500 W xenon lamp light source (Newport solar simulator). The setup for the photo-oxidation measurement can be seen on Fig. 19. Three-electrode cell configuration with 1.0 M H_2SO_4 as the electrolyte, and a platinum wire was the counter electrode, Ag/AgCl was the reference electrode, and WO_3 electrodeposited on steel thread (or WO_3 electrodeposited on ITO) was the working electrode. The potential ranged from 0 to 1 V with 10 mV/s scan rate was used to evaluate the photo-oxidation of the WO_3 films.

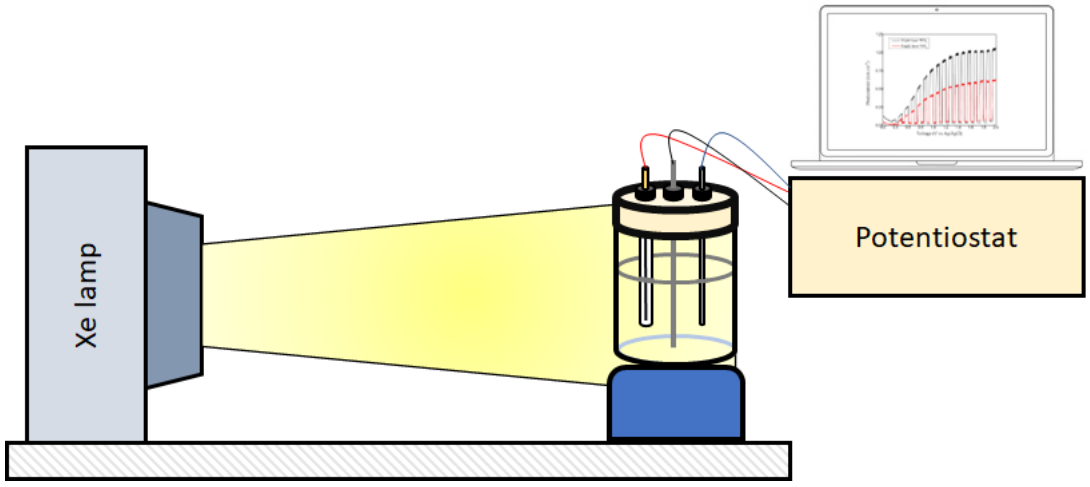

Figure 19. Schematic diagram of photo-oxidation (photocurrent) measurement.

2-11. Photoactivity measurement

To compare for the photovoltaic activity of the films, a two-electrode cell setup was used. Fig. 20 shows the schematic diagram of the setup for current density vs voltage characterization of the prepared wire-shaped DSSCs. The light source was a 1000 W xenon lamp (Newport solar simulator) with 71 mW/cm^2 illumination (measured by Newport, Power meter, model 1918-C), and the measurements were performed by observing the photocurrent while sweeping the potential at a constant rate of 10 mV/s.

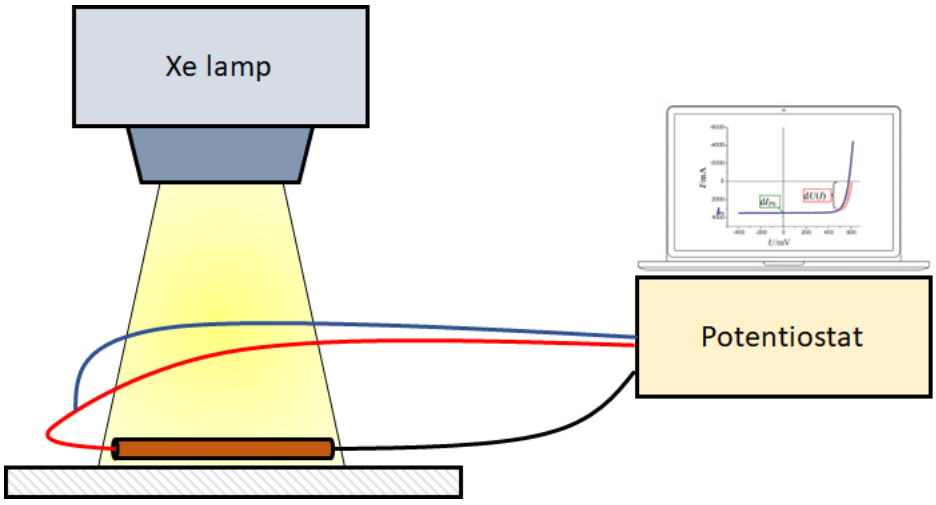

Figure 20. Schematic diagram of current density vs voltage measurement during Xe lamp light illumination.

As shown in Fig. 21, in a two-electrode cell system, the reference electrode connector is shorted to the counter electrode (negative electrode in our setup) and set apart from the WO_3/stainless steel thread working electrode held at ground potential.

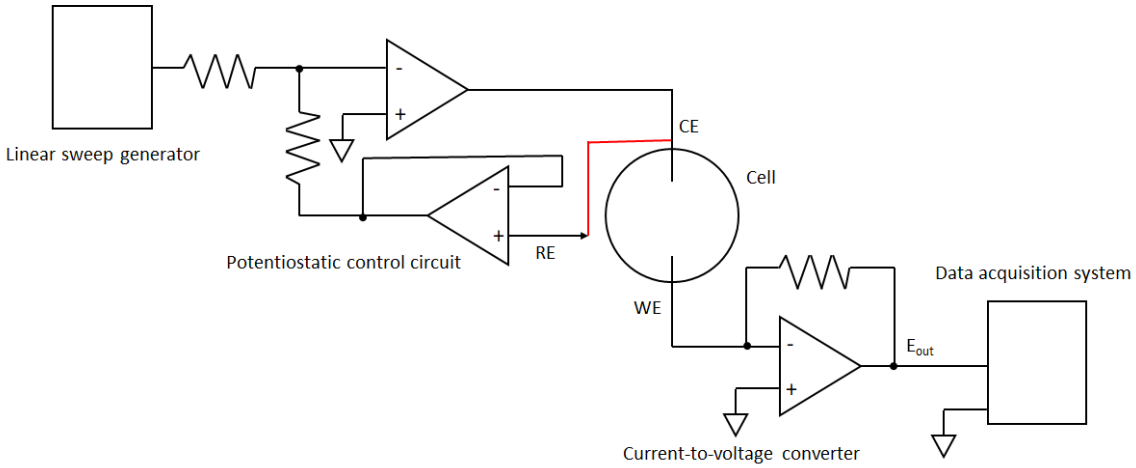

Figure 21. Diagram of potentiostat with a two-electrode setup.[47]

Both the reference and test cells were ensured to be placed at the same spot under the solar simulator during measurement. The current density vs voltage data was obtained by recording the generated photocurrent upon the application of an external potential bias. The voltage was swept in the direction of open circuit voltage to short circuit. The obtained data were plotted to extract the photovoltaic parameters, including open circuit voltage (V_{OC}), short circuit current (J_{SC}), fill factor (FF), and maximum energy conversion efficiency (η).

Chapter 3. Results & Discussion

3-1. Surface morphology of the fabricated cell

The surface morphology of the electrodes as they were progressively modified was characterized by SEM. Fig. 22 and 23 show film formation by electrodeposition and SEM images of each stage, respectively. In first state, WO_3 nucleates on the electrically active surface, and subsequently grows (Stage 2). After there are no longer any sites on the substrate for deposition (Stage 3), continued film growth must occur on top of the existing WO_3 deposit (Stage 4). Fig 24 shows images of electrodeposited Pt particles coated onto the stainless steel wire substrate. A uniform coating of Pt particles covering the surface of stainless steel 302 wire can be seen in Fig 24(b). To avoid contact between working and counter electrodes, synthesized PMMA latex particles were prepared. From Fig 25, after the polymerization was done, uniform nanoparticles of 0.25 μm diameter PMMA latex were confirmed by particle size distribution. SEM images of annealed WO_3 deposited on stainless steel microfibers and other cell parts are shown on Fig. 26. Fig. 26(a) shows WO_3 electrodeposited on ITO with cracks after annealing at 350 ℃ in air and Fig. 26(b) shows the smooth surface of stainless steel thread without any treatment. From Fig. 26(c) WO_3 electrodeposited on stainless steel thread and twisted around Pt-deposited stainless steel wire can be seen. Fig. 26(d) shows the morphology of the WO_3 film with uniform cracks after annealing at 350 ℃ for 1 h in air. The coating of the films shows clearly that the WO_3 is surrounding the individual fibrils with cracks around the fibers, indicating shrinkage of the deposited film during annealing. We assume the

individual channels between WO_3 grains can enhance the surface area of the contact between the electrode/electrolyte interface while adding flexibility to the cell. To achieve efficient fiber photoelectrochemical behavior, the key points are uniform functional layers and effective interfacial contact for light collection and charge carrier generation.[48] As to the purpose of enhancing the surface area, as shown by the image in Fig 26(e), by using an electrodeposition method for film fabrication, we can see that the individual fibrils are uniformly coated with WO_3. Fig. 26(f) shows the image of PMMA latex coated onto Pt-deposited stainless steel wire. Since the cell design involved twisting the working electrode around the counter electrode, the purpose of the latex coating was to avoid their electrical contact with each other. We had to create an electrically nonconductive porous structure which could transport the redox couple between the two electrodes while acting as a protective insulating layer.

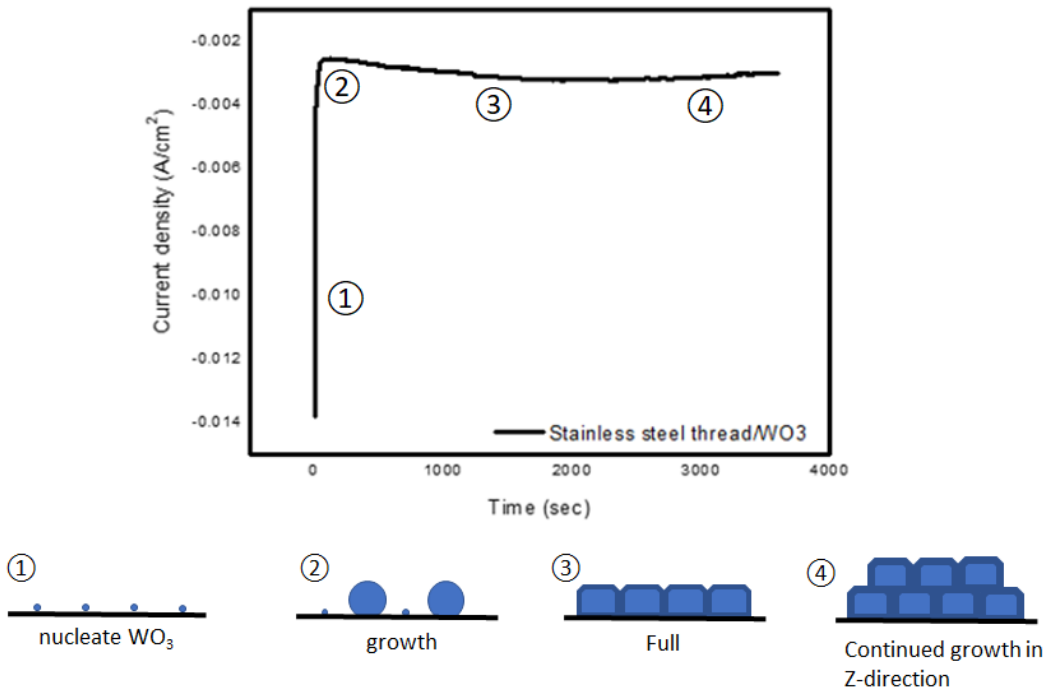

Figure 22. Current density vs Time curve during electrodeposition with film formation.

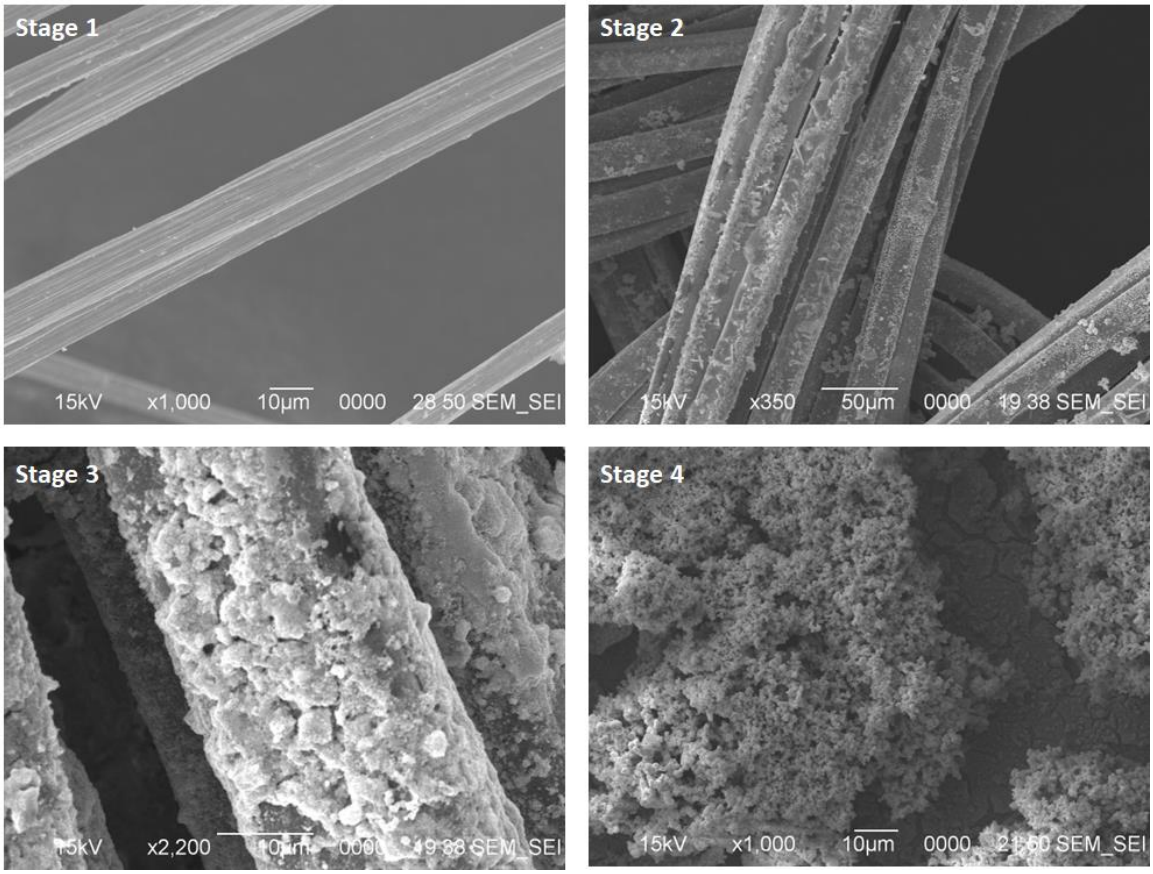

Figure 23. Comparison of morphology change of corresponding each stage during electrodeposition.

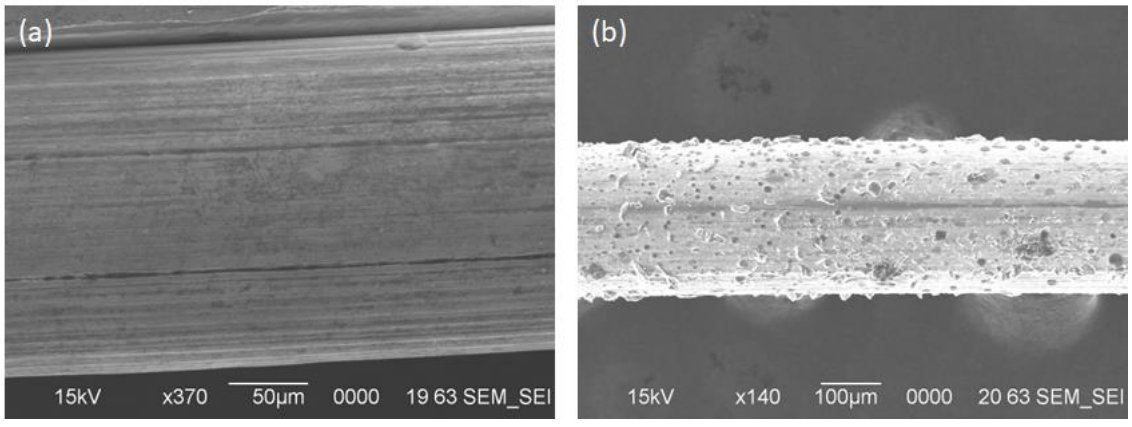

Figure 24. SEM images of Pt particles electrodeposited on stainless steel 302 wire (a) before and (b) after.

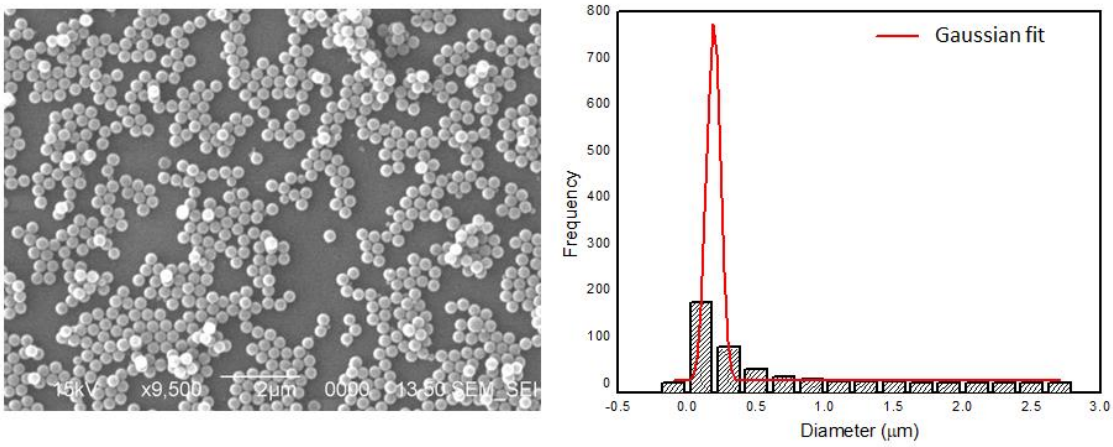

Figure 25. SEM images of PMMA latex and particle size distribution.

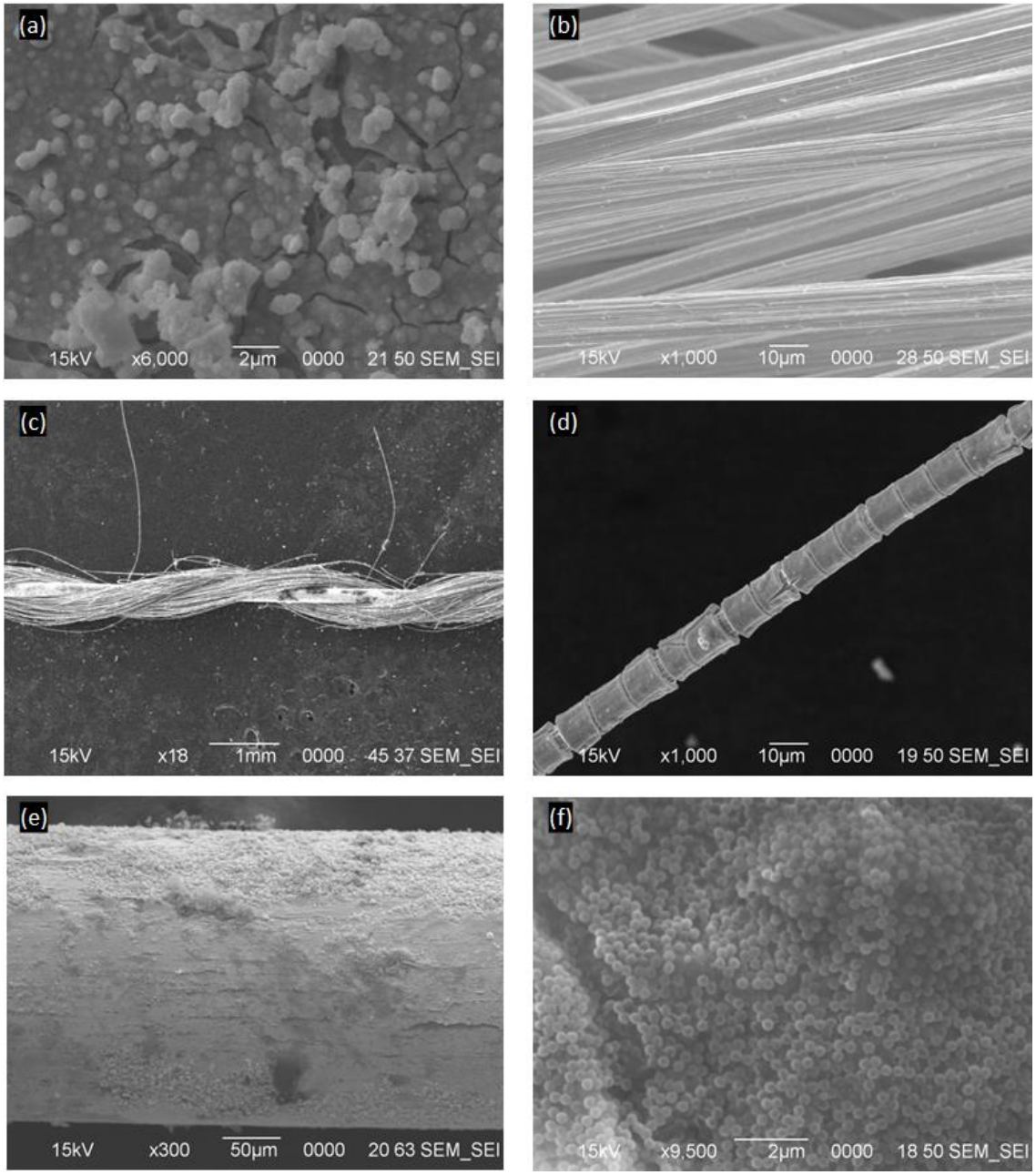

Figure 26. SEM images of a fabricated PV microfiber cell with (a) WO_3 electrodeposited on ITO, (b) uncoated stainless steel thread, (c) twisted WO_3 electrodeposited on stainless steel around Pt-deposited stainless steel wire, (d) WO_3 electrodeposited on stainless steel microfiber with annealing at 350 ℃ for 1 h in air, (e) 300 X magnification of PMMA latex coated and (f) 9500 X magnification of PMMA latex coated on Pt deposited stainless steel wire.

3-2. Optical properties

UV-vis absorption spectra of WO_3 deposited on ITO with adsorbed natural dye are displayed in Fig. 27. From Fig. 27(a) and (b), the direct bandgap (E_g) of nanomaterials was calculated by a Tauc plot using the equation;

$$(\alpha h\nu) = A(h\nu - E_g)^{1/2}$$

where $h\nu$ is the photon energy, α is the absorption coefficient, and A is a constant for the specific materials.[49] The absorption edge of the electrodeposited WO_3 on ITO was around 355 nm, and the estimated direct bandgap (E_g) was around 2.87 eV. The optical properties of WO_3 are directly related to its bandgap, which in turn is related to the oxygen vacancy concentration.[50] Higher vacancy concentration leads to smaller bandgap energy. In the visible domain of the spectrum higher than 400 nm, there is no absorption, so that the appearance of the WO_3 deposited on ITO was transparent. Fig. 28(a) and (b) depict the absorption spectra of prepared natural dyes of blackberry and raspberry, respectively. The absorption spectra showed the presence of distinct absorption peaks in the visible region for each dye. The blackberries and raspberries used for the natural dyes contain anthocyanins, which are responsible for the colors of the dyes and their photosensitizing performance. The chemical structure of the photochemically reactive cyanidin group contained in anthocyanins can be seen on Fig. 29 with electron transfer mechanisms.[51] The maximum absorption peak of blackberry dye appears at the visible region at 560 nm and raspberry dye at 530 nm.

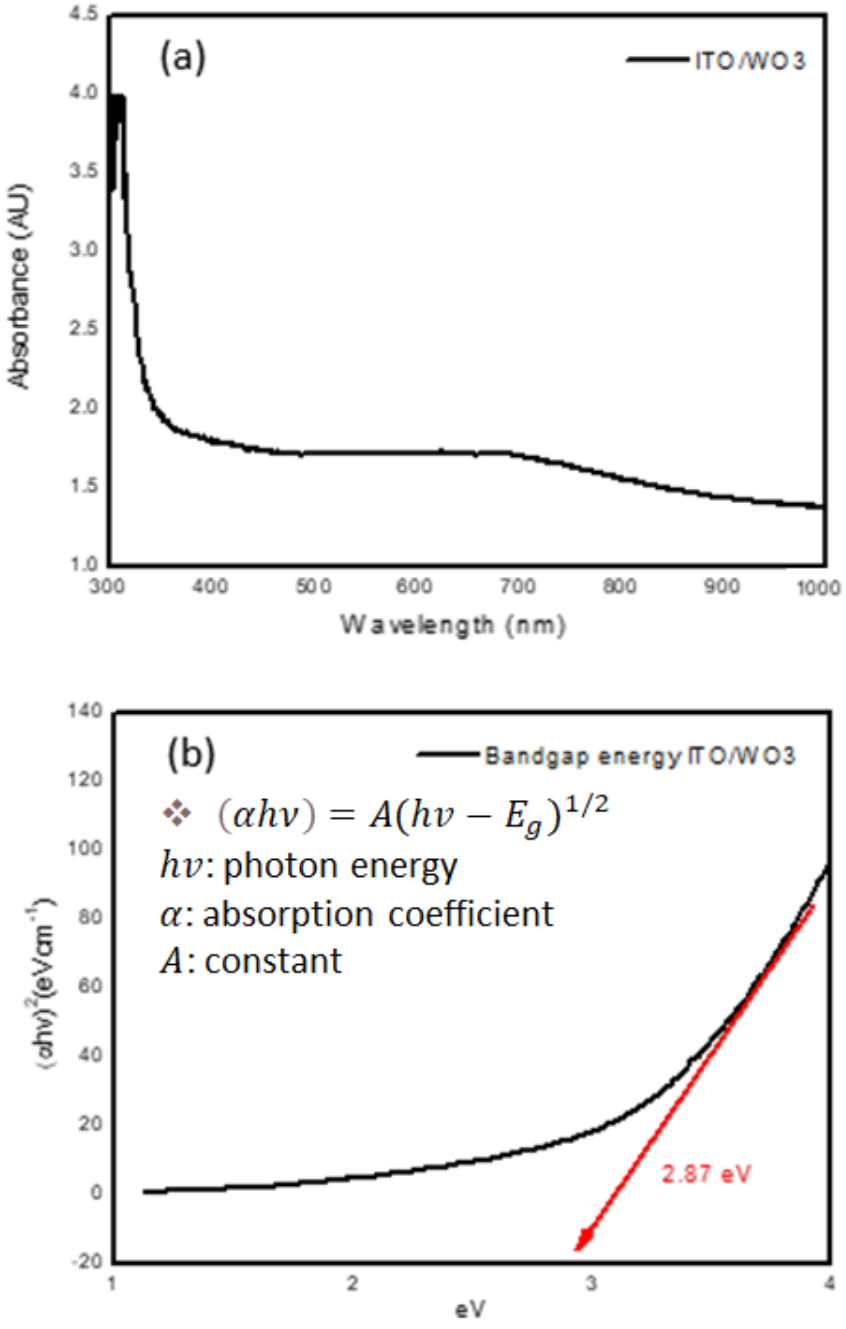

Figure 27. Comparison of UV-vis spectra of (a) ITO/WO_3, ITO/WO_3/dye (raspberry), and ITO/WO_3/dye (blackberry). (b) bandgap energy of WO_3 electrodeposited on ITO after annealing at 350 ℃ for 1 h,

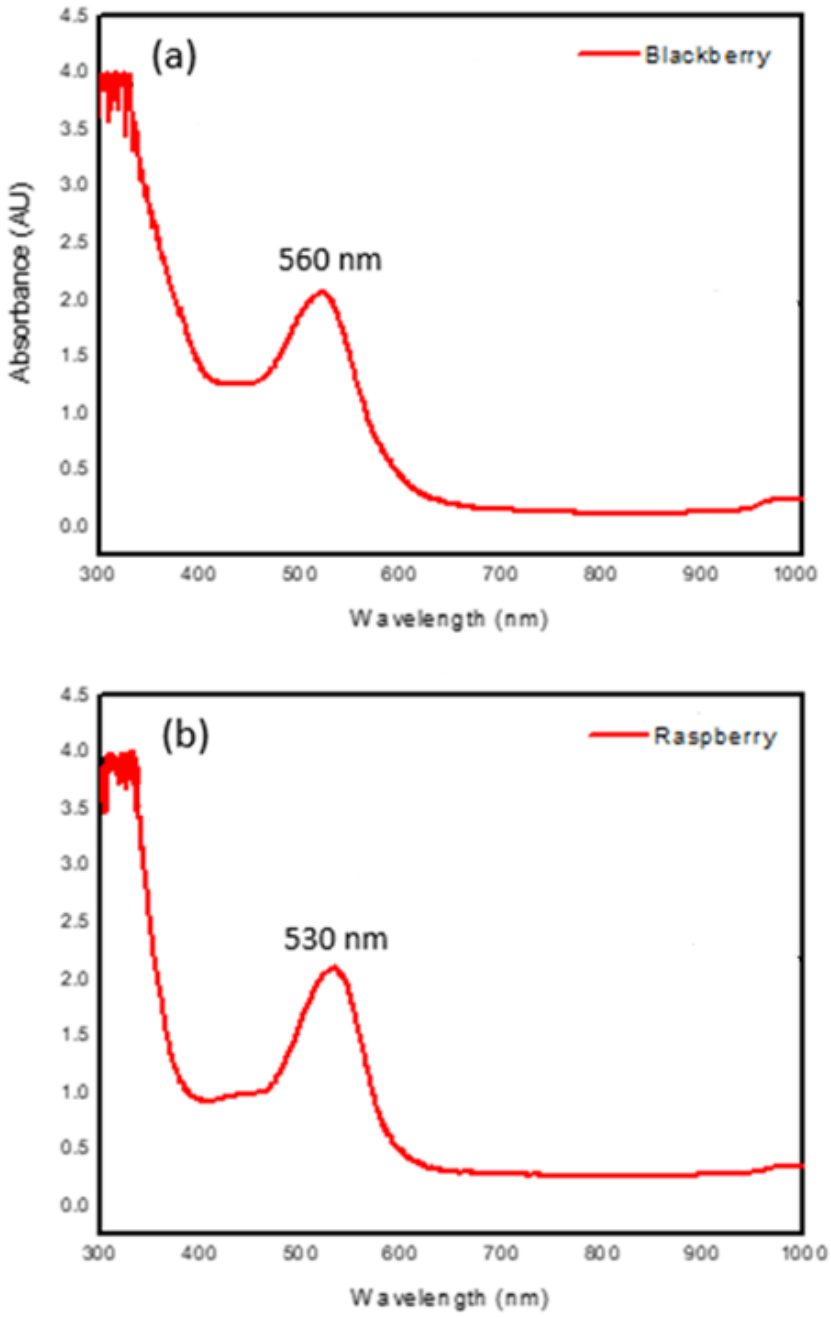

Figure 28. Comparison of UV-vis spectra of (a) blackberry dye, and (b) raspberry dye.

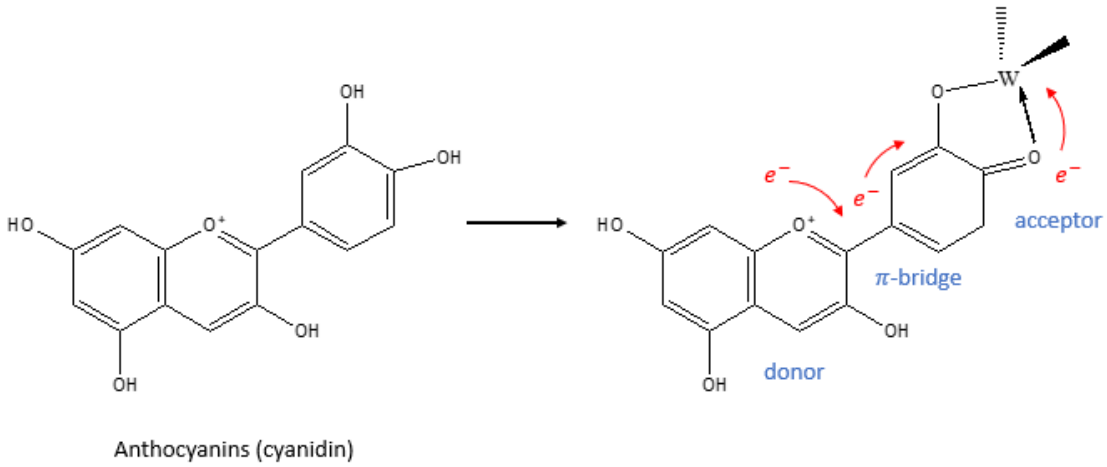

Figure 29. Chemical structure of cyanidin contained in natural anthocyanin dyes.

Fig. 30 displays the UV-vis absorption spectra and chemical structure of the synthetic organic dyes employed. From Fig. 30(a) the UV-vis spectrum of DPP shows two main absorption peaks between 300 to 400 nm, which corresponds to UVA (310-400 nm) and UVB (280-315 nm) absorption regions. Fig. 30(b) shows the UV-vis spectrum of Red 177 with maximum absorbance at 580 nm and a slightly lower wavelength maximum at 510 nm.

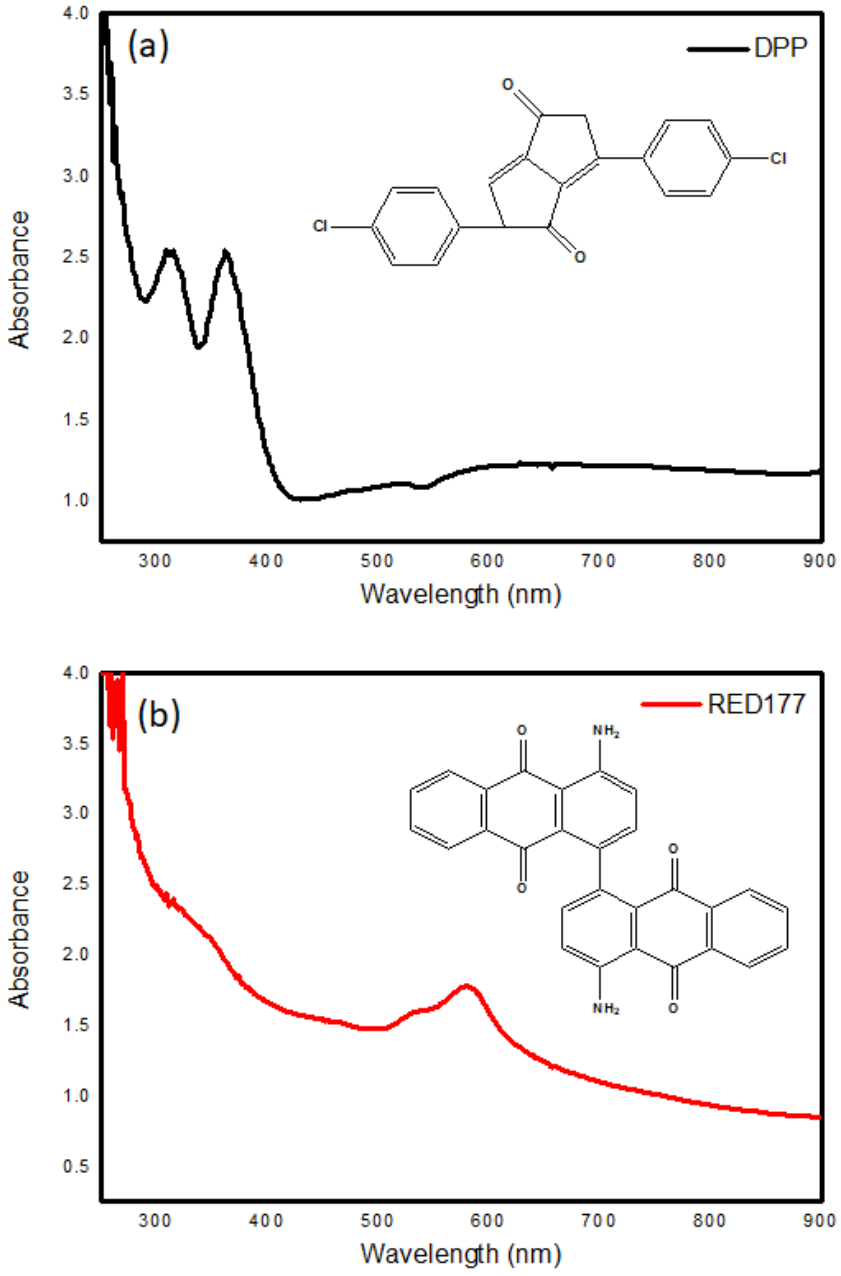

Figure 30. Solutions of UV-vis absorbance with chemical structures for (a) DPP and (b) RED 177 organic dyes.

Comparison of the optical properties of the prepared inorganic and organic iodide salts is shown in Fig. 31(a) and (b) respectively. All samples were prepared by adding 25 µL electrolyte solution (0.1 M iodide salts + 0.01 M I_2 + solvent (H_2O or acetonitrile)) to a cuvette filled with DI water. From Fig. 31(a), two main characteristic absorption peaks at 280 nm and 360 nm correspond to I_3^-.[52] Relatively high concentrations of iodide ions compared to the I_2 concentration pull more iodine into solution to form triiodide ion, giving rise to a large increase in the absorption. The absorption spectra of organic iodide salts in Fig. 31(b) with extra CH_2 groups slightly shift the spectrum toward longer wavelengths. The light attenuation in the PV cell due to absorption by the electrolyte will be directly related to its performance. However, the size of cation in the electrolyte is one of the factors that will affect the value of the V_{OC}. If the size of a cation is smaller, it can adsorb more strongly to the WO_3-electrodeposited area and change the position of the Fermi level to some extent.[53]

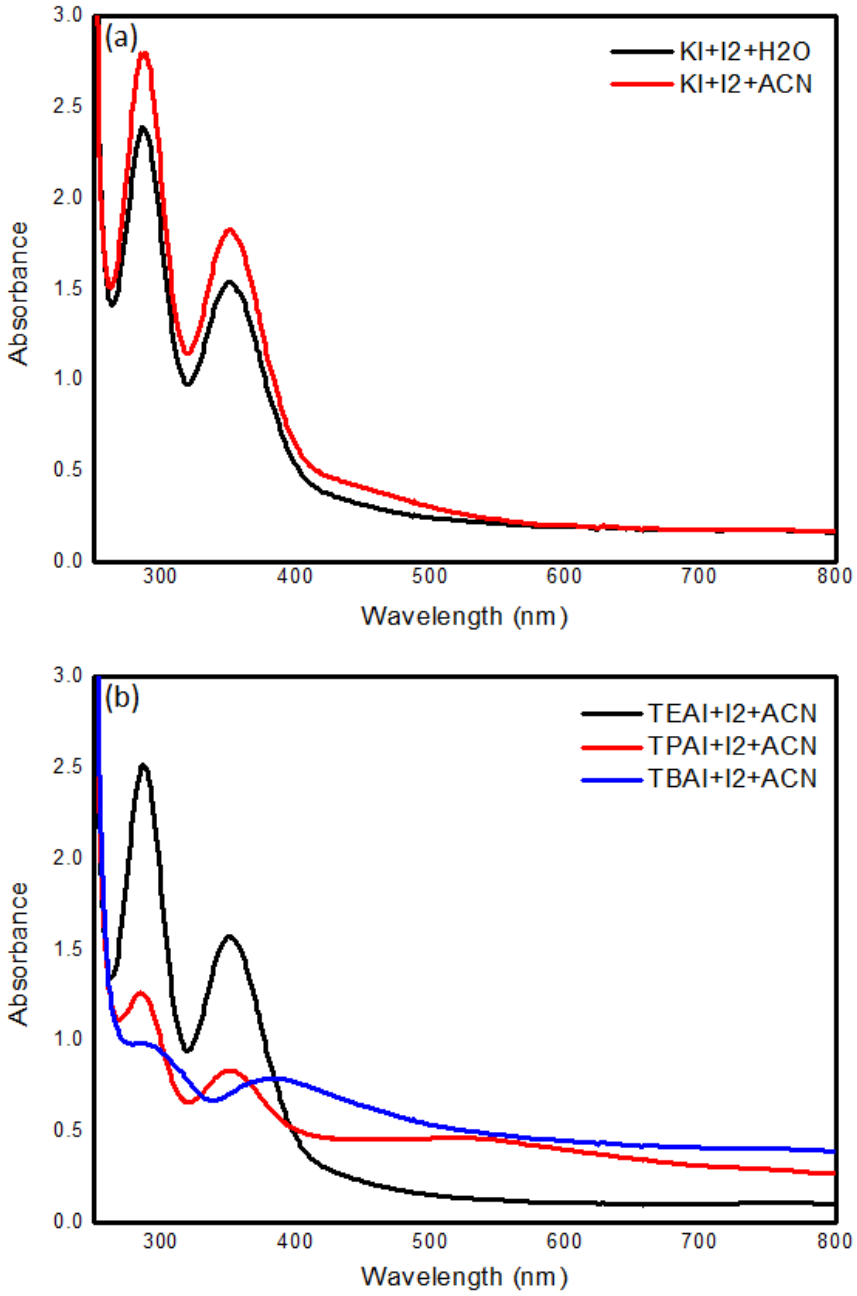

Figure 31. Comparison of UV-vis spectra of (a) inorganic iodide salts with H_2O (pH 2) and acetonitrile as a solvent and (b) organic iodide salts with acetonitrile as a solvent.

3-3. Crystal structure

WO_3 is a series of complicated materials with complex polymorphism and defect chemistry. Its various crystal phases include monoclinic, tetragonal, orthorhombic, cubic, triclinic, and hexagonal.[54] Among these various structures, the monoclinic structure is favorable for photoelectrochemical cells due to its stability at room temperature.[55] These polymorphic phases are highly sensitive to temperature and pressure changes. From Fig. 32(a), bare stainless steel threads before/after annealing at different temperatures for 1 h are compared. Before annealing the stainless steel thread, the 2θ angle of the two main peaks corresponds to the hexagonal structure of Cr at 43.6° and cubic structure of $Fe_{0.7}Ni_{0.3}$ at 44.7°. The elemental analysis of stainless steel thread using X-ray fluorescence (XRF) is shown in Fig 34 and Table 2, for which the XRD peaks agree with the elemental analysis. The FWHM (or peak intensity) of the annealed $Fe_{0.7}Ni_{0.3}Cr$ decrease as the temperature increases due to the release of internal stress and grain growth. These results are consistent with Etienne's work[56] and Xiong et al.[57] Fig. 32(b) shows the WO_3 electrodeposited stainless steel thread with different annealing temperatures. There are no diffraction peaks for annealing at 50 and 150 ℃ for 1h except for the peaks of the stainless steel thread. The low intensity peaks near 24 and 30° belonging to WO_3 are observed at an annealing temperature of 250 ℃ for 1 h, revealing the crystallinity transition. When the annealing temperature increased to 350 ℃, peaks appeared at 2θ = 23.1°, 23.6°, and 24.2°, which are associated with crystalline planes (002), (020), and (200), respectively, of the monoclinic structure. Annealing at 450 ℃ showed the phase transition of monoclinic to hexagonal. This result revealed that the crystal type of the WO_3 can be controlled by annealing temperature.

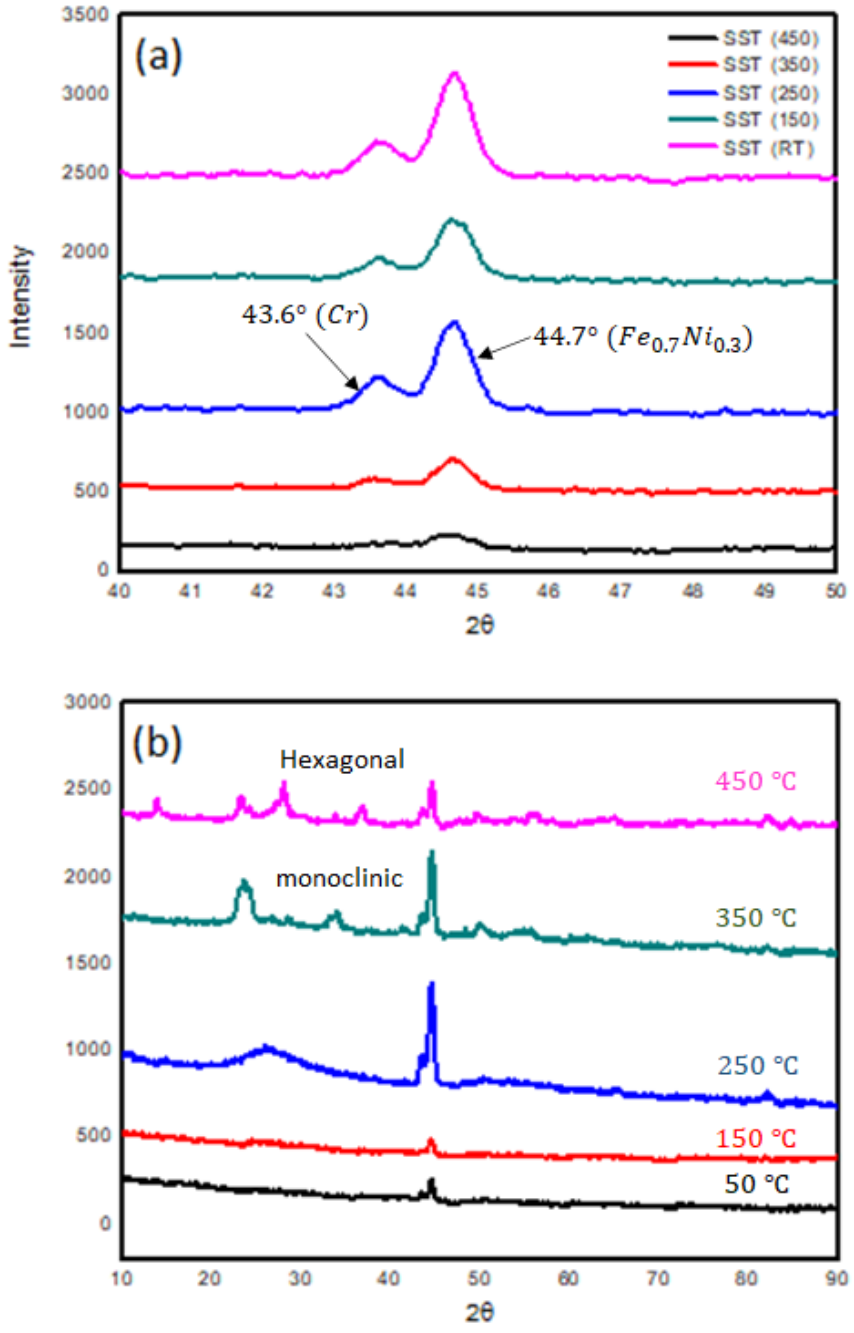

Figure 32. Comparison of XRD patterns after annealing at different temperatures for 1 h. (a) stainless steel thread and (b) WO_3 electrodeposited stainless steel thread.

From Fig. 33(a) the WO_3 electrodeposited film before annealing shows the orthorhombic phase of hydrated ($WO_3 \cdot H_2O$). Fig 33(b) displays the effect of different times of deposition after annealing the samples at 350 ℃ for 1 h in air. The annealed WO_3 films with more deposition time showed enhanced peak intensity. Curve fitting of the 350 ℃-annealed WO_3 film peaks is shown in Fig. 32(c). After transferring the dye to the deposited film, it can seen that the decreased diffraction peak intensity of the main peaks from Fig. 33(d) indicates that the surface of the film is covered with dye molecules.

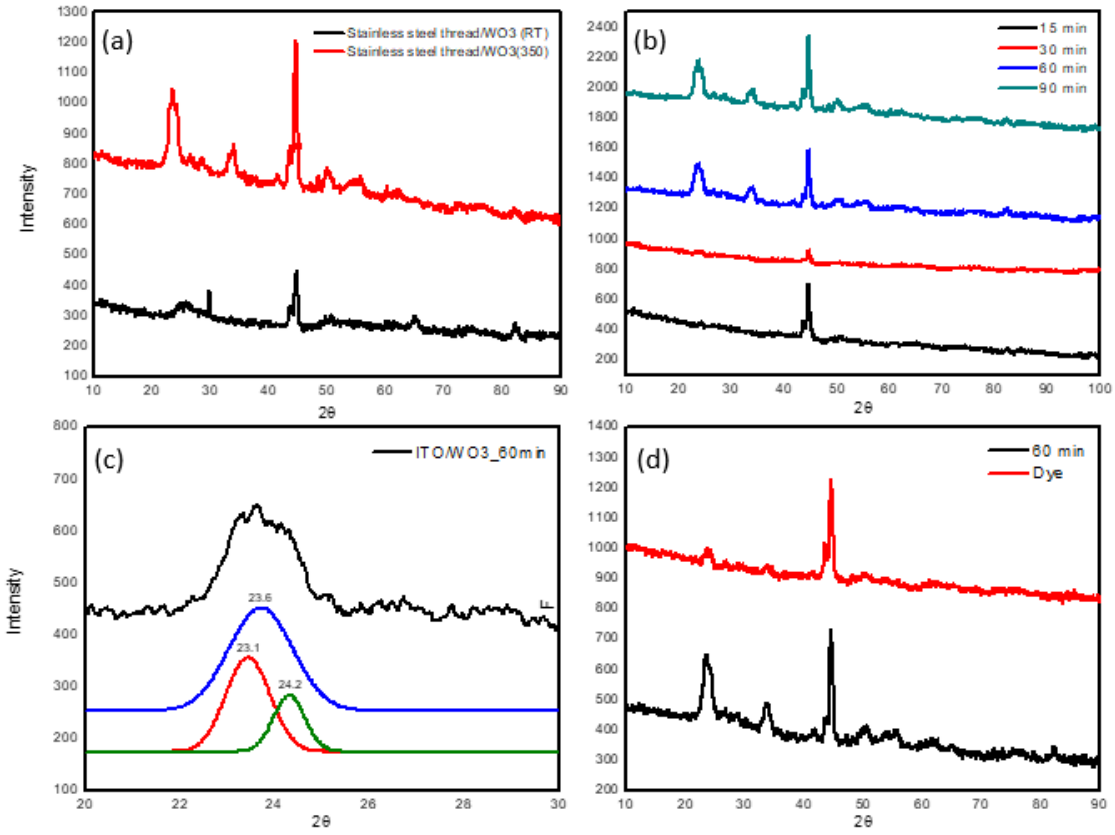

Figure 33. Comparison of XRD patterns of WO_3 electrodeposited on stainless steel thread after annealing at 350 ℃ in 1 h at air. (a) before and after annealing WO_3, (b) different deposition time, (c) curve fit angle from 22 to 25 °, and (d) before(black)/after(red) dye transfer.

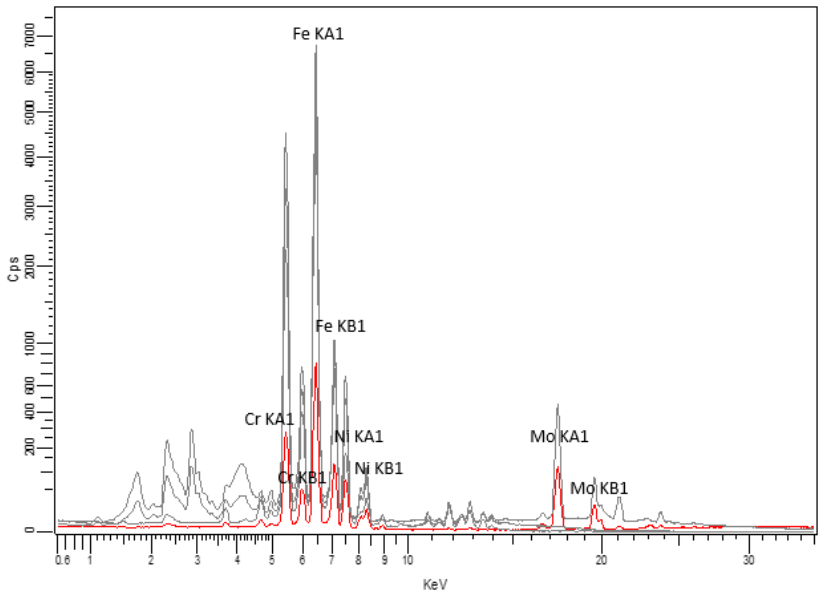

Figure 34. XRF analysis of stainless steel thread.

Table 2. XRF element analysis of control stainless steel thread in weight percent.

Cr	17.5%	Mo	2.19%	Fe	68.3%	Ni	9.32%

3-4. Electrochemical measurement

To evaluate the electrochemical behavior of electrodeposited WO_3 on stainless steel thread, a typical CV curve was compared with ITO substrate and stainless steel thread, as shown in Fig. 35. There is a peak for surface reduction and reoxidation around -0.2 V and near 0.0 V due to the electron transfer, respectively. In Fig. 35(b), the steep rise in current above 0.4 V indicates oxidation of the stainless steel thread. From the obtained CV curves, the following formula was used to calculate the areal capacitance of the film.

$$C = {\int I(V)dV}/{A \cdot K \cdot \Delta V}$$

where $\int I(V)dV$ is the area under the curve, A is the area of the working electrode, K is the scanning rate in mV/s, and ΔV is the potential window in volts.[58] By comparison of the calculated areal capacitance 68.9 mF/cm^2 was measured after WO_3 deposition onto ITO, and 116 mF/cm^2 was measured after depositing WO_3 on stainless steel thread. Comparison of the area and the calculated capacitance indicates an increase after deposition of WO_3 with annealing at 350 ℃ for 1 h.

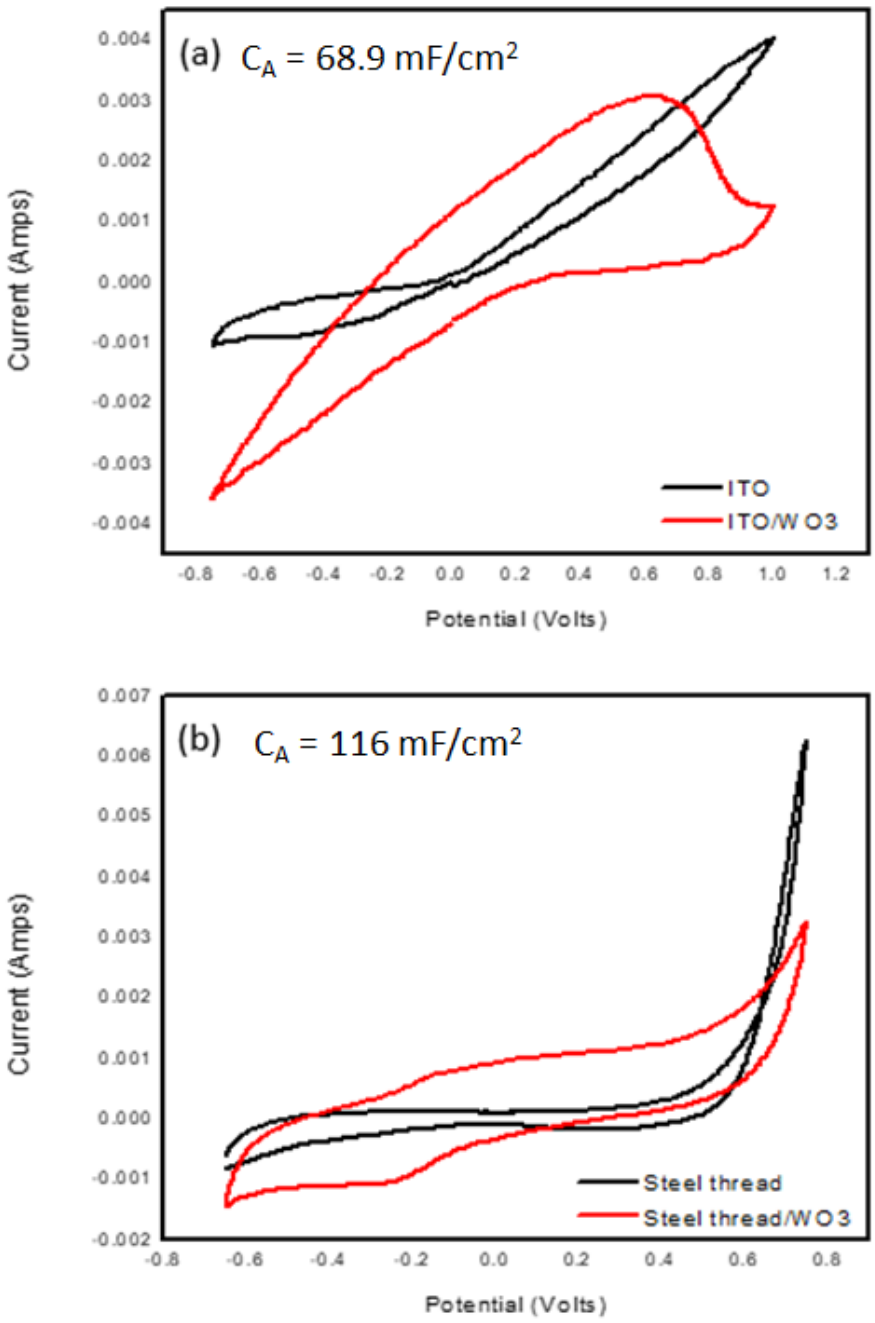

Figure 35. Comparison of cyclic voltammetric curves in 1 M H_2SO_4 electrolyte with scan rate of 100 mV/s for (a) ITO with and without WO_3, (b) plain stainless steel thread and with WO_3 film. All the deposited WO_3 films annealed 350 ℃ for 1 h.

From Fig. 36, CV curve of reactivity and reversibility of the iodide/triiodide couple in water and acetonitrile are compared. From Fig 36(a) when DI water was used as a solvent, two pairs of positive current peaks correspond to oxidation reaction of I_3^-/I^- can be seen.[59] The separation of redox peak in the CV curves was broad with no clear indication of reduction reaction implying that the reversibility of the I_3^-/I^- was not good. However, from Fig 36(b), using acetonitrile as a solvent. Clear indication of two pairs of oxidation and reduction peaks were observed which indicates the reversibility of the redox couple was good. The following reactions can occur represent as

$$I_3^- + 2e^- \rightarrow 3I^-$$

$$3I_2 + 2e^- \rightarrow I_3^-$$

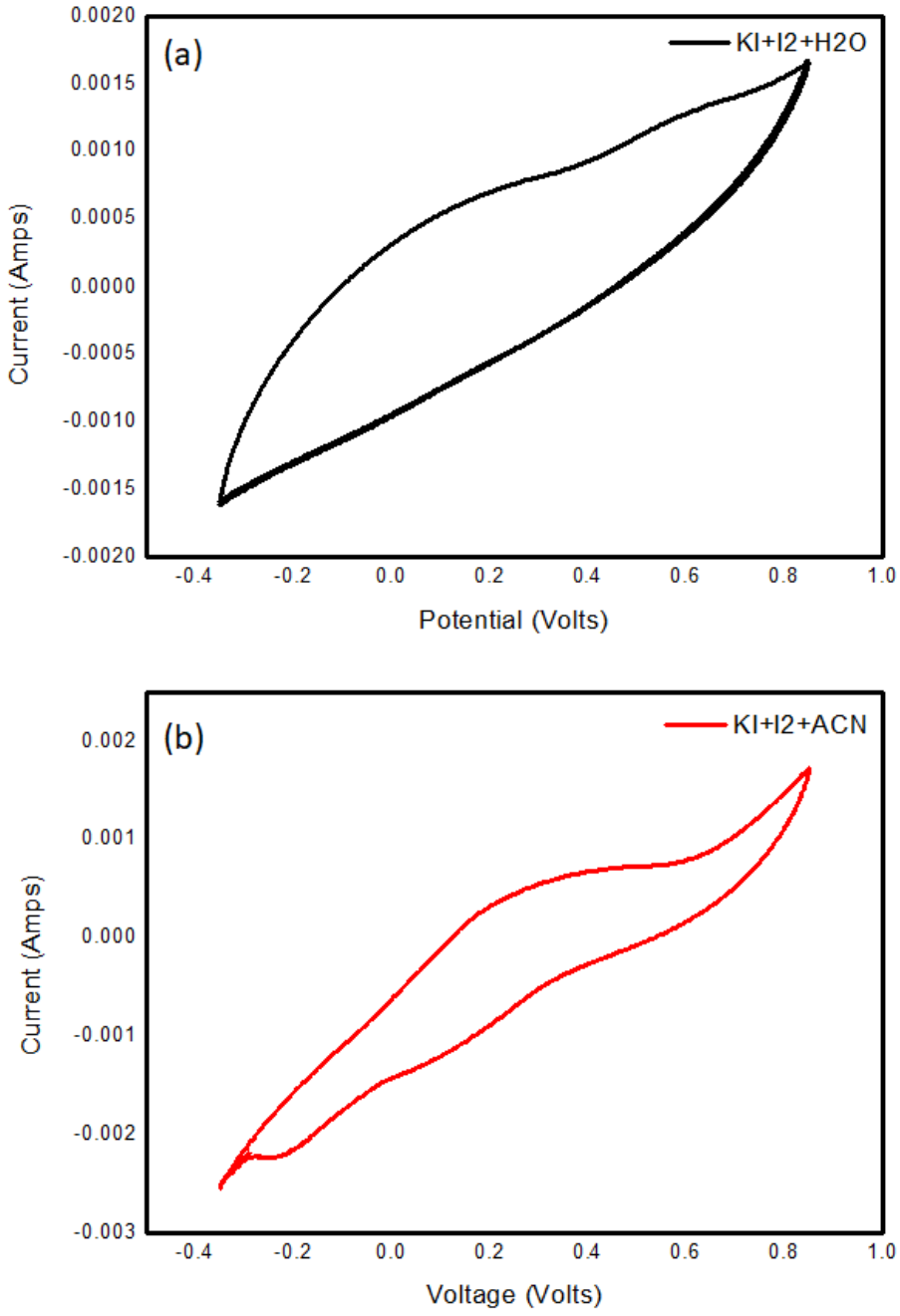

Figure 36. Comparison of cyclic voltammetric curves of electrodeposited WO_3 on stainless steel thread with iodide/triiodide couple in (a) water and (b) acetonitrile with scan rate of 100 mV/s.

3-5. Photoactivity measurement

To measure the photoactivity of the films, oxygen evolution behavior of WO_3 in the dark and under illumination for the ITO and stainless steel thread are compared in Fig 37. The results show that the different substrates did influence the photoactivity. Minimal anodic current was observed at the WO_3-deposited ITO and stainless steel thread electrodes within the potential range from 0 to 1.0 V in the dark. In Fig. 37(a), for WO_3 deposited on ITO, the onset potential was found to be 0.2 V vs AgCl, which is in line with the onset potential of photoelectrochemical oxygen evolution for WO_3.[60] A current of 107 $\mu A/cm^2$ was observed at 0.7 V using ITO substrate. From Fig. 37(b) it is confirmed that for plain stainless steel thread with and without illumination there was no change. After depositing the stainless steel thread with WO_3, as shown in Fig. 37(c), a photocurrent of 317 $\mu A/cm^2$ was observed at 0.7 V. Also, under the same conditions, the photo-response by periodically blocking the light during the test can be seen on Fig. 37(d). This is a clear indication that charge carriers are being photogenerated in the WO_3.

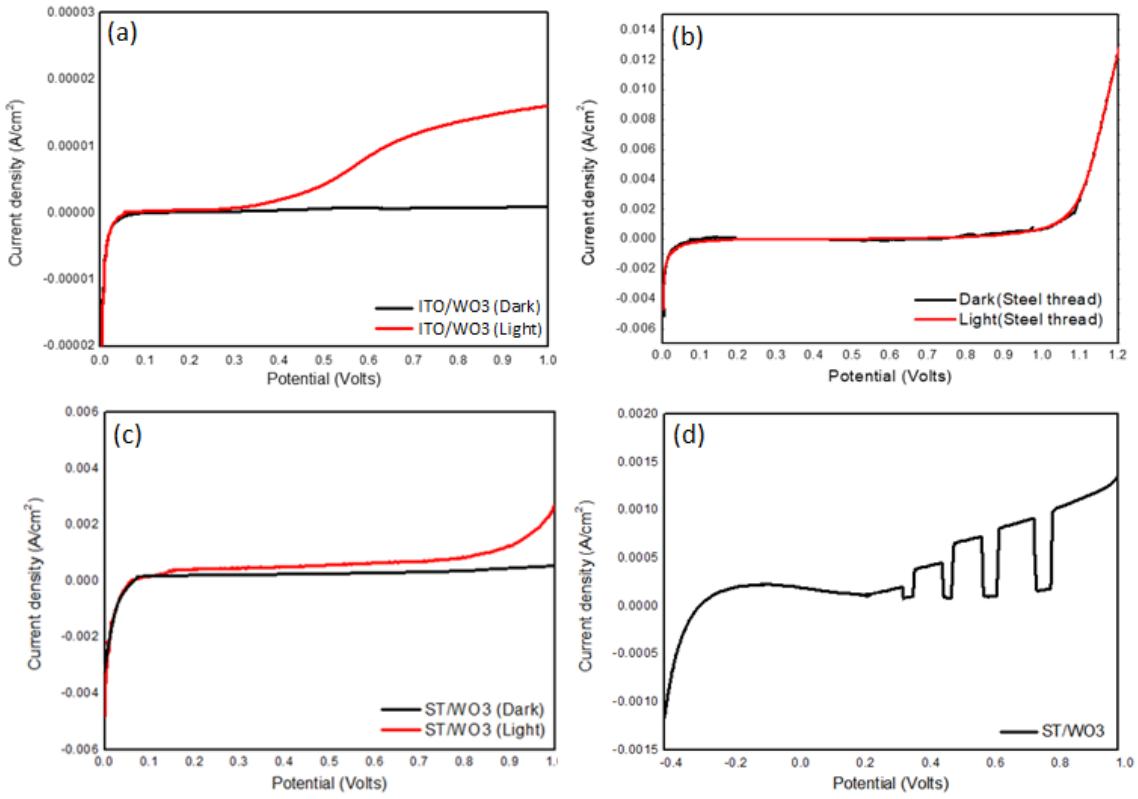

Figure 37. Comparison of linear sweep voltammograms for WO_3 films on various substrates in the dark and under illumination with 500 W Xe lamp (71 mW/cm^2). (a) ITO; (b) uncoated stainless steel thread; (c) stainless steel thread with WO_3 deposit, 10 mV/s sweep rate, and (d) chopped photo-response of WO_3 electrodeposited on stainless steel thread at 5 mV/s scan rate.

By varying conditions and substrates for electrodepositing WO_3, we have produced different thicknesses of the thin films. By using the relationship between the total charge passed during electrodeposition and the thickness of the deposited films, we can calculate the deposited film thickness by using the coulometric method. From Fig 38, we can integrate current over time, which is $Q = \int_0^t idt$, corresponding to the area under the curve. The equation for film thickness is:

$$D = Q \cdot M/n \cdot F \cdot A \cdot \rho$$

where M is the molecular weight of WO_3 (231.84 g/mol), n is the number of electrons transferred ($n = 2$), F is the Faraday constant (96485 A·sec/mol), and ρ is the density of WO_3 (7.16 g/cm^3).[61] By acquirng the data of Q, we have calculated thicknesses 10.7 and 17.3 μm for ITO/WO_3 and stainless steel thread/WO_3, respectively. Also, by comparison of the SEM images of deposited films in Fig. 26(a) and (d), we used Image J (Fiji software) to analyze the surface area of the films. Regarding each individual grain that is deposited, the average area we have analyzed was 150 and 1.02 μm^2 for for ITO/WO_3 and stainless steel thread/WO_3, respectively. The higher thickness of the film indicates there is more material that is deposited on the substrate and smaller specific area of the deposited films. A higher photocurrent density may be observed with larger exposed surface area with long carrier diffusion length and efficient charge transport and separation.

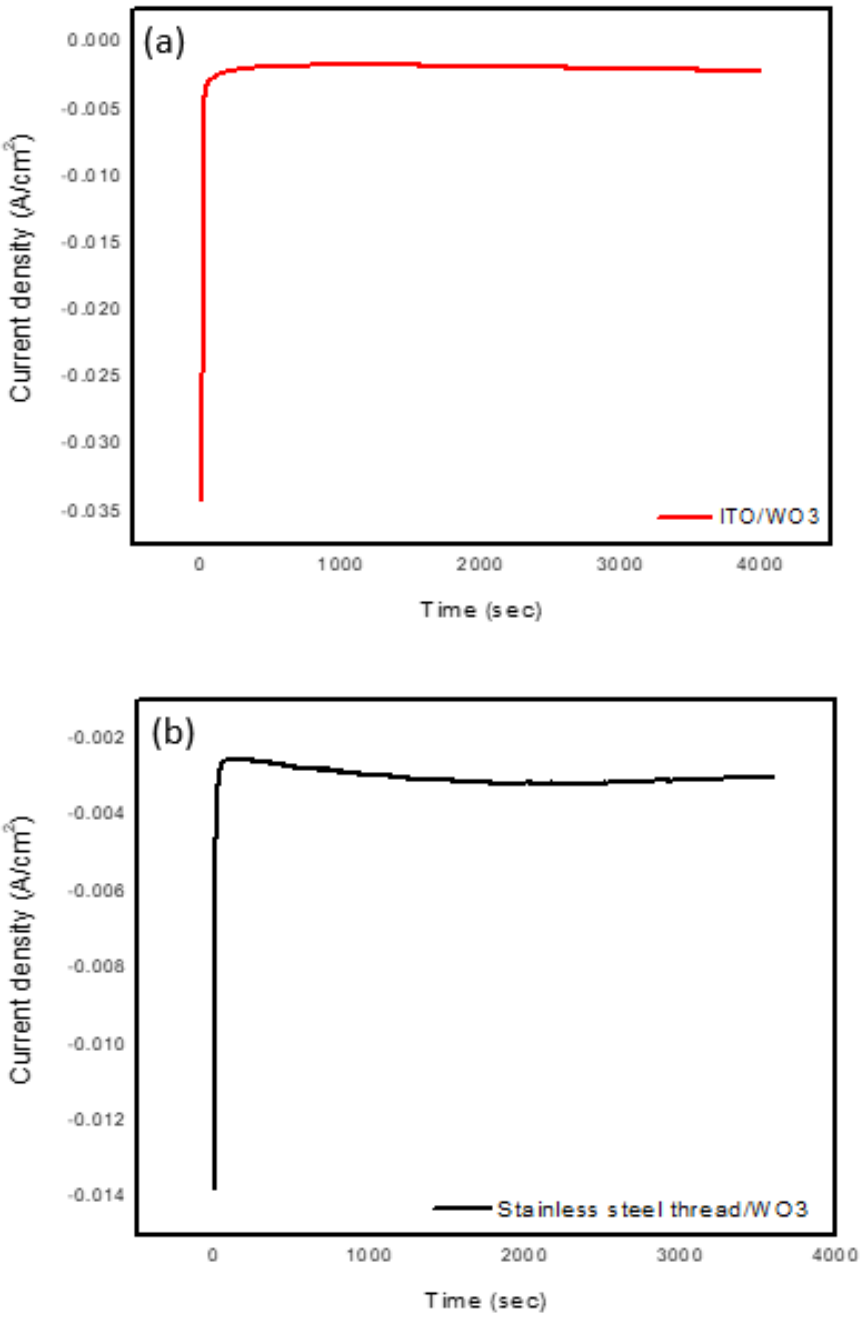

Figure 38. Current density vs time curve of (a) ITO and (b) stainless steel thread with potential -0.45 V.

3-6. Photovoltaic characterization

From Fig. 39 to Fig. 43 the comparison of I-V curves for fabricated liquid junction solar cells oriented as twisted format with illuminated intensity of 71 mW/cm^2 is shown. The corresponding values of open circuit voltage (V_{OC}), short circuit current (J_{SC}), fill factor (FF) and overall efficiency (η) are summarized in Table 3 to Table 7. The effect of natural dyes and organic pigments on the cell performance is also shown. Deciding on the redox couple in a liquid junction solar cell is crucial; at present we have used 0.1 M KI and 0.01 M I_2 with DI water (pH adjusted by 10% H_2SO_4) for the I^-/I_3^- redox couple. Further work was conducted by replacing the inorganic salts (0.1 M KI) with the organic salts tetraethylammonium iodide (TEAI), tetrapropylammonium iodide (TPAI), and tetrabutylammonium iodide (TBAI) in organic-based (acetonitrile) electrolyte. The effect of electrolyte composition on liquid junction solar cells based on WO_3 electrodeposited on a steel thread photoanode (control) is shown in Fig. 39. For the aqueous I^-/I_3^- system, V_{OC} = 78.74 mV, $J_{SC} = -1.17 \times 10^{-2}$ mA/cm^2, $FF = 19.26\%$ and $\eta = 0.06\%$. By replacing the electrolyte to acetonitrile, the values were enhanced to V_{OC} = 81.09 mV, $J_{SC} = -4.10 \times 10^{-2}$ mA/cm^2, $FF = 34.41\%$, and $\eta = 0.36\%$. Compared to water the potential window of acetonitrile is large (> 3.0 V) where no faradaic reaction takes involving the solvent as a reactant. The molecular weight increases as TEAI (257.16 g/mol) < TPAI (313.27 g/mol) < TBAI (369.38 g/mol) so that TBAI has the largest molecular size. The trend of the I-V curves showed that smaller molecular weight has greater ion mobility for the charge transfer and so the performance of the FF followed 22.08, 19.83, and 15.79% for TEAI, TPAI, and TBAI respectively.

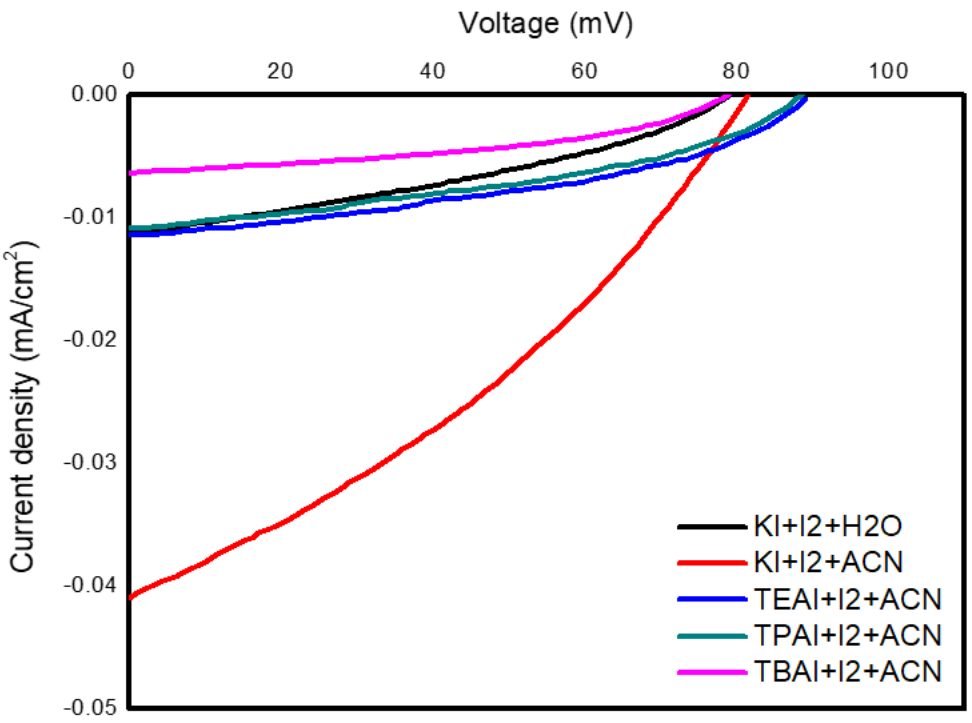

Figure 39. Comparison of current-voltage (I-V) characteristics of fabricated WO_3/stainless steel photoanode liquid junction solar cell.

Table 3. Performance of the fabricated liquid junction solar cell based on WO_3/stainless steel.

Sample	V_{OC} (mV)	J_{SC} (mA/cm^2)	V_{mp} (mV)	J_{mp} (mA/cm^2)	FF (%)	η (%)
KI+I_2+H_2O	78.74	-1.17×10^{-2}	18.33	-9.68×10^{-3}	19.26	0.06
KI+I_2+ACN	81.09	-4.10×10^{-2}	47.67	-2.4×10^{-2}	34.41	0.36
TEAI+I_2+ACN	89.30	-1.17×10^{-2}	20.09	-1.07×10^{-3}	22.08	0.07
TPAI+I_2+ACN	87.84	-1.09×10^{-2}	19.20	-9.89×10^{-3}	19.83	0.06
TBAI+I_2+ACN	77.87	-6.09×10^{-3}	11.87	-6.31×10^{-3}	15.79	0.02

The I-V results for natural dye-loaded solar cells are shown in Fig. 40 and 41. The dyes were applied to WO_3-electrodeposited liquid junction cells and improved the solar conversion efficiency. The natural dyes contain high concentrations of anthocyanins, which have higher visible light absorptivities compared to WO_3. Compared to the WO_3 photoanode, where V_{OC} = 78.74 mV, $J_{SC} = -1.17 \times 10^{-2}$ mA/cm^2, $FF = 19.26\%$ and $\eta = 0.06\%$, the natural dye-loaded cells using blackberry (cyanidin) dye had its performance values enhanced to V_{OC} = 86.36 mV, $J_{SC} = -0.103$ mA/cm^2, $FF = 31.34\%$ and $\eta = 0.87\%$ based on H_2O electrolyte. Replacing the solvent with acetonitrile, the performance values of the cell were again improved to V_{OC} = 88.73 mV, $J_{SC} = -0.136$ mA/cm^2, $FF = 49.25\%$ and $\eta = 1.86\%$. The molecular size effect for TEAI, TPAI, and TBAI showed same trend for the FF as in the aqueous system with 41.71, 30.65 and 24.58% respectively. The anthocyanin dyes prepared from raspberries gave V_{OC} = 77.72 mV, $J_{SC} = -6.92 \times 10^{-2}$ mA/cm^2, $FF = 31.96\%$ and $\eta = 0.54\%$ based on H_2O electrolyte. Preparing the electrolyte with acetonitrile, the performance of the cell was enhanced to V_{OC} = 81.17 mV, $J_{SC} = -60.138$ mA/cm^2, $FF = 45.88\%$ and $\eta = 1.61\%$. For both sources of the natural dyes, the PV cell performance values were enhanced relative to those cells without dye loading onto the WO_3 films. Both natural dyes contain the cyanidin molecular species. However, there is a difference between side groups, in that blackberry dyes contain a 3-glucoside unit, which has a slight effect in shifting the solar energy absorption with slightly higher photoconversion efficiency.[62]

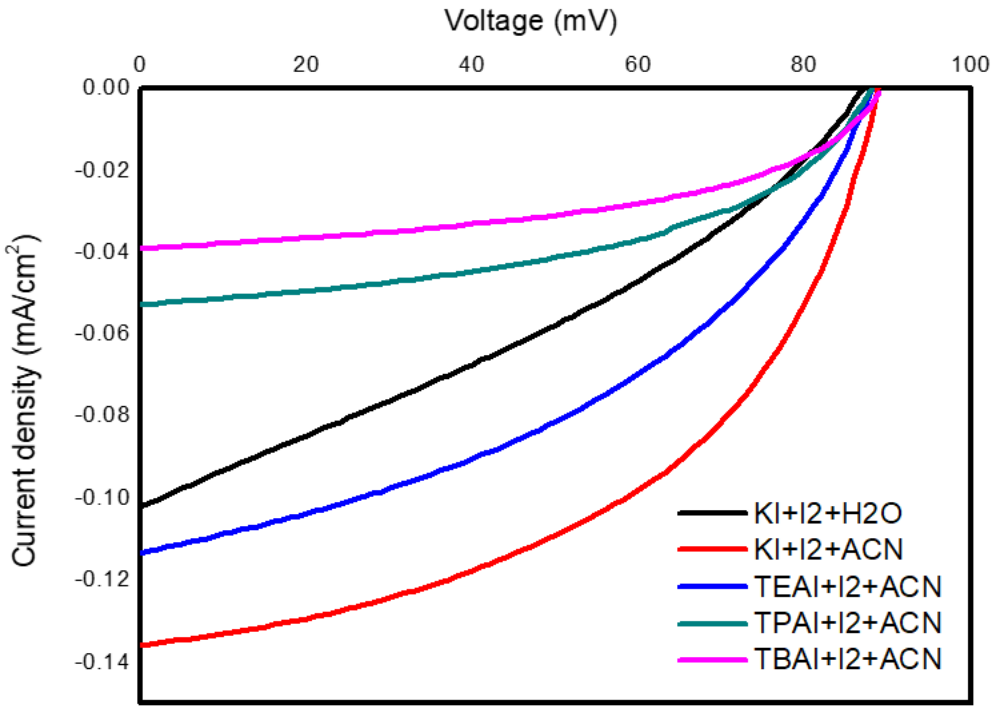

Figure 40. Comparison of current-voltage (I-V) characteristics of fabricated blackberry anthocyanin/WO_3/stainless steel photoanode liquid junction solar cell.

Table 4. Performance of the fabricated liquid junction solar cell based on blackberry anthocyanin/ WO_3/stainless steel.

Sample	V_{OC} (mV)	J_{SC} (mA/cm^2)	V_{mp} (mV)	J_{mp} (mA/cm^2)	FF (%)	η (%)
KI+I_2+H_2O	86.36	-0.103	42.97	-6.49×10^{-2}	31.34	0.87
KI+I_2+ACN	88.73	-0.136	62.62	-9.49×10^{-2}	49.25	1.86
TEAI+I_2+ACN	87.55	-0.113	52.35	-7.88×10^{-2}	41.71	1.29
TPAI+I_2+ACN	87.24	-5.30×10^{-2}	30.35	-4.67×10^{-2}	30.65	0.44
TBAI+I_2+ACN	88.73	-3.92×10^{-2}	23.62	-3.62×10^{-2}	24.58	0.27

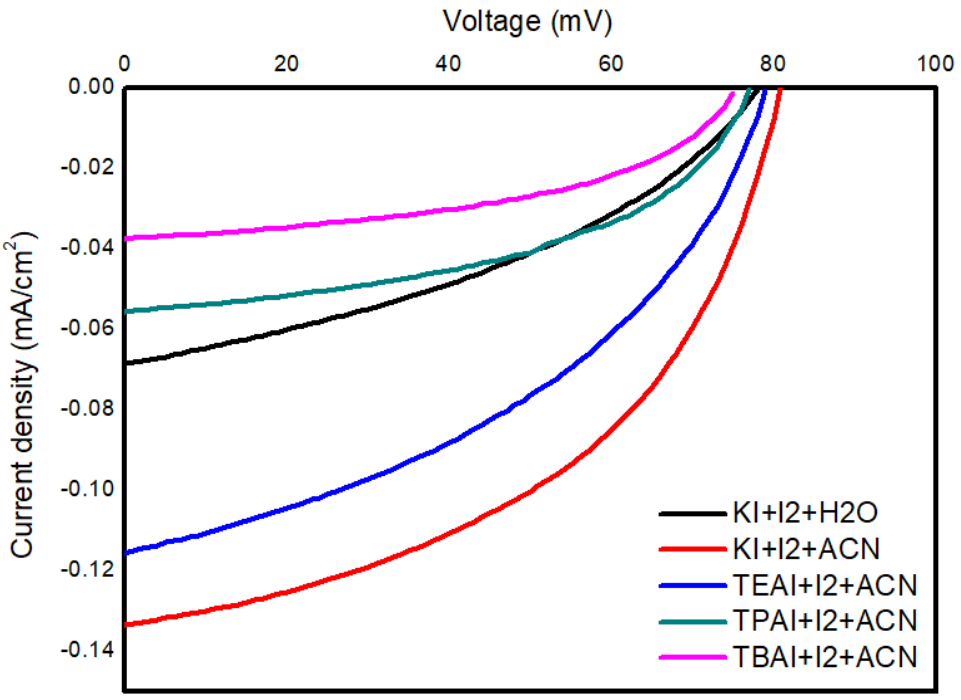

Figure 41. Comparison of current-voltage (I-V) characteristics of fabricated raspberry anthocyanin/ WO_3/stainless steel thread photoanode liquid junction solar cell.

Table 5. Performance of the fabricated liquid junction solar cell based on raspberry anthocyanin/WO_3/ stainless steel.

Sample	V_{OC} (mV)	J_{SC} (mA/cm^2)	V_{mp} (mV)	J_{mp} (mA/cm^2)	FF (%)	η (%)
KI+I_2+H_2O	77.72	-6.92×10^{-2}	32.07	-5.36×10^{-2}	31.96	0.54
KI+I_2+ACN	81.17	-0.138	55.56	-9.25×10^{-2}	45.88	1.61
TEAI+I_2+ACN	79.06	-0.116	47.91	-7.99×10^{-2}	41.74	1.19
TPAI+I_2+ACN	76.68	-5.66×10^{-2}	29.43	-4.88×10^{-2}	33.09	0.45
TBAI+I_2+ACN	74.82	-3.86×10^{-2}	20.73	-3.56×10^{-2}	25.55	0.23

Instead of natural dye molecules, many synthetic organic dyes have been studied for DSSCs. Organic dyes tend to have higher molar absorptivity coefficients than inorganic salt-based dyes, so they have more efficient light harvesting capabilities over the solar spectral region.[63] In this research we used a diketopyrrolopyrrole (DPP), specifically 3,6-bis(4-chlorophenyl)-DPP (Pigment Red 254) and 4,4'-diamino-1,1'-bianthraquinone (Pigment Red 177) for comparison. Similar to the natural dyes, the photovoltaic performance of the synthetic organics follow donor-acceptor π-conjugated bridges (D-π-A structures), which possess both electron-donating (D) and electron-accepting (A) groups linked by π-conjugated bridges, displaying broad spectral absorption.[64] The prepared synthetic organic dye-loaded liquid junction cells are shown in Fig. 42 and 43, and the detailed photovoltaic parameters are summarized in Table 6 and 7. By loading DPP onto an electrodeposited WO_3 photoanode, V_{OC} = 118.82 mV, $J_{SC} = -5.52 \times 10^{-2}$ mA/cm^2, $FF = 20.85\%$ and $\eta = 0.43\%$ based on H_2O electrolyte. Replacing the solvent with acetonitrile, the performance of the cell was enhanced to V_{OC} = 115.97 mV, $J_{SC} = -8.07 \times 10^{-2}$ mA/cm^2, $FF = 40.95\%$ and $\eta = 1.19$. By using Red 177 for the photosensitizer, V_{OC} = 138.18 mV, $J_{SC} = -4.44 \times 10^{-2}$ mA/cm^2, $FF = 35.12\%$ and $\eta = 0.68\%$ based on H_2O electrolyte. Replacing the solvent to acetonitrile, the performance of the cell was enhanced to V_{OC} = 137.73 mV, $J_{SC} = -4.73 \times 10^{-2}$ mA/cm^2, $FF = 46.53\%$ and $\eta = 0.95\%$. Compared to the natural dye loaded cells, the DPP and Red 177 cells showed higher open circuit voltages, which can be attributed to an upward shift of the conduction band edge. A similar trend was found in Dualeh et al,[65] who studied how applying donor groups of organic D- π-A dyes onto TiO_2 influenced V_{OC}. As seen in previous cases, using TEAI, TPAI, and TBAI for the I^-/I_3^-

redox couple gave a FF trend of 35.49, 31.15 and 13.36% for DPP and 38.31, 20.22 and 14.77% for Red 177 dyes, respectively.

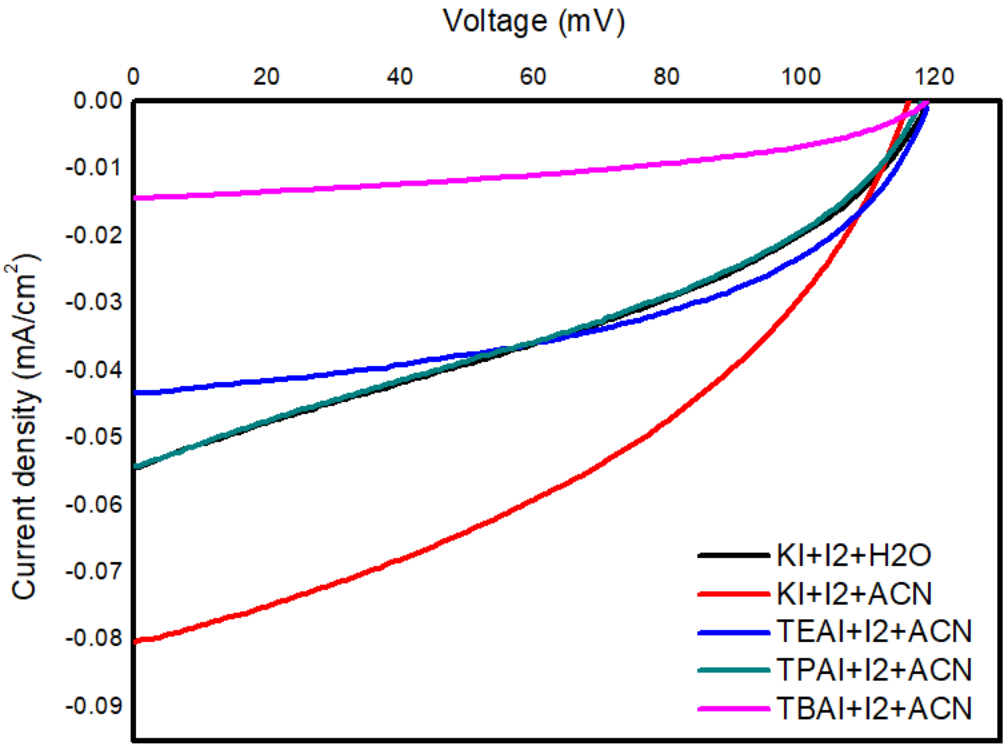

Figure 42. Comparison of the current-voltage (I-V) characteristics of fabricated bis(4-chlorophenyl)DPP/WO_3/ stainless steel photoanode liquid junction solar cell.

Table 6. Performance of the fabricated liquid junction solar cell based on bis(4-chlorophenyl)DPP/WO_3/ stainless steel.

Sample	V_{OC} (mV)	J_{SC} (mA/cm^2)	V_{mp} (mV)	J_{mp} (mA/cm^2)	FF (%)	η (%)
KI+I_2+H_2O	118.42	-5.52×10^{-2}	51.21	-3.89×10^{-2}	20.85	0.43
KI+I_2+ACN	115.97	-8.07×10^{-2}	70.57	-5.37×10^{-2}	40.85	1.19
TEAI+I_2+ACN	119.12	-4.40×10^{-2}	49.09	-3.79×10^{-2}	35.49	0.58
TPAI+I_2+ACN	117.36	-5.41×10^{-2}	50.84	-3.89×10^{-2}	31.15	0.62
TBAI+I_2+ACN	118.06	-1.49×10^{-2}	17.42	-1.35×10^{-2}	13.36	0.07

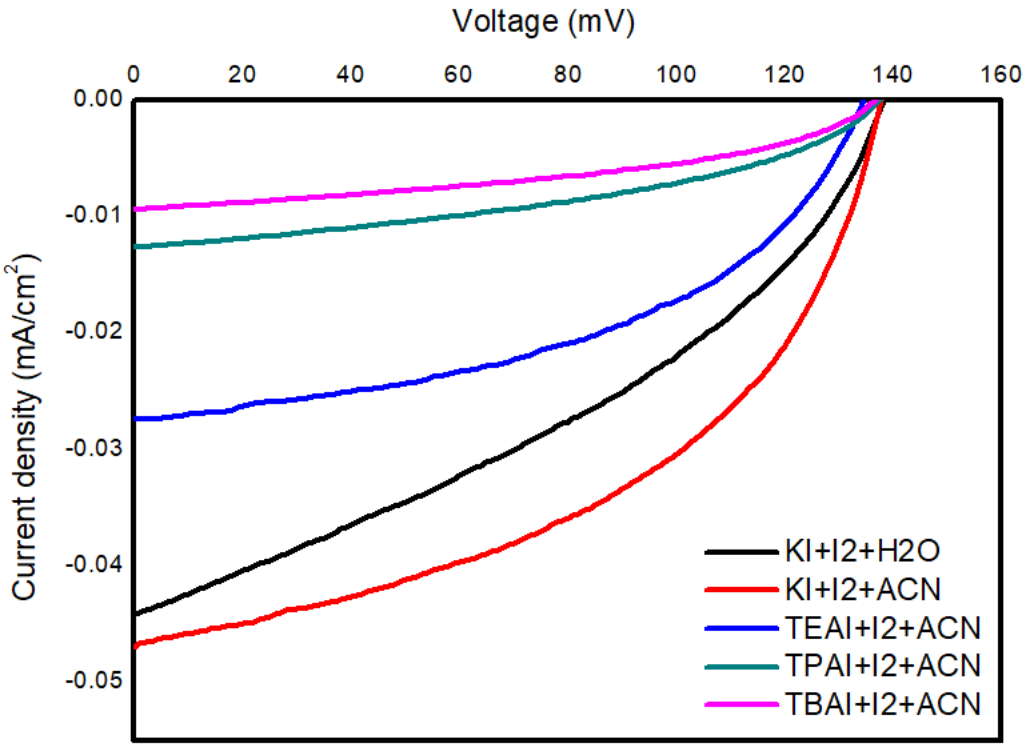

Figure 43. Comparison of current-voltage (I-V) characteristics of fabricated RED177/WO_3/stainless steel photoanode liquid junction solar cell.

Table 7. Performance of the fabricated liquid junction solar cell based on Red177/WO_3/ stainless steel.

Sample	V_{OC} (mV)	J_{SC} (mA/cm^2)	V_{mp} (mV)	J_{mp} (mA/cm^2)	FF (%)	η (%)
KI+I_2+H_2O	138.18	-4.44×10^{-2}	75.34	-2.86×10^{-2}	35.12	0.68
KI+I_2+ACN	137.73	-4.73×10^{-2}	89.41	-3.39×10^{-2}	46.53	0.95
TEAI+I_2+ACN	134.91	-2.74×10^{-2}	60.78	-2.33×10^{-2}	38.31	0.44
TPAI+I_2+ACN	133.49	-1.26×10^{-2}	29.32	-1.16×10^{-2}	20.22	0.11
TBAI+I_2+ACN	136.32	-9.69×10^{-3}	22.30	-8.75×10^{-3}	14.77	0.06

To further improve the J_{SC} of the constructed cells, a small organic electron donor, triethylamine (TEA), was added to the iodide/triiodide electrolyte of the liquid junction solar cells. Fig. 44 shows the comparison of photovoltaic performance of prepared cells with/without adding 0.1 M of TEA into the I^-/I_3^- redox electrolyte. By adding the organic electron donor, as from Fig. 44(a), V_{OC} and J_{SC} increased from 89.30 to 102.6 mV and from -4.10×10^{-2} to -4.45×10^{-2} mA/cm^2 for the electrodeposited WO_3 photoanode, respectively. The $FF = 36.8\%$ and $\eta = 0.53\%$ was calculated after the addition of TEA. From Fig. 44(b), after loading the natural dyes onto the WO_3 photoanode, adding TEA into the redox electrolyte enhanced V_{OC} from 88.73 to 98.55 mV and J_{SC} from -0.136 to -0.171 mA/cm^2. The $FF = 46.3\%$ and $\eta = 2.44\%$ was calculated after the addition of TEA.

The enhancement of the performance of the cells can be explained by the effect of TEA on the charge transfer reactions of the dye, the iodide/triiodide redox couple and the WO_3 semiconductor electrode.[66] From Fig. 45, the addition of an amine commonly has a positive redox potential around 1.0 V vs NHE. Therefore, it can give an electron to a photogenerated hole in the WO_3, and then having been oxidized, can in turn be reduced by iodide ion. The idea is that the redox catalyst amine can react faster with WO_3 and iodide ion. When using one of the anthocyanin natural dyes as a sensitizer, an improved solar performance was also found, which could be attributed to a rapid dye regeneration reaction when TEA is added.

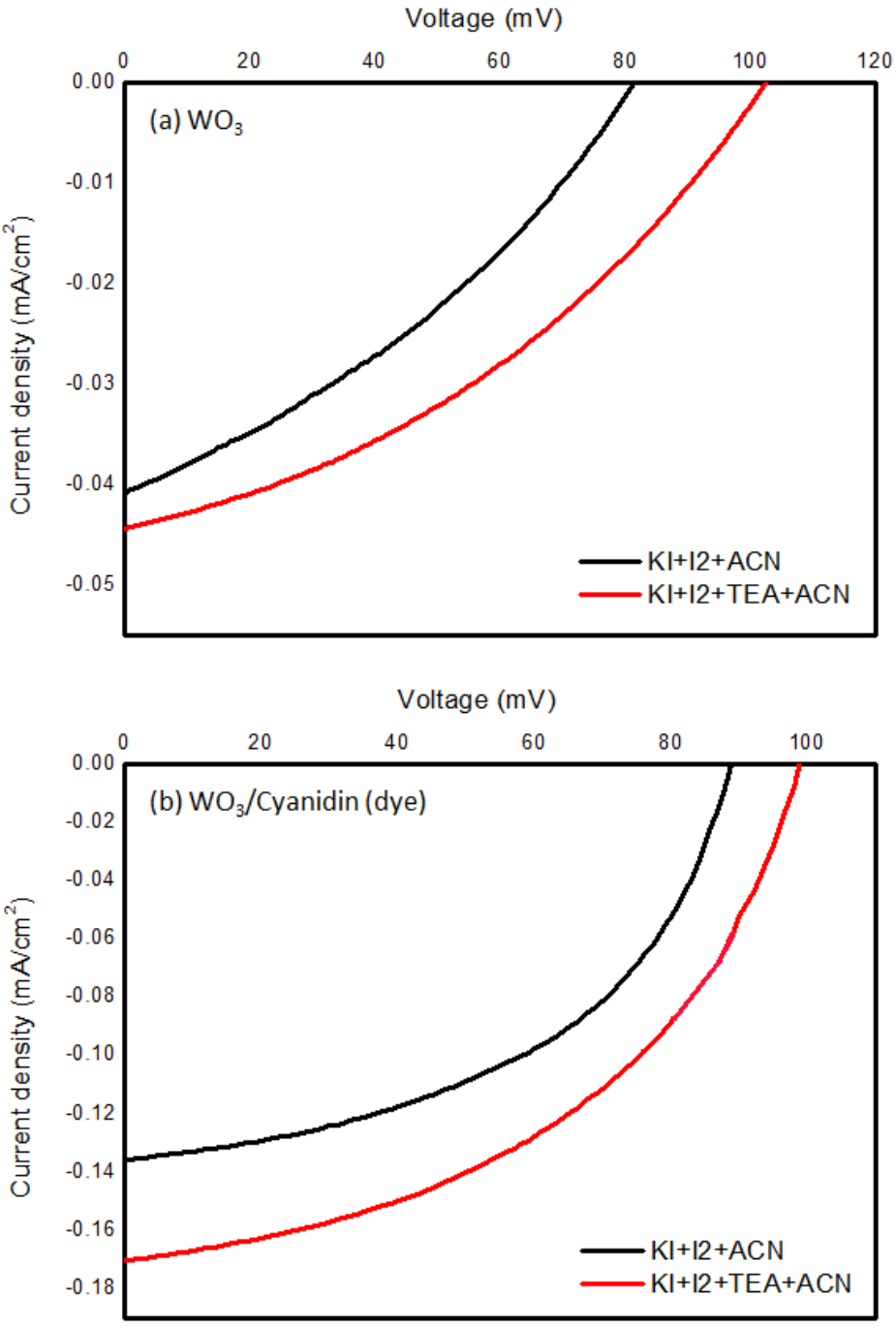

Figure 44. Comparison of current-voltage (I-V) characteristics of fabricated liquid junction cell with adding 0.1 M of triethylamine (TEA) based on acetonitrile (ACN) (a) WO_3 photoanode and (b) cyanidin /WO_3/ loaded photoanode.

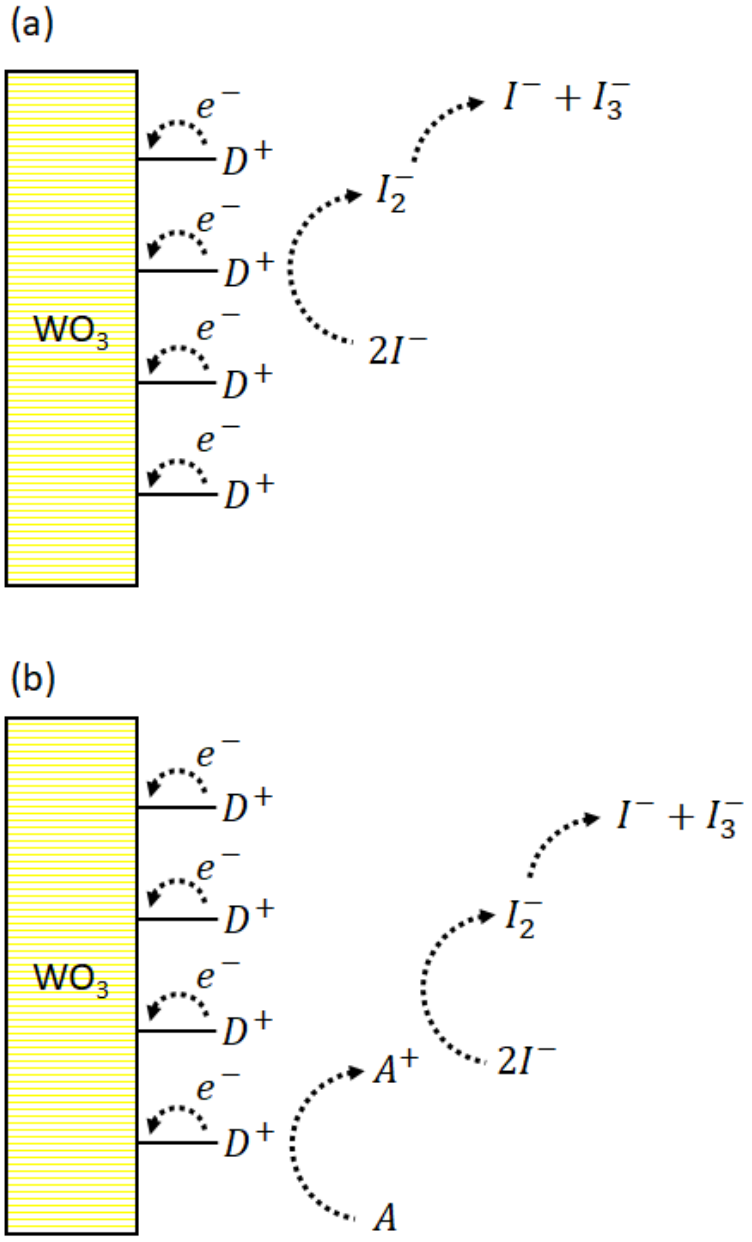

Figure 45. Comparison of schematic diagram for the charge transfer reaction of (a) iodide/triiodide electrolyte and (b) triethylamine added for rapid dye regeneration.

3-7. Comparison of geometric orientation of constructed cells

To compare the geometric configuration, we employed different shape of stainless steel 316L wire as a substrate for WO_3 electrodeposition. Fig. 46 shows the surface morphologies of the electrodeposited WO_3 before/after deposition onto square shape stainless steel 316L wire. The substrate edge-to-edge width was 0.51 mm, the prepared square photoanode wire twisted around the Pt-deposited and PMMA latex covered counter electrode can be seen in Fig. 46(d). From the difference in shape of the photoanode, we wanted to compare the illumination area and assess the photovoltaic performance of the liquid junction solar cells. The performance of the prepared liquid junction solar cells with difference shape comparison can be seen on Fig. 47. By using a square shape wire for the substrate, the V_{OC} = 81.09 mV, $J_{SC} = -4.10 \times 10^{-2}$mA/cm^2, $FF = 34.41\%$ was measured. Using a circular shape wire (or thread) for the substrate, enhanced parameters V_{OC} = 81.09 mV, $J_{SC} = -4.10 \times 10^{-2}$ mA/cm^2, $FF = 34.41\%$ were obtained. The use of circular thread improved the light absorption, from which FF increased 2.8%.

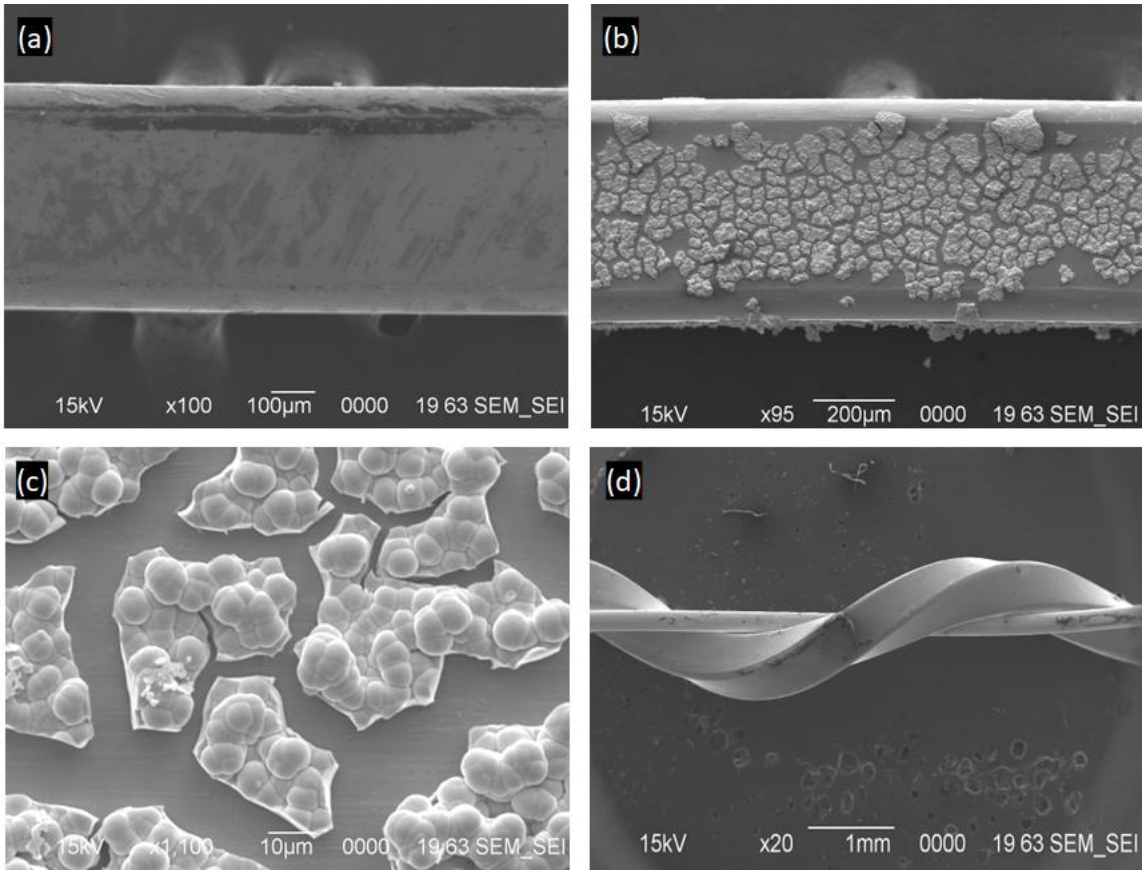

Figure 46. SEM images of a fabricated PV cell with square shape 316L stainless steel wire substrate. (a) uncoated square shape stainless steel wire, (b) WO_3 electrodeposited on the square stainless steel wire, (c) 1100 X magnification of the WO_3 coated, and (d) constructed square wire-shaped PV cell.

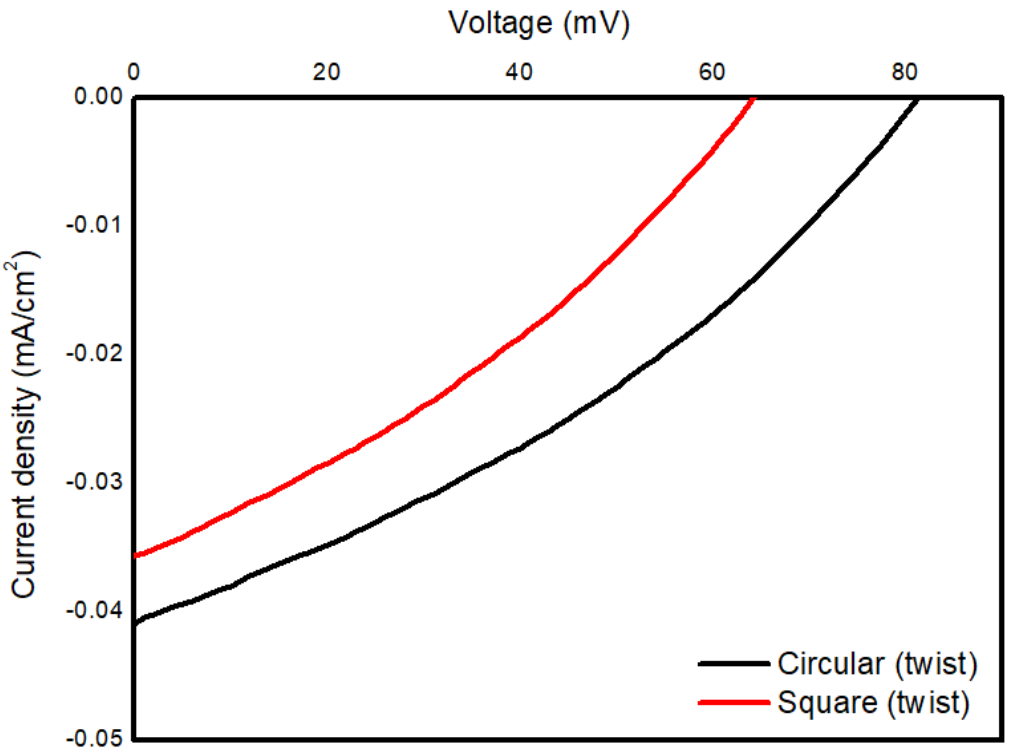

Figure 47. Comparison of current-voltage (I-V) characteristics of fabricated liquid junction solar cells based on WO_3 electrodeposited onto square-and circular-shaped stainless steel 316L as photoanode (twist orientation).

Table 8. Performance of the fabricated liquid junction solar cells based on square and circular shape WO_3 electrodeposited photoanode.

Sample	V_{OC} (mV)	J_{SC} (mA/cm^2)	V_{mp} (mV)	J_{mp} (mA/cm^2)	FF (%)	η (%)
Circular	81.09	-4.10×10^{-2}	47.67	-2.40×10^{-2}	34.41	0.36
Square	64.07	-3.56×10^{-2}	38.56	-1.98×10^{-2}	33.47	0.24

Also, it was attempted to design liquid junction cells with a different orientation. Fig. 48 shows a schematic diagram for the design of parallel-oriented wire-shaped liquid junction solar cells. Another attribute of the original design involved coating the counter electrode, with an insulating, protective layer of PMMA latex in order to prevent shorting between the electrodes. To assess the effectiveness of the PMMA latex I-V characteristics were obtained for cells with/without the protective coating. Fig. 49 compares the I-V curves of the liquid junction cells with different orientation and with/without PMMA latex coating. The original design (twisted version) with PMMA latex gave V_{OC} = 81.09 mV, $J_{SC} = -4.10 \times 10^{-2}$ mA/cm^2, and $F = 34.41\%$. For the twist version without the PMMA latex coating, the cell performance was measured to be V_{OC} = 74.36 mV, $J_{SC} = -3.54 \times 10^{-2}$ mA/cm^2, and $FF = 32.47\%$, indicating that the PMMA latex coating prevented recombination of charge via shorting. The performance of the parallel electrode orientation of the cell was measured as V_{OC} = 42.20 mV, $J_{SC} = -2.06 \times 10^{-2}$ mA/cm^2, and $FF = 29.05\%$ with the PMMA latex-coated counter electrode. Without the PMMA latex coating, the cell performance showed measured V_{OC} = 41.33 mV, $J_{SC} = -1.93 \times 10^{-2}$ mA/cm^2, and $FF = 28.91\%$. For of the parallel version with/without the PMMA latex, the performance appeared in the similar range, implying that the recombination of charge was avoided due to the physical separation of the two electrodes. Fig. 50 compares the adsorption of liquid electrolyte onto two electrodes with PMMA latex coating. The nature of PMMA is hydrophobic.[67] However, a lowering of pH can protonate surface oxygen groups, change the surface energy and render the PMMA latex into hydrophilicity. The adsorption of liquid electrolyte onto both electrodes was enhanced with time.

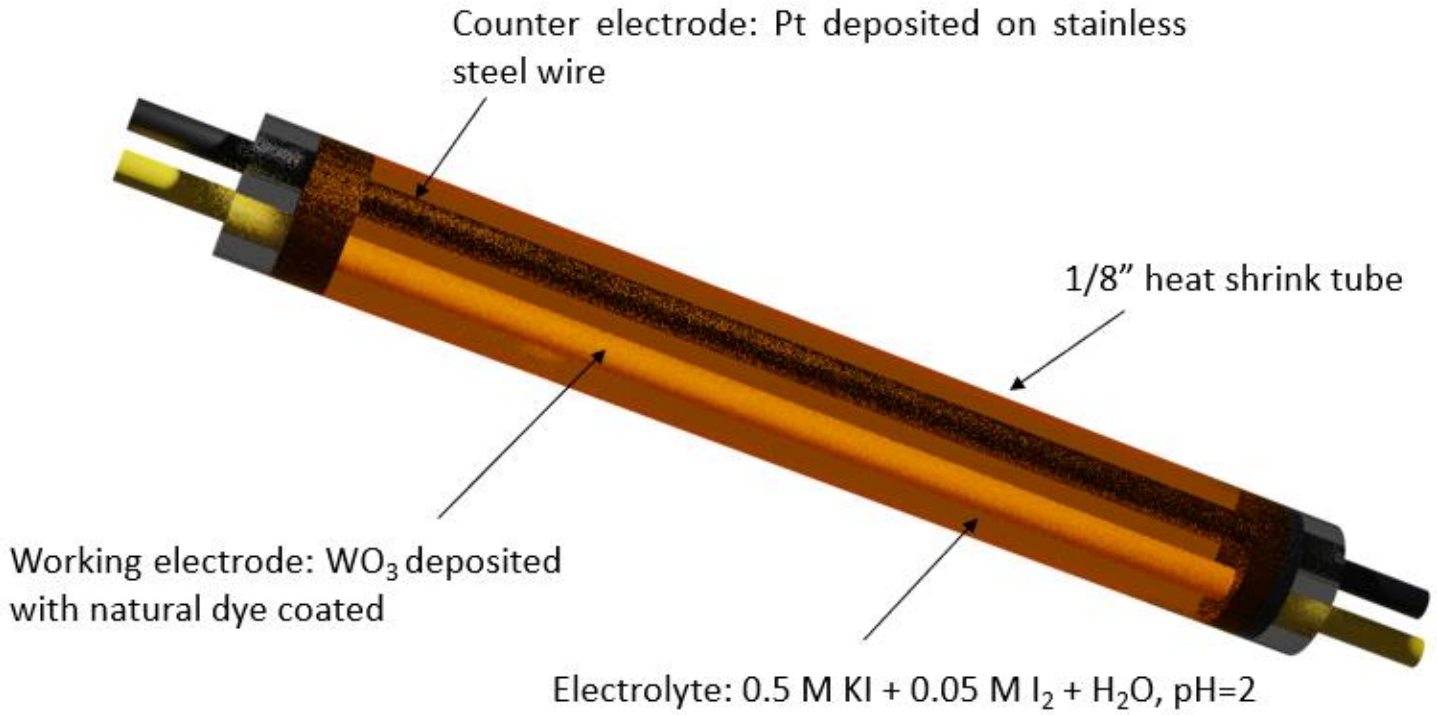

Figure 48. Schematic diagram of liquid junction solar cell with parallel orientation with using stainless steel thread as a substrate for WO_3 electrodeposition.

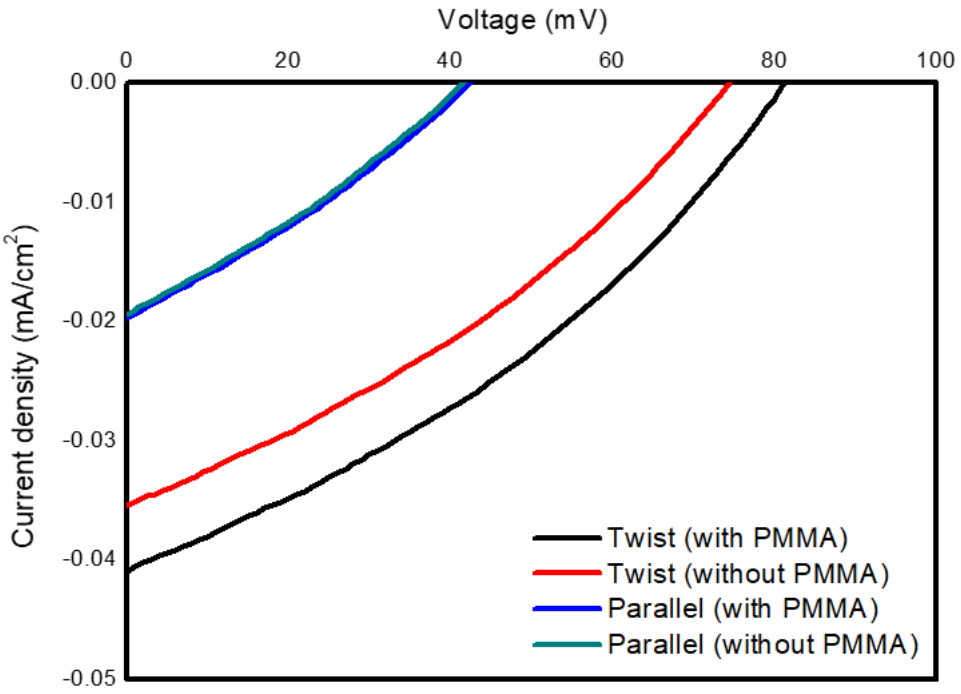

Figure 49. Comparison of current-voltage (I-V) characteristics of fabricated liquid junction solar cells with WO_3 electrodeposited on stainless steel thread in twist and parallel orientation with/without PMMA latex coated; Pt-deposited counter electrode.

Table 9. Performance of the fabricated liquid junction solar cells based on different orientation.

Sample	V_{OC} (mV)	J_{SC} (mA/cm^2)	V_{mp} (mV)	J_{mp} (mA/cm^2)	FF (%)	η (%)
Twist with PMMA	81.09	-4.10×10^{-2}	47.67	-2.40×10^{-2}	34.41	0.36
Twist Without PMMA	74.36	-3.54×10^{-2}	41.09	-2.08×10^{-2}	32.47	0.27
Parallel With PMMA	42.20	-2.06×10^{-2}	22.75	-1.11×10^{-2}	29.05	0.08
Parallel Without PMMA	41.33	-1.93×10^{-2}	21.55	-1.07×10^{-2}	28.91	0.07

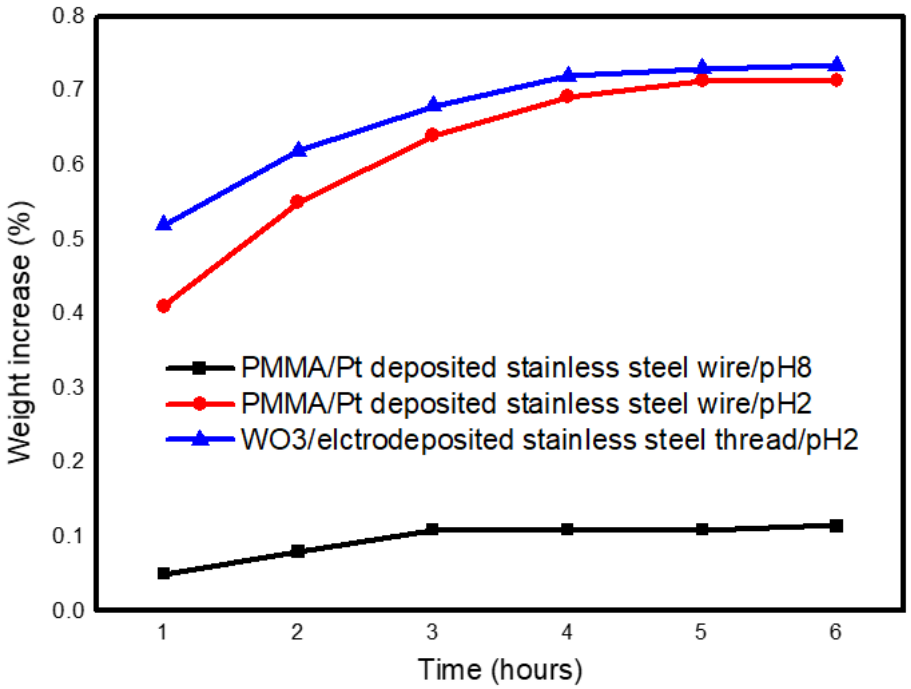

Figure 50. Weight increase (%)/Water uptake comparison after electrode immersion in $KI+I_2+H_2O$; pH determined by 10% H_2SO_4 ; Pt-deposited stainless steel wire coated with PMMA latex and WO_3-electrodeposited stainless steel thread.

3-8. Long-term stability test

Establishing long-term stability and efficiency is an important step towards textile DSSCs. The present work has identified natural dye-loaded (blackberry anthocyanins), twisted photoanode WO_3 photoelectrodes as the best performers, with acetonitrile as electrolyte solvent. To perform a long-term stability test, the PV cell described above was exposed to daily sunlight for 5 weeks. From Fig. 51 and Table 10, performance data from each week of for the wire-shaped, dye-sensitized solar cell was recorded. From the I-V curves of the sample over 5 weeks, a downward trend in photoconversion efficiency from an initial value of 1.86% (week 1) to 0.52% on week 5 was observed. Possible degradation of the dye and redox electrolyte can affect the stability of the cell. Another reason could be due to the I-V measurement itself, which may irreversibly alter the dye/semiconductor interface. Cell lifetime measurements are tedious and expensive, but to prove long-term stability, accurate and reproducible measurements will be essential in future work.

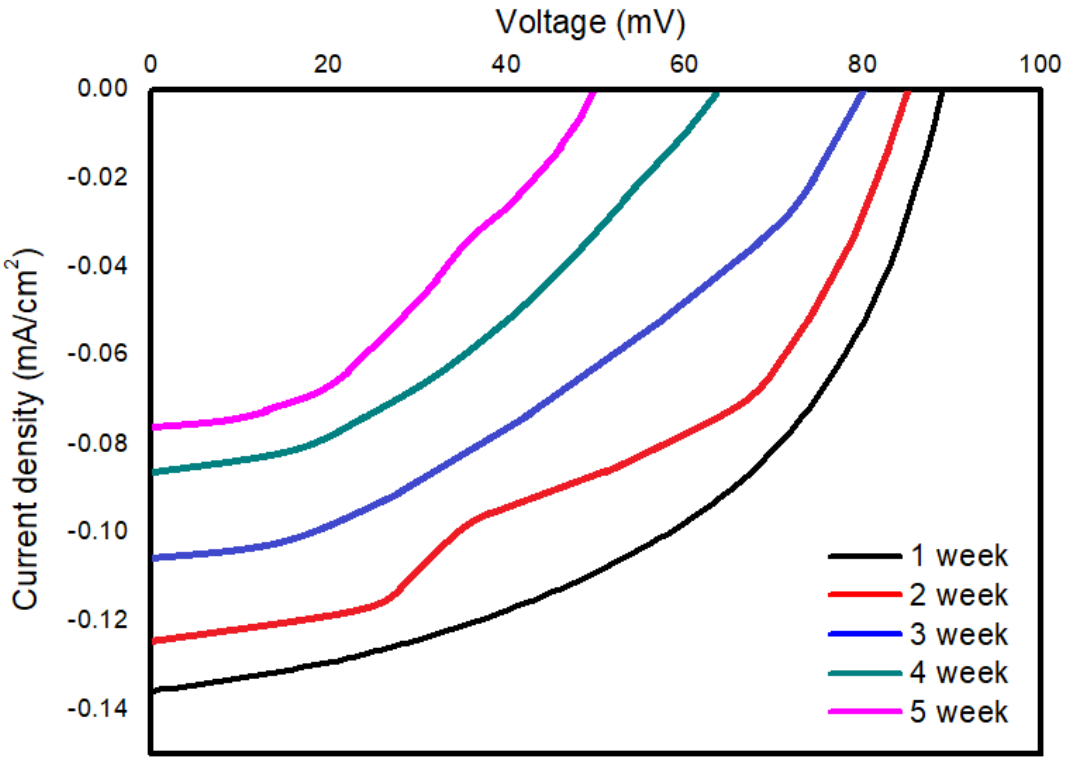

Figure 51. Long-term stability test of blackberry anthocyanin/WO_3/stainless steel thread liquid junction solar cell with 0.1 M KI + 0.01 M I_2 + acetonitrile electrolyte.

Table 10. Long-term performance of the fabricated liquid junction solar cell based on Blackberry/WO_3/stainless steel.

Sample	V_{OC} (mV)	J_{SC} (mA/cm^2)	V_{mp} (mV)	J_{mp} (mA/cm^2)	FF (%)	η (%)
1	88.73	-0.136	62.62	-9.49×10^{-2}	49.25	1.86
2	83.26	-0.127	57.35	-8.31×10^{-2}	41.46	1.37
3	80.02	-0.108	47.23	-7.03×10^{-2}	38.41	1.04
4	64.18	-8.34×10^{-2}	37.11	-5.65×10^{-2}	39.17	0.66
5	49.32	-7.85×10^{-2}	32.95	-5.02×10^{-2}	42.72	0.52

Chapter 4. Periodic Cracking of WO_3 films

4-1. Introduction

Brittle films supported by compliant substrates are important in many emerging technological applications as flexible electronics including flexible photovoltaic cells. However, the fracture behavior of stiff deposited films on compliant substrates can fracture into patterns of parallel cracks.[68,69] We have electrodeposited tungsten oxide (WO_3) films onto stainless steel microfiber. After annealing the films at 350 ℃ for 1 hour in air, it was seen that periodic cracks had occurred on the surface of the films, as shown on Fig. 26(d). As for case studies, there have been several on the cracking of stiff metal oxide coatings onto polymer substrates. The level of modulus mismatch between the two components for some of these applications can generate cracks when the metal film is supported by a flexible elastomer.[70] For instance, elastomer actuators deform in response to high electric field between thin metal electrodes on the surface of elastomeric dielectrics. During the deformation, failure of the surface layer is one of the limitations on the flexibility of the metal films. Formation of wrinkles can also occur on a thin film bonded to a compliant substrate.[71] When in-plain strain in an initially flat structure reaches a certain extent due to mechanical loading, thermal expansion mismatch, or chemical reactions, wrinkling partially diminishes the strain energy in the film layer and relieves the strain.[72] In both cases, the presence of stress in thin films and functional coatings constitutes a major concern in many technological applications, as excessive residual stress levels can dramatically affect performance, reliability, and durability of

material components and devices. From a more practical point of view, when brittle films are bonded to an elastic substrate with different modulus, a residual stress is presumed to exist in the film.[73] The focus of this section is the influence of the mismatch in modulus properties on patterns of crack formation in the film. Conventional laboratory XRD can be performed to characterize average residual stresses and stress gradients in thin films, coatings and near-surface regions. Residual stress measurement by XRD is unique in that macroscopic and microscopic stresses can be determined nondestructively. In XRD the strain in the crystal lattice is measured, and the residual stress producing the strain is calculated. As from Fig. 52, the shape and intensity of the XRD peaks can result from residual stress. For example, if there are no stresses in the conjoined phases, the peaks will appear at the exact 2θ. However, if tensile stresses are induced, the 2θ value will be shifted to the left on the baseline or if compression stresses are induced, the 2θ value will shift to the right, due to the increased/decreased d-spacing between two atoms.[74] By the following equation, the strain can be calculated as

$$\varepsilon = \frac{\varepsilon_i - \varepsilon_0}{\varepsilon_0} = \frac{d_i - d_0}{d_0}$$

where d_0 is the spacing of the same {hkl} planes in the absence of stress and d_i is the spacing after stress.[75] The residual stress is calculated quantitatively via

$$\sigma = -\frac{E}{v}\left(\frac{d_i - d_0}{d_0}\right)$$

Where, E and ν are Young's modulus and Poisson's ratio respectively.[76] Stress measurement by the XRD method is achieved by measurement of the change in d-spacing characteristically revealed as changes in diffraction peak position. In other words, the sample under study must be crystalline to give a sharp diffraction peak.

This method was employed to analyze the periodic cracking effect with residual stress measurements. WO_3 electrodeposited thin films onto stainless steel thread were annealed at different temperatures to analyze the fracture mechanics with scanning electron microscopy and X-ray diffraction.

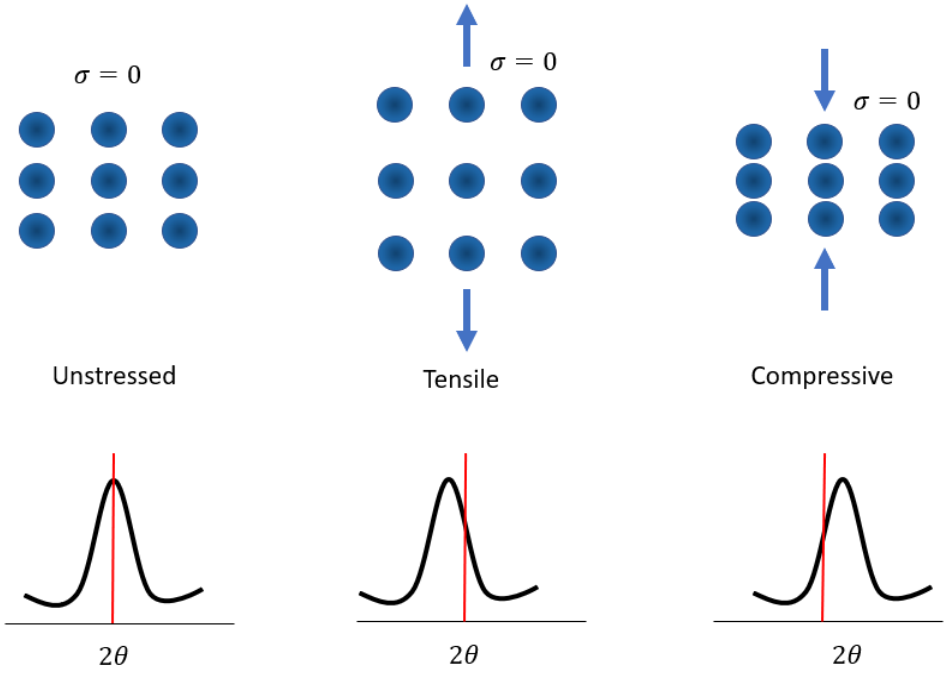

Figure 52. Stress and its effect on d-spacing and diffraction peak position on XRD.

4-2. Modeling periodic cracking

A schematic diagram of the geometric comparison of crack formation can be seen on Fig. 53. By using the geometric function, the mechanism of crack formation, in which the critical strain depends on the thickness of the film and the spacing between the arrays can be determined. The relationship can be expressed as

$$\frac{S_{ch}}{h} = f_2\left(\alpha, \beta, \frac{\Gamma_f}{\Gamma_s}, \frac{\varepsilon_0^2 \overline{E_f} h}{\Gamma_f}\right),$$

where the film thickness is h, Γ is the toughness and the subscripts f and s denote the film and substrate respectively.[77] The nondimensional Dundur's parameters for the modulus mismatch across the interface α and β are given by

$$\alpha = \frac{\overline{\overline{E_f}} - \overline{E_s}}{\overline{\overline{E_f}} + \overline{E_s}}$$

And

$$\beta = \frac{\overline{\overline{E_f}}(1 - \overline{\nu_s}) - \overline{E_s}\left(1 - \overline{\nu_f}\right)}{2\left(\overline{\overline{E_f}} + \overline{E_s}\right)} \quad ,$$

where $\bar{E} = E/(1 - \nu^2)$ and $\bar{\nu} = \nu/(1 - \nu)$ in plane strain, E is Young's modulus, and ν is Poisson's ratio.[78]

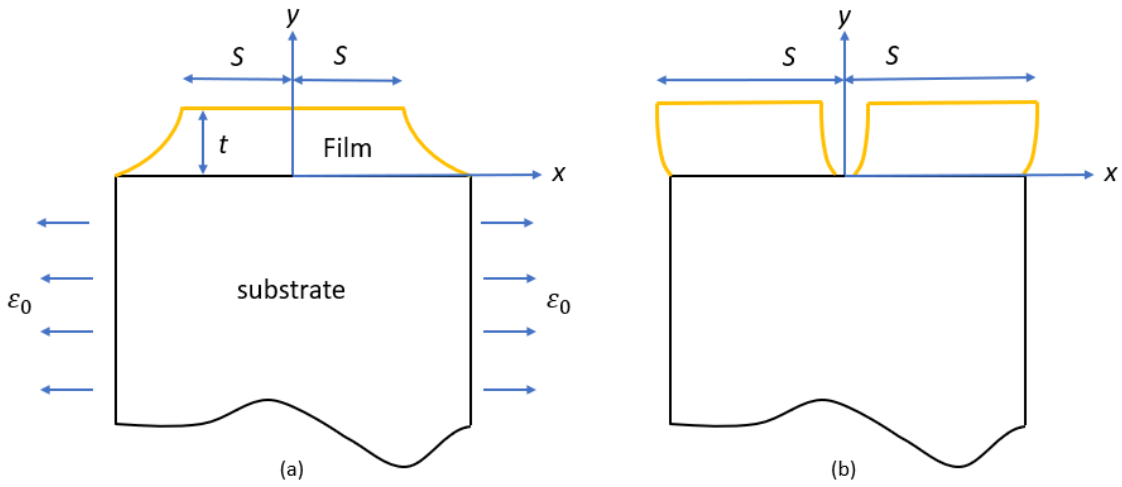

Figure 53. Schematic diagram of the process by which the energy changes associated with a crack channeling as (a) stress distribution along the mid plane and (b) introducing crack opening along the plane.

4-3. Characterization techniques

The surface morphology of the electrodeposited WO_3 film onto stainless steel microfiber was investigated using a scanning electron microscope (JEOL JIB-4500 multibeam system). The crystalline phase and strain calculation were determined by an X-ray diffractometer (Bruker, X8 PROSPECTOR).

4-4. Morphology study

The comparison of surface morphology of the electrodeposited WO_3 film onto stainless steel thread with different annealing temperatures was characterized by SEM. The SEM images in Fig. 54 show a smooth surface for stainless steel thread without any treatment. Depositing WO_3 films at different annealing temperatures can create different patterns of

cracks. Havingdeposited the WO_3 film at room temperature, a few cracks appearng after the drying process can be seen. After annealing at 50 and 150 ℃, the formation of cracks without periodicity were observed. After annealing at 350 ℃ for 1 h, the crack formation is periodic with uniform channeling. At 450 ℃, instead of periodic cracks, there are random shapes of cracks appearing. Thus from the SEM analysis, different cracking patterns were found and correlated to annealing temperature.

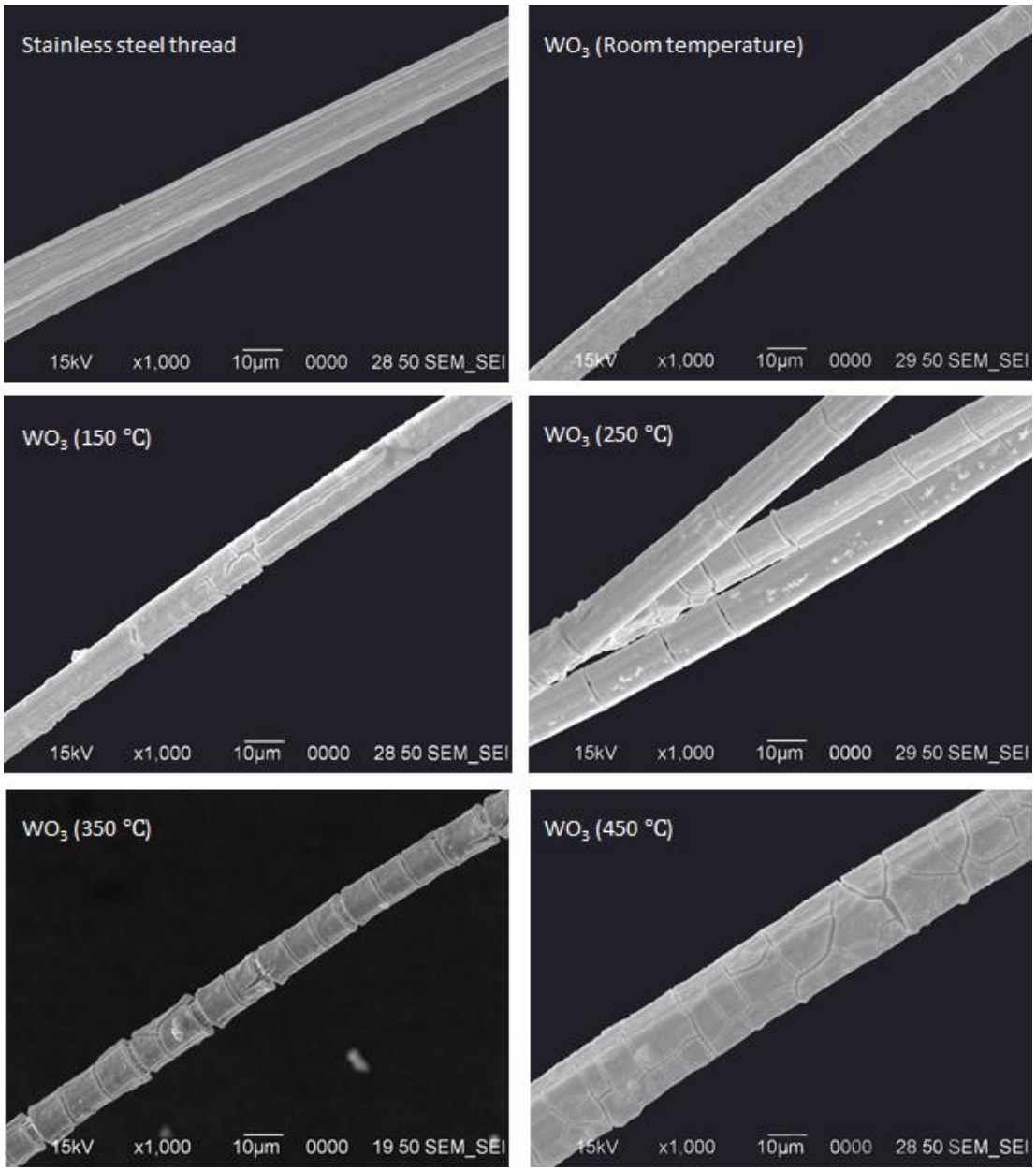

Figure 54. Comparison of SEM images of WO_3 electrodeposited films onto stainless steel thread with different annealing temperature.

4-5. Residual stress

The residual stress calculation was conducted based on the XRD results. From Table 11 and 12, the d-spacing parameters of stainless steel thread substrate and electrodeposited WO_3 film onto stainless steel thread, in which the tensile stress is presented in both cases after annealing at different temperatures. After using the strain equation and inserting the values from the reference into the equation,[79] the calculated residual stress is shown in Fig. 55. After annealing the uncoated stainless steel thread at different temperatures for 1 h, the residual stress was found to increase at higher temperatures. The maximum residual stress was calculated for annealing at 450 ℃ to be 3.89 GPa. The residual stresses of the WO_3 thin films exhibited a residual stress decrease from 2.13 to 2.05 GPa as the substrate temperature increased from 350 to 450 ℃. The residual stress is the sum of the intrinsic stress, thermal stress, and the external stress. The intrinsic stress is due to the deposition defects and lattice mismatch between the film and the substrate. The thermal stress is caused by the thermal mismatch between the thin film and substrate, and the external stress denotes the stress resulting external mechanical load.[80] In our observation, the residual stress decrease is due to the different rates of thermal mismatch release at different temperatures. By comparison between the annealing temperature at 350 and 450 ℃ of substrate and WO_3 thin film, the residual stress difference at 450 ℃ was larger compared that at 350 ℃, which can cause different shapes of cracks in the films.

Table 11. Stainless steel thread after annealed at different temperatures.

Temperature	2θ	Crystal structure	hkl	d-spacing	intensity
RT	44.696 °	Cubic	$\bar{1}\bar{1}0$	2.025 Å	624
150 ℃	44.648 °	Cubic	$\bar{1}\bar{1}0$	2.027 Å	503
250 ℃	44.553 °	Cubic	$\bar{1}\bar{1}0$	2.029 Å	139
350 ℃	44.524 °	Cubic	$\bar{1}\bar{1}0$	2.032 Å	135
450 ℃	44.491 °	cubic	$\bar{1}\bar{1}0$	2.036 Å	126

Table 12. WO_3 electrodeposited film annealed at different temperatures.

Temperature	2θ	Crystal structure	hkl	d-spacing
350 ℃	23.11° → 22.32°	Monoclinic	$00\bar{2}$	3.16Å → 3.18Å
450 ℃	28.22° → 28.02°	Hexagonal	$\bar{2}00$	3.81Å → 3.84Å

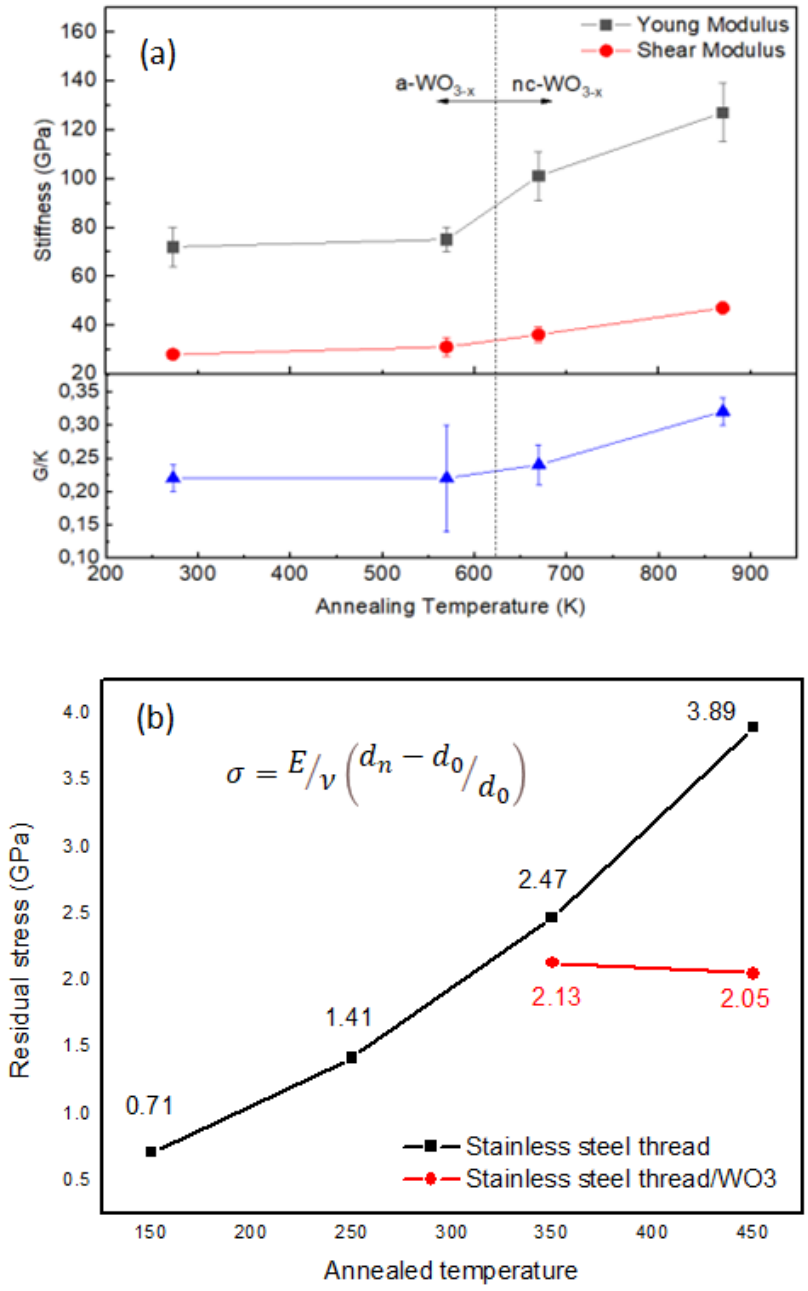

Figure 55. Comparison of (a) Young's modulus for WO_3 annealed at different temperatures and (b) calculated residual stress of uncoated stainless steel thread and WO_3 electrodeposited film onto stainless steel thread annealed at different temperatures.

4-6. Modeling periodic cracks

Numerical calculation for modeling periodic cracking of WO_3 thin films was performed by two geometries comparison as shown in Fig. 53. The stress distribution was calculated along the mid-plane between two cracks of depth h and distance 2s apart for a given value of applied strain. The resulting crack opening displacements were computed, and the critical strain energy channeling this new crack was calculated. The calculated results are shown in Fig. 56. Matching between the geometric separation properties of the material and the applied strain was found. It can be seen that the range of strains for periodic arrays increases as the feature separation increases. Two separate curves are plotted, one without modulus mismatch (black) and one with the given Dundur's parameter (red). The three separate regions can be defined as few cracks, periodic cracks, and random cracks. The conclusions from modeling periodic cracking of thin films is consistent with the experimental observation. By carefully analyzing the SEM images of electrodeposited WO_3 films annealed at 350 and 450 ℃, the geometric spacings were obtained and paired with the values of mechanical properties, so that plots for the annealed WO_3 films define different regions as periodic and random cracks, respectively.

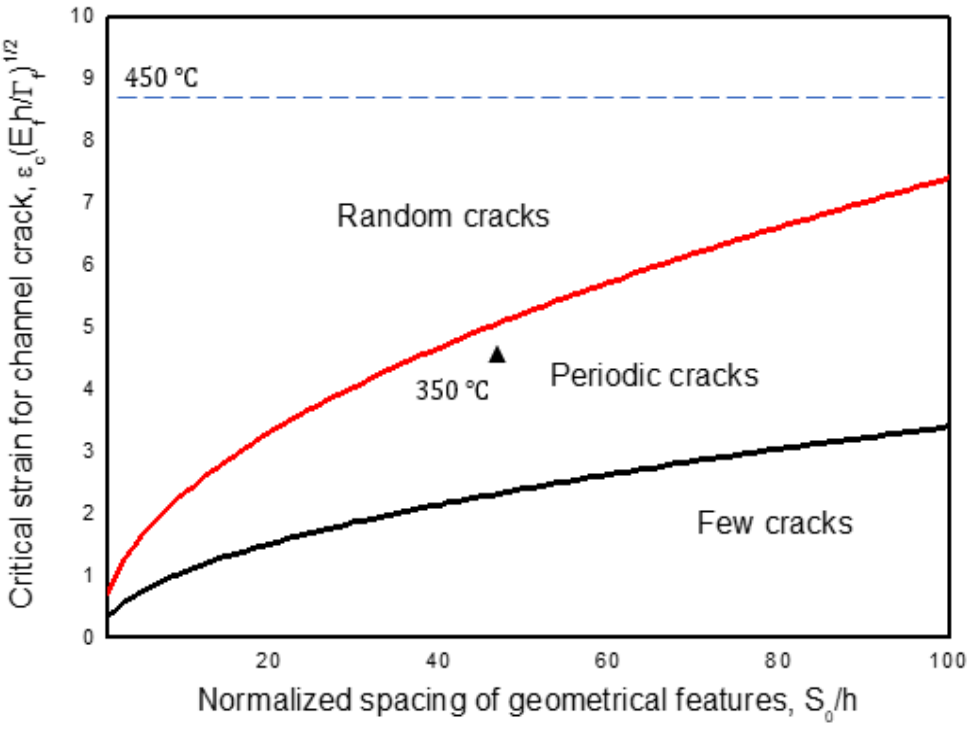

Figure 56. Plots showing the regimes of critical strains vs geometric spacing in which periodic crack arrays contained.

Chapter 5. Conclusions & Future work

5-1. Conclusions

WO_3 electrodeposited on stainless steel thread was introduced as a photoelectrochemical cell and liquid junction solar cell. Morphology, crystal structure, and photoelectrochemical behavior of WO_3 electrodeposited on stainless steel 316 L thread has been studied. The morphology of electrodeposited WO_3 on stainless steel thread shows a dense structure with the coating surrounding the individual fibrils of the thread. Annealing the crystal causes a phase transition of $WO_3 \cdot H_2O$ to monoclinic and hexagonal structure at 350 and 450 ℃, respectively. Using the onset and plateau current under illumination as an indication of photoactivity, a photocurrent of 317 $\mu A/cm^2$ was observed with fast response to chopped illumination. The performance of the liquid junction solar cell showed enhanced values of open circuit voltage (V_{OC}), short circuit current (J_{SC}), fill factor (FF) and overall efficiency (η) by adsorbing natural and synthetic organic dyes onto the WO_3 surface. To improve the PV parameters, 0.1 M of redox catalyst TEA was added to the redox electrolyte and maximum performance of $V_{OC} = 98.55$ mV, $J_{SC} = -0.171$ mA/cm^2, $FF = 46.3\%$, and $\eta = 2.44\%$ was achieved with the blackberry dye-loaded liquid junction cell. Separating the electrodes with a uniform PMMA latex layer on the counter electrode helped prevent shorting and charge recombination, improving power conversion efficiency. Fig. 57 shows a comparison of energy levels relative to WO_3. Based upon the results of the I-V curves, the photovoltaic

effect for WO_3 electrodeposited on stainless steel thread could be observed with either twisted or parallel electrode orientations.

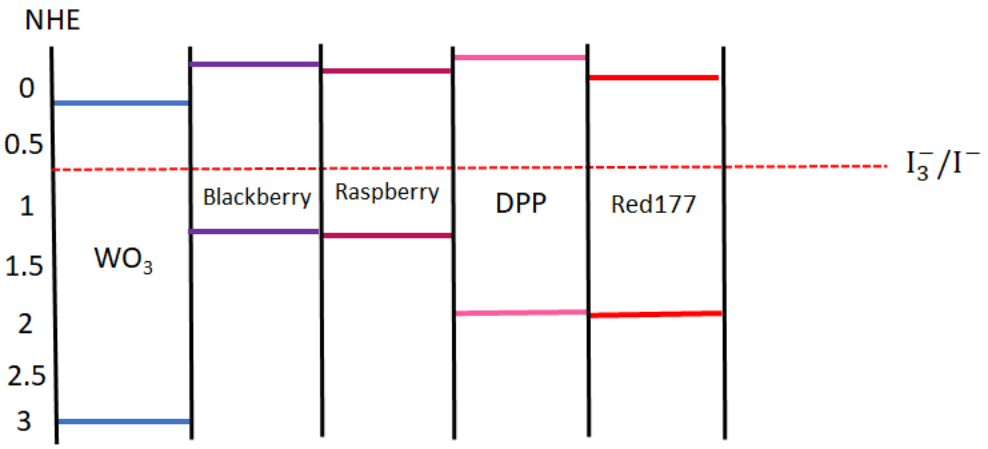

Figure 57. Band gap energy and band gap alignment comparison of natural and organic dyes.

Residual stresses of WO_3 thin films electrodeposited onto stainless steel thread annealed at temperatures between 50 to 450 ℃ were compared. The residual stress analysis was conducted by measuring the strain energy by XRD. The results indicated that for stainless steel 316L thread substrates, stress increased after annealing at higher temperatures. The WO_3 film showed decreased residual stress after annealing at 450 ℃, so that it may be used to control the residual stress creation. By modeling the periodic cracking of WO_3 films, the critical strain rate vs the geometric crack spacing was used to simulate the periodic cracking. By comparison of SEM images to the modeled plots, agreement with the theoretical simulation was obtained.

5-2. Future work

In this work, in order to create lightweight, portable, energy-harvesting devices, electrochemistry was performed on single fibers of metallic steel threads to deposit a WO_3 semiconductor photoanode and create a junction with a redox electrolyte. To further advance the technology, the wire-shaped liquid junction photovoltaic cells will be woven into a textile, so that output voltage and current from each wire cell can be additive. Fig. 58 shows a schematic diagram for textile fabrication from liquid junction cell threads by stacking stainless steel fiber meshes, one with electrodeposited WO_3 and one with Pt particles. To avoid contact between the two mesh electrodes, the same procedure will be followed that was employed for the single wires, i.e., a PMMA latex would act as a protective layer around the Pt-deposited steel mesh counter electrode. By incorporating the liquid electrolyte into thin films of transparent laminate paper (PEG films) it could also be used as a sealant. Further study will be conducted to replace the liquid electrolyte with a gel or a solid electrolyte to minimize leakage from the cell.

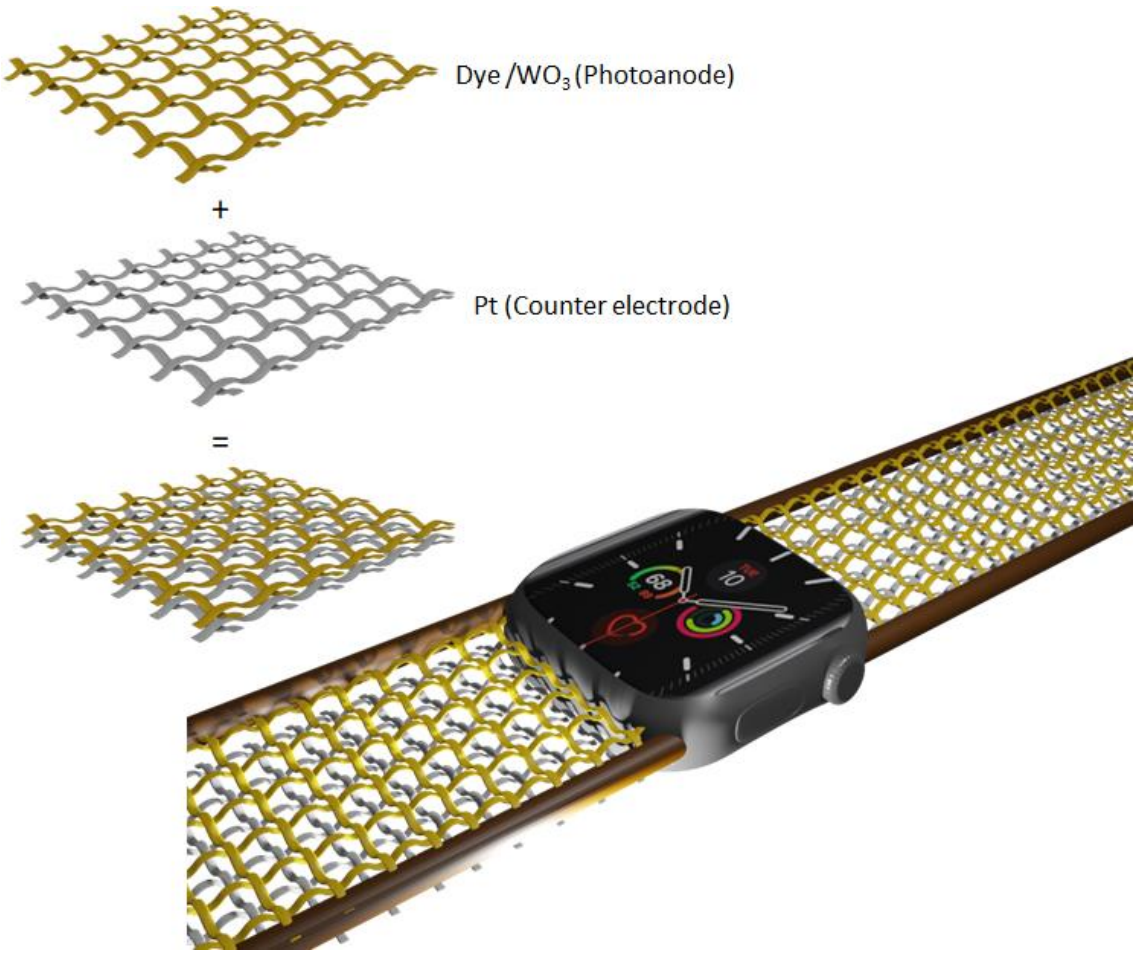

Figure 58. Fabrication of the liquid junction solar cells into a textile.

REFERENCES

[1] Pan, S., Yang, Z., Chen, P., Deng, J., Li, H., & Peng, H. (2014). Wearable solar cells by stacking textile electrodes. *Angewandte Chemie*, *126*(24), 6224-6228.

[2] Malik, N. K., Singh, J., Kumar, R., & Rathi, N. (2013). A Review on Solar PV Cell'. International Journal of Innovative Technology Exploring Engineering, 3, 116-19.

[3] Sproul, A. (2003). Understanding the p-n Junction. Solar Cells: Resource for the Secondary Science Teacher, 73.

[4] Aribisala, H. A. (2013). Improving the efficiency of solar photovoltaic power system. University of Rhode Island.

[5] Sproul, A. (2003). Understanding the p-n Junction. *Solar Cells: Resource for the Secondary Science Teacher*, *73*.

[6] Smith, R. P., Hwang, A. A. C., Beetz, T., & Helgren, E. (2018). Introduction to semiconductor processing: Fabrication and characterization of pn junction silicon solar cells. *American Journal of Physics*, *86*(10), 740-746.

[7] Sinton, R. A., & Cuevas, A. (2000, May). A quasi-steady-state open-circuit voltage method for solar cell characterization. In Proceedings of the 16th European photovoltaic solar energy conference (Vol. 1152, p. 4).

[8] Tsuno, Y., Hishikawa, Y., & Kurokawa, K. (2006, May). Translation equations for temperature and irradiance of the IV curves of various PV cells and modules. In 2006 IEEE 4th World Conference on Photovoltaic Energy Conference (Vol. 2, pp. 2246-2249). IEEE.

[9] Tributsch, H., & Gerischer, H. (1969). The use of semiconductor electrodes in the study of photochemical reactions. Berichte der Bunsengesellschaft für physikalische Chemie, 73(8-9), 850-854.

[10] Fujishima, A., & Honda, K. (1972). Electrochemical photolysis of water at a semiconductor electrode. nature, 238(5358), 37-38.

[11] O'regan, B., & Grätzel, M. (1991). A low-cost, high-efficiency solar cell based on dye-sensitized colloidal TiO_2 films. nature, 353(6346), 737-740.

[12] Lianos, P. (2011). Production of electricity and hydrogen by photocatalytic degradation of organic wastes in a photoelectrochemical cell: the concept of the photo-fuel cell: a review of a re-emerging research field. Journal of Hazardous Materials, 185(2-3), 575-590.

[13] Chiu, Y. H., Lai, T. H., Kuo, M. Y., Hsieh, P. Y., & Hsu, Y. J. (2019). Photoelectrochemical cells for solar hydrogen production: Challenges and opportunities. APL Materials, 7(8), 080901.

[14] Sharma, K., Sharma, V., & Sharma, S. S. (2018). Dye-sensitized solar cells: fundamentals and status. Nanoscale research letters, 13(1), 1-46.

[15] Wang, Q., Ito, S., Grätzel, M., Fabregat-Santiago, F., Mora-Sero, I., Bisquert, J., ... & Imai, H. (2006). Characteristics of high efficiency dye-sensitized solar cells. The Journal of Physical Chemistry B, 110(50), 25210-25221.

[16] Han, W., Shi, Q., & Hu, R. (2021). Advances in electrochemical energy devices constructed with tungsten oxide-based nanomaterials. Nanomaterials, 11(3), 692.

[17] Hai, G., & Zhang, H. (2019). The Photocatalytic Applications of TiO_2-WO_3 Heterostructure in Methylene Blue. American Academic Scientific Research Journal for Engineering, Technology, and Sciences, 61(1), 135-142.

[18] Ismail, M., Chebaane, M. M., Bousselmi, L., Zahraa, O., Olivier, C., & Toupance, T. (2021). Photoelectrochemical properties of WO_3-modified anatase TiO_2 photoanodes and application for dye-sensitized solar cells. Surfaces and Interfaces, 27, 101543.

[19] Lee, M. G., Park, J. S., & Jang, H. W. (2018). Solution-processed metal oxide thin film nanostructures for water splitting photoelectrodes: a review. Journal of the Korean Ceramic Society, 55(3), 185-202.

[20] Liu, Y., Xie, S., Liu, C., Li, J., Lu, X., & Tong, Y. (2014). Facile synthesis of tungsten oxide nanostructures for efficient photoelectrochemical water oxidation. Journal of Power Sources, 269, 98-103.

[21] Chatten, R., Chadwick, A. V., Rougier, A., & Lindan, P. J. (2005). The oxygen vacancy in crystal phases of WO_3. The Journal of Physical Chemistry B, 109(8), 3146-3156.

[22] Zheng, H., Ou, J. Z., Strano, M. S., Kaner, R. B., Mitchell, A., & Kalantar-zadeh, K. (2011). Nanostructured tungsten oxide–properties, synthesis, and applications. Advanced Functional Materials, 21(12), 2175-2196.

[23] Zheng, J. Y., Haider, Z., Van, T. K., Pawar, A. U., Kang, M. J., Kim, C. W., & Kang, Y. S. (2015). Tuning of the crystal engineering and photoelectrochemical properties of crystalline tungsten oxide for optoelectronic device applications. CrystEngComm, 17(32), 6070-6093.

[24] Diez-Cabanes, V., & Pastore, M. (2021). Morphological engineering of inorganic semiconductor VIS-light-driven nanocatalysts: experimental and theoretical understandings. The Journal of Physical Chemistry C, 125(28), 15125-15133.

[25] Khamkhom, P., Chananonnawathorn, C., Hincheeranun, W., Limwichean, S., Eiamchai, P., Saekow, B., ... & Horprathum, M. (2018, September). Preparation and characterization of tungsten trioxide nanoplates by low cost acid treatment method. In AIP Conference Proceedings (Vol. 2010, No. 1, p. 020020). AIP Publishing LLC.

[26] Li, W., Da, P., Zhang, Y., Wang, Y., Lin, X., Gong, X., & Zheng, G. (2014). WO_3 nanoflakes for enhanced photoelectrochemical conversion. ACS nano, 8(11), 11770-11777.

[27] Yang, L., Chen, Z., Ma, T., Zhang, S., Dai, W., Xiao, X., ... & Luo, S. (2021). Efficient electrochemical dehalogenation of florfenicol without discharging toxic intermediates via direct electron transfer over electrochromic WO_3. Chemical Engineering Journal, 412, 127481.

[28] Xing, P., Zhou, F., & Li, Z. (2019). Preparation of WO_3/g-C_3N_4 composites with enhanced photocatalytic hydrogen production performance. Applied Physics A, 125(11), 1-7.

[29] Santos, L., Neto, J. P., Crespo, A., Baião, P., Barquinha, P., Pereira, L., ... & Fortunato, E. (2015). Electrodeposition of WO_3 nanoparticles for sensing applications. Electroplating of nanostructures, 1-22.

[30] Momeni, M. M., & Ghayeb, Y. (2016). Photochemical deposition of platinum on titanium dioxide–tungsten trioxide nanocomposites: an efficient photocatalyst under

visible light irradiation. Journal of Materials Science: Materials in Electronics, 27(2), 1062-1069.

[31] Abd Rashid, A., Saad, N. H., Sheng, D. B. C., & Akhir, M. A. M. (2015). Hydrothermal synthesis of tungsten oxide (WO_3) nanostructures using sodium chloride as structure directing agent.

[32] Mardare, C. C., & Hassel, A. W. (2019). Review on the versatility of tungsten oxide coatings. *physica status solidi (a)*, *216*(12), 1900047.

[33] Kwong, W. L., Savvides, N., & Sorrell, C. C. (2012). Electrodeposited nanostructured WO_3 thin films for photoelectrochemical applications. *Electrochimica Acta*, *75*, 371-380.

[34] Georgieva, J., Armyanov, S., Valova, E., Philippidis, N., Poulios, I., & Sotiropoulos, S. (2008). Photoelectrocatalytic activity of electrosynthesised tungsten trioxide-titanium dioxide bi-layer coatings for the photooxidation of organics. *Journal of Advanced Oxidation Technologies*, *11*(2), 300-307.

[35] Peng, M., & Zou, D. (2015). Flexible fiber/wire-shaped solar cells in progress: properties, materials, and designs. Journal of Materials Chemistry A, 3(41), 20435-20458.

[36] Zhang, Z., Yang, Z., Wu, Z., Guan, G., Pan, S., Zhang, Y., ... & Peng, H. (2014). Weaving efficient polymer solar cell wires into flexible power textiles. Advanced Energy Materials, 4(11), 1301750.

[37] Choudhury, B. D., Lin, C., Shawon, S. M. A. Z., Soliz-Martinez, J., Huq, H., & Uddin, M. J. (2021). A photoanode with hierarchical nanoforest TiO_2 structure and silver

plasmonic nanoparticles for flexible dye sensitized solar cell. Scientific reports, 11(1), 1-11.

[38] Cai, X., Hou, S., Wu, H., Lv, Z., Fu, Y., Wang, D., ... & Zou, D. (2012). All-carbon electrode-based fiber-shaped dye-sensitized solar cells. Physical Chemistry Chemical Physics, 14(1), 125-130.

[39] Cai, F., Chen, T., & Peng, H. (2012). All carbon nanotube fiber electrode-based dye-sensitized photovoltaic wire. Journal of Materials Chemistry, 22(30), 14856-14860.

[40] Chen, T., Qiu, L., Li, H., & Peng, H. (2012). Polymer photovoltaic wires based on aligned carbon nanotube fibers. Journal of Materials Chemistry, 22(44), 23655-23658.

[41] Liu, D., Zhao, M., Li, Y., Bian, Z., Zhang, L., Shang, Y., ... & Huang, C. (2012). Solid-state, polymer-based fiber solar cells with carbon nanotube electrodes. Acs Nano, 6(12), 11027-11034.

[42] Chen, T., Wang, S., Yang, Z., Feng, Q., Sun, X., Li, L., ... & Peng, H. (2011). Flexible, light-weight, ultrastrong, and semiconductive carbon nanotube fibers for a highly efficient solar cell. Angewandte Chemie, 123(8), 1855-1859.

[43] Shahizuan, W. D., & Mohd, Y. (2012). Influence of pH solution on the electrodeposition of tungsten oxide (WO_3) films onto indium tin oxide (ITO)-glass substrate. Journal of Science and Technology, 4(1).

[44] Sharma, R., & Kar, K. K. (2015). Particle size and crystallographic orientation controlled electrodeposition of platinum nanoparticles on carbon nanotubes. Electrochimica Acta, 156, 199-206.

[45] Huang, X., & Brittain, W. J. (2001). Synthesis and characterization of PMMA nanocomposites by suspension and emulsion polymerization. Macromolecules, 34(10), 3255-3260.

[46] Zyoud, A., Zaatar, N., Saadeddin, I., Helal, M. H., Campet, G., Hakim, M., ... & Hilal, H. S. (2011). Alternative natural dyes in water purification: anthocyanin as TiO_2-sensitizer in methyl orange photo-degradation. Solid State Sciences, 13(6), 1268-1275.

[47] Holler, F. J., Skoog, D. A., & Crouch, S. R. (2007). Chapter 1. *Principles of Instrumental Analysis (6th ed.). Cengage Learning*, 9.

[48] Mohamed, A. M., Shaban, S. A., El Sayed, H. A., Alanadouli, B. E., & Allam, N. K. (2016). Morphology–photoactivity relationship: WO_3 nanostructured films for solar hydrogen production. International Journal of Hydrogen Energy, 41(2), 866-872.

[49] Prabhu, N., Agilan, S., Muthukumarasamy, N., & Senthil, T. S. (2014). Enhanced photovoltaic performance of WO_3 nanoparticles added dye sensitized solar cells. Journal of Materials Science: Materials in Electronics, 25(12), 5288-5295.

[50] Kalanur, S. S., Yoo, I. H., Cho, I. S., & Seo, H. (2019). Effect of oxygen vacancies on the band edge properties of WO_3 producing enhanced photocurrents. Electrochimica Acta, 296, 517-527.

[51] Cherepy, N. J., Smestad, G. P., Grätzel, M., & Zhang, J. Z. (1997). Ultrafast electron injection: implications for a photoelectrochemical cell utilizing an anthocyanin dye-sensitized TiO_2 nanocrystalline electrode. The Journal of Physical Chemistry B, 101(45), 9342-9351.

[52] Du, C., Liu, B., Hu, J., & Li, H. (2021). Determination of iodine number of activated carbon by the method of ultraviolet–visible spectroscopy. Materials Letters, 285, 129137.

[53] Farhana, N. K., Ramesh, S., & Ramesh, K. (2019). Efficiency enhancement of dye-sensitized solar cell based gel polymer electrolytes using Poly (vinyl butyral-co-vinyl alcohol-co-vinyl acetate)/tetrapropylammonium iodide. *Materials Science in Semiconductor Processing*, *91*, 414-421.

[54] Quan, H., Gao, Y., & Wang, W. (2020). Tungsten oxide-based visible light-driven photocatalysts: crystal and electronic structures and strategies for photocatalytic efficiency enhancement. Inorganic Chemistry Frontiers, 7(4), 817-838.

[55] Seo, D. B., Yoo, S., Dongquoc, V., Trung, T. N., & Kim, E. T. (2021). Facile synthesis and efficient photoelectrochemical reaction of WO_3/WS_2 core@ shell nanorods utilizing $WO_3 \cdot 0.33\ H_2O$ phase. Journal of Alloys and Compounds, 888, 161587.

[56] Etienne, A., Radiguet, B., Genevois, C., Le Breton, J. M., Valiev, R., & Pareige, P. (2010). Thermal stability of ultrafine-grained austenitic stainless steels. Materials Science and Engineering: A, 527(21-22), 5805-5810.

[57] Xiong, Y., He, T., Wang, J., Lu, Y., Chen, L., Ren, F., ... & Volinsky, A. A. (2015). Cryorolling effect on microstructure and mechanical properties of Fe–25Cr–20Ni austenitic stainless steel. Materials & Design, 88, 398-405.

[58] Huang, Y., Li, Y., Zhang, G., Liu, W., Li, D., Chen, R., ... & Ni, H. (2019). Simple synthesis of 1D, 2D and 3D WO_3 nanostructures on stainless steel substrate for high-performance supercapacitors. Journal of Alloys and Compounds, 778, 603-611.

[59] Shukla, S., Loc, N. H., Boix, P. P., Koh, T. M., Prabhakar, R. R., Mulmudi, H. K., ... & Xiong, Q. (2014). Iron pyrite thin film counter electrodes for dye-sensitized solar cells: high efficiency for iodine and cobalt redox electrolyte cells. ACS nano, 8(10), 10597-10605.

[60] Ma, M., Zhang, K., Li, P., Jung, M. S., Jeong, M. J., & Park, J. H. (2016). Dual oxygen and tungsten vacancies on a WO_3 photoanode for enhanced water oxidation. Angewandte Chemie, 128(39), 11998-12002.

[61] Kim, Y. O., Yu, S. H., Ahn, K. S., Lee, S. K., & Kang, S. H. (2015). Enhancing the photo-response of electrodeposited WO_3 film: Structure and thickness effect. Journal of Electroanalytical Chemistry, 752, 25-32.

[62] Senthil, T. S., Muthukumarasamy, N., Velauthapillai, D., Agilan, S., Thambidurai, M., & Balasundaraprabhu, R. (2011). Natural dye (cyanidin 3-O-glucoside) sensitized nanocrystalline TiO_2 solar cell fabricated using liquid electrolyte/quasi-solid-state polymer electrolyte. Renewable Energy, 36(9), 2484-2488.

[63] Calogero, G., Yum, J. H., Sinopoli, A., Di Marco, G., Grätzel, M., & Nazeeruddin, M. K. (2012). Anthocyanins and betalains as light-harvesting pigments for dye-sensitized solar cells. Solar energy, 86(5), 1563-1575.

[64] Cahya Prima, E., Yuliarto, B., & Dipojono, H. K. (2015). Theoretical investigation of anthocyanidin aglycones as photosensitizers for dye-sensitized TiO_2 solar cells. In Advanced Materials Research (Vol. 1112, pp. 317-320). Trans Tech Publications Ltd.

[65] Dualeh, A., De Angelis, F., Fantacci, S., Moehl, T., Yi, C., Kessler, F., ... & Grätzel, M. (2012). Influence of donor groups of organic D−π−a dyes on open-circuit voltage in solid-state dye-sensitized solar cells. The Journal of Physical Chemistry C, 116(1), 1572-1578.

[66] Ayaz, M., Khan Kasi, J., Khan Kasi, A., Bokhari, M., & Boschloo, G. (2022). Improved Dye Regeneration through Addition of a Triphenylamine Electron Donor in

Iodide-Based Electrolytes for Dye-Sensitized Solar Cells. ACS Applied Energy Materials, 5(4), 4240-4246.

[67] Shieh, Y. T., Yeh, Y. C., & Cheng, C. C. (2020). Two-way CO_2-responsive polymer particles with controllable amphiphilic properties. ACS omega, 5(4), 1862-1869.

[68] Thouless, M. D., Li, Z., Douville, N. J., & Takayama, S. (2011). Periodic cracking of films supported on compliant substrates. Journal of the Mechanics and Physics of Solids, 59(9), 1927-1937.

[69] Taylor, A. A., Edlmayr, V., Cordill, M. J., & Dehm, G. (2011). The effect of film thickness variations in periodic cracking: Analysis and experiments. Surface and Coatings Technology, 206(7), 1830-1836.

[70] Hubertus, J., Croce, S., Neu, J., Rizzello, G., Seelecke, S., & Schultes, G. (2020). Influence of residual stresses of sputtered thin film electrodes for dielectric elastomer applications. Multidisciplinary Digital Publishing Institute Proceedings, 64(1), 2.

[71] Nikravesh, S., Ryu, D., & Shen, Y. L. (2020). Instabilities of thin films on a compliant substrate: direct numerical simulations from surface wrinkling to global buckling. Scientific reports, 10(1), 1-19.

[72] Bush, K. A., Rolston, N., Gold-Parker, A., Manzoor, S., Hausele, J., Yu, Z. J., ... & McGehee, M. D. (2018). Controlling thin-film stress and wrinkling during perovskite film formation. ACS Energy Letters, 3(6), 1225-1232.

[73] Huang, J., Kim, B. C., Takayama, S., & Thouless, M. D. (2014). The control of crack arrays in thin films. Journal of materials science, 49(1), 255-268.

[74] Noyan, I. C., Huang, T. C., & York, B. R. (1995). Residual stress/strain analysis in thin films by X-ray diffraction. Critical Reviews in Solid State and Material Sciences, 20(2), 125-177.

[75] Abadias, G., Chason, E., Keckes, J., Sebastiani, M., Thompson, G. B., Barthel, E., ... & Martinu, L. (2018). Stress in thin films and coatings: Current status, challenges, and prospects. Journal of Vacuum Science & Technology A: Vacuum, Surfaces, and Films, 36(2), 020801.

[76] Motazedian, F., Wu, Z., Zhang, J., Shariat, B. S., Jiang, D., Martyniuk, M., ... & Yang, H. (2019). Determining intrinsic stress and strain state of fibre-textured thin films by X-ray diffraction measurements using combined asymmetrical and Bragg-Brentano configurations. Materials & Design, 181, 108063.

[77] Shenoy, V. B., Schwartzman, A. F., & Freund, L. B. (2001). Crack patterns in brittle thin films. International journal of fracture, 109(1), 29-45.

[78] Freund, L. B., & Shenoy, V. B. (2000, May). Crack Patterns due to residual stress in thin films. Eighteenth Symposium on Energy Engineering Sciences, (p. 9).

[79] Ciavarella, M., & Decuzzi, P. (2001). The state of stress induced by the plane frictionless cylindrical contact. II. The general case (elastic dissimilarity). International journal of solids and structures, 38(26-27), 4525-4533.

[80] Besozzi, E., Dellasega, D., Russo, V., Conti, C., Passoni, M., & Beghi, M. G. (2019). Thermomechanical properties of amorphous metallic tungsten-oxygen and tungsten-oxide coatings. Materials & Design, 165, 107565.